Decay Dynamics of Quantum Dots in Nanophotonic Structures

Johansen, Jeppe; Lodahl, Peter; Hvam, Jørn Marcher

Publication date:
2008

Decay Dynamics of Quantum Dots in Nanophotonic Structures

Jeppe Johansen

9th May 2008

DTU Fotonik
Department of Photonics Engineering

DTU Fotonik
Department of Photonics Engineering
Technical University of Denmark
Building 345V
2800 Kgs. Lyngby
DENMARK

PREFACE

This thesis presents research carried out from April 2005 to May 2008 in the Quantum Optics Group, Nanophotonics Cluster, at DTU Fotonik, The Department of Photonics Engineering while I have been enrolled as a Ph.D. student at the Technical University of Denmark.

The Ph.D. study has been supervised by

- Associate Prof. Peter Lodahl
- Prof. Jørn M. Hvam

First I would like to thank my supervisors for their guidance and support during these three years. Peter Lodahl, for always being available for questions, for taking the time to do daily supervision when needed, and for teaching me about the colourful world of photonic crystals. Jørn M. Hvam, for giving me the opportunity to do research in the Nanophotonics Cluster, and for sharing his great knowledge and general overview within the field of semiconductor physics.

Despite my name being the only one on this thesis my fellow Ph.D students Søren Stobbe, Toke Lund-Hansen, Philip T. Kristensen and Post Doc Brian Julsgaard have all contributed to the work presented here. They all deserve to be greatly acknowledged for many helpful discussions, for advice, help and company in the laboratory, for doing the advanced fabrication of photonic-crystal membranes, for supervising my first steps in the cleanroom and much more. The help of Associate Prof Kresten Yvind, in relation to cleanroom work, and the help of Senior Research Scientist Kristján Leósson with introduction to the closed-cycle cryostate, is greatly appreciated.

I would also like to thank Professor Willem L. Vos who gave me the opportunity to visit and do experiments in the Photonic Bandgaps group, at Amolf Institute, Amsterdam, The Netherlands. During my visit I had the great pleasure of working with Ph.D. student Merel Leistikow who introduced me to the colloidal quantum

dots.

In our work on photonic-crystal membranes we have had the great opportunity to rely on numerical calculations most generously provided by Dr. A. Femius Koenderink, group leader of Resonant Nanophotonics at Amolf Institute, Amsterdam, The Netherlands.

A special thank goes to all my fellow Ph.D. students in the Nanophotonics cluster who have all contributed to the pleasant and enjoyable daily atmosphere. In particularly Toke, Søren, Philip, Mads, Stephan, Per, Martin, Elaine, Rasmus (Systems), Tine, Jens, and David.

Finally, I would like to express my gratitude to Drude. Thanks for standing by me and supporting me during the rough times. Thanks for bearing with my absence during the long working hours in the lab and especially during the writing of this thesis. And thanks for supplying the office with plenty of delicious cake ...

ABSTRACT

This thesis describes time-resolved optical characterization of spontaneous emission from self-assembled quantum dots in nanophotonic media, with particular focus on the interpretation of decay dynamics of the spontaneous emission.

The fundamental properties of the quantum dots, i.e., the oscillator strength and the quantum efficiency are determined. These properties are essential for an understanding of the light-emitter interaction in complex nanophotonic structures. The experimental method is based on positioning the quantum dots at various positions in a medium with a known modification of local density of optical states. The energy dependence of the oscillator strength and the quantum efficiency is measured by probing different quantum dots within the quantum dot ensemble. Superior optical properties are found for quantum dots emitting at low energies.

The relation between the measured oscillator strength and the overlap of the electron and hole wavefunctions of the quantum dot ground state is established. This model is used to deduce the energy dependence of the wavefunction overlap from the measured oscillator strengths.

The decay dynamics is studied under different excitation conditions and analyzed in a model which takes into account the fine structure of the quantum dot exciton. From the analysis the intrinsic spin-flip rates between the bright (optically active) and the dark (optically inactive) exciton states are extracted.

Finally, the strongly modified spontaneous emission from a quantum dot ensemble embedded in a photonic-crystal membrane is studied. Strong inhibition of the spontaneous emission is observed within a wide frequency range, in excellent agreement with the 2D photonic band gap predicted by theory. Enhanced emission rates are observed on both sides of the band gap as expected from theory. Using the gained knowledge of the optical properties and the decay dynamics, the first successful quantitative comparison between experiment and a full 3D calculation of the local density of optical states is performed.

RESUMÉ

Denne afhandling beskriver tidsopløste optiske målinger af spontan emission fra selvdannede kvantepunkter indlejret i nanofotoniske materialer. Afhandling fokuserer i særlig grad på at opnå forståelse af den spontane emissions henfaldsdynamik.

Kvantepunkternes fundamentale egenskaber, d.v.s. deres kvanteeffektivitet og oscillatorstyrke, bestemmes. En fastlæggelse af disse egenskaber er nødvendig for at kunne opnå en forståelse af vekselvirkningen mellem lys og emittere i komplekse nanofotoniske strukturer. Den eksperimentelle metode beror på, at kvantepunkterne placeres forskellige steder i en struktur med en kendt variation i den lokale optiske tilstandstæthed. Energiafhængigheden af kvanteeffektiviteten og oscillatorstyrken fastlægges ved at udføre tidsopløste målinger på forskellige undergrupperinger af kvantepunkterne. Det viser sig, at store kvantepunkter, som udsender lys ved lav energi, besidder bedre optiske egenskaber end små kvantepunkter. Der etableres en relation mellem kvantepunktets oscillatorstyrke og overlappet af elektronens og hullets bølgefunktioner. Ud fra denne relation bestemmes overlappets energiafhængighed.

Den spontane emissions henfaldsdynamik studeres under systematisk varierede pumpebetingelser og analyseres i en model baseret på excitonens finstrukturniveauer. Ved denne analyse findes den intrinsiske spin flip-rate imellem de optisk aktive (bright) og de optisk inaktive (dark) excitontilstande.

Endeligt studeres den stærkt modificerede spontane emission fra kvantepunkter indlejret i en membran med fotonisk krystalstruktur. I fuld overensstemmelse med teoretiske beregninger af et to-dimensionelt fotonisk båndgab observeres en kraftig undertrykkelse af den spontane emission i et bredt frekvensspektrum samt en øget emissionsrate på begge sider af dette. Ved at anvende den opnåede viden om henfaldsdynamikken foretages den første succesfulde sammenligning mellem eksperimentelle målinger og en tredimensional beregning af den lokale optiske tilstandstæthed.

PUBLICATIONS

The following publications have resulted from this Ph.D. project.

Journal publications

- J. Johansen, S. Stobbe, I. S. Nikolaev, T. Lund-Hansen, P. T. Kristensen, J. M. Hvam, W. L. Vos, and P. Lodahl, *Size dependence of the wavefunction of self-assembled InAs quantum dots from time-resolved optical measurements*, Phys. Rev. B **77** (7), 073303 (2008).

- B. Julsgaard, J. Johansen, S. Stobbe, T. Stolberg-Rohr, T. Sünner, M. Kamp, A. Forchel and P. Lodahl, *Decay dynamics of quantum dots influenced by the local density of optical states of two-dimensional photonic crystal membranes*, Submitted to App. Phys. Lett., (*arXiv:0802.2947v1*).

Journal publications in preparation

- J. Johansen, B. Julsgaard, J. M. Hvam, and P. Lodahl, *Influence of the exciton fine structure on the decay dynamics of quantum-dot ensembles*, Work in progress.

- S. Stobbe, J. Johansen, J. M. Hvam, and P. Lodahl, *Determination of the Frequency Dependence of Quantum Efficiency and Oscillator Strength of Quantum Dot Excitons by a Modified Local Density of Optical States Technique*, Work in progress.

Conference contributions

- M. L. Andersen, S. Stobbe, J. Johansen, and P. Lodahl, *Coupling of Self-Assembled InAs Quantum Dots to Surface Plasmon Polaritons*, CLEO, San Jose, USA 2008.

- S. Stobbe, J. Johansen, A. Löffler, S. Höfling, A. Forchel, J. M. Hvam, W. L. Vos, and P. Lodahl, *Breakdown of the Dipole Approximation for Large Quantum Dot Emitters Coupled to an Interface*, CLEO, San Jose, USA 2008.

- S. Stobbe, J. Johansen, I. S. Nikolaev, T. Lund-Hansen, P. T. Kristensen, J. M. Hvam, W. L. Vos, and P. Lodahl, *Accurate measurement of the transition dipole moment of self-assembled quantum dots*, CLEO Europe, Munich, Germany 2007.

- T. Lund-Hansen, J. Johansen, T. van Lippen, R. Notzel, J. M. Hvam, and P. Lodahl, *Time- and energy-resolved measurements of spontaneous emission from ordered quantum dots*, NANOMETA, Seefeld, Austria 2007.

- T. Lund-Hansen, J. Johansen, S. Stobbe, J. M. Hvam, and P. Lodahl, *Measuring dipole moment and quantum efficiency of self-assembled InAs/GaAs quantum dots using a modified electromagnetic vacuum*, DFS annual meeting, Nyborg, Denmark 2007.

- J. Johansen, S. Stobbe, J. M. Hvam, and P. Lodahl, *Modified local density of optical states as a diagnostic tool for quantum dot decay dynamics*, ICOOPMA, London, UK 2007.

- J. Johansen, S. Stobbe, I. S. Nikolaev, T. Lund-Hansen, P. T. Kristensen, J. M. Hvam, W. L. Vos, and P. Lodahl, *Quantum efficiency of self-assembled quantum dots determined by a modified optical local density of states*, CLEO/ QELS, Baltimore, USA 2007.

- B. Julsgaard, S. Stobbe, J. Johansen, T. Stolberg-Rohr, T. Sünner, M. Kamp, A. Forchel, and P. Lodahl, *Probing the local density of optical states in 2D photonic crystal membranes*, ECIO, Copenhagen, Denmark 2007.

- T. Lund-Hansen, J. Johansen, S. Stobbe, J. M. Hvam, and P. Lodahl, *Detailed investigation of spontaneous emission decay rates of self-assembled InAs quantum dots*, ECIO, Copenhagen, Denmark 2007.

- J. Johansen, T. Lund-Hansen, J. M. Hvam, and P. Lodahl, *Highly Efficient Spontaneous Emission from Self-Assembled Quantum Dots*, EOS, Paris, France 2006.

CONTENTS

1. INTRODUCTION

One of the fundamental processes in quantum optics is the spontaneous emission of light. Spontaneous and stimulated emission are two closely related processes caused by the coupling between the radiation field and excited emitters, e.g., atoms, molecules, or quantum dots. Stimulated emission occurs due to interaction with photons, while spontaneous emission is caused by interaction with so-called virtual photons. The virtual photons are a property of the vacuum field and are caused by its fluctuations. The fluctuations of the vacuum field can only be described by a full quantization of the electric field, and spontaneous emission is therefore a truly quantum mechanical phenomenon. Interesting techniques to control the dynamics of spontaneous emission, i.e., to inhibit or to enhance the emission rate, are one of the main foci of quantum optics.

Control over spontaneous emission can play an important role for applications such as, e.g., efficient light emitting diodes, solar cells, low-threshold lasers, and single-photon sources for quantum information. The vacuum fluctuations, which stimulate the spontaneous emission, can be manipulated by structuring the environment of the emitter. Until recently such intriguing experiments on controlled spontaneous emission were performed only for atomic systems limiting the connection to applications. However, the ability to fabricate high-quality nanostructured materials (photonic crystals) with embedded light sources (quantum dots) has opened a new field of *all-solid-state* quantum optics.

The solid state implementation of quantum optics has several assets: the emitter properties can be conveniently tailored by quantum dot growth, the emitters have fixed positions, and the photon dispersion relation can be tailored by proper design of the photonic crystal. The solid state implementation has a large potential as it allows for strong enhancement of the emission rate while keeping the extraction efficiency high. This can be obtained in photonic crystal cavities due to the extremely small mode volumes achievable and a moderate quality factor or in properly designed waveguides where the slow down of light causes a strong light-matter interaction. Moreover, the solid state implementation has the clear

advantage that large-scale realizations of quantum optics devices can take advantage of the very mature semiconductor fabrication technology.

This thesis concerns the study of modified spontaneous emission from quantum dots embedded in nanophotonic structures. However, before we can perform a detailed study of the complex nanophotonic environment of a photonic crystal, it is essential to know the fundamental properties of the embedded light sources, i.e., the quantum dots. As a necessity, we therefore start by obtaining the fundamental properties of the quantum dots, before we focus on the study of the complex nanophotonic environment in photonic crystals.

The outline of the thesis is as follows. Chapter 2 provides an introductory background for the thesis. The general properties of spontaneous emission in a homogeneous medium and in a photonic crystal membrane are reviewed and the electrical and optical properties of self-assembled quantum dots are discussed. In Chapter 3 time-resolved spontaneous emission measurements on quantum dots positioned in a medium with well-known modifications in the vacuum fluctuations are presented. The measurements allow for an accurate determination of the oscillator strength and the quantum efficiency of the quantum dots. Chapter 4 concerns the determination of the overlap of the electron and hole wavefunctions from the measurements presented in Chapter 3. The measured wavefunction overlap is compared to numerical calculations. In Chapter 5, a detailed study of the quantum dot decay dynamics under different excitation conditions is presented. The measurements are discussed in a model involving the bright and dark states of the quantum dot exciton allowing for a determination of the spin-flip rate. Chapter 6 concerns time-resolved measurements from quantum dot ensembles in a photonic crystal membrane. The existence of a 2D photonic band gap is clearly demonstrated. Using the knowledge of the quantum dot properties gained in Chapters 3 to 5 we perform the first successful comparison of experiment and theory. A short summary of the conclusions and an outlook are given in Chapter 7.

2. CONTROLLING THE SPONTANEOUS EMISSION FROM QUANTUM DOTS BY PHOTONIC CRYSTALS

In this chapter we discuss modified spontaneous emission in the context of quantum dots embedded in photonic crystals. Using Fermi's Golden Rule and the quantized electromagnetic field we, calculate the rate of spontaneous emission. We stress the importance of the local density of optical states for the spontaneous emission rate, and introduce the concept of photonic crystals with emphasis on the properties of 2D photonic crystal slabs. The electronic and optical properties of self-assembled quantum dots are discussed with focus on the intrinsic decay dynamics of the spontaneous emission.

The great interest in photonic crystals was mainly spurred by the theoretical works of Yablonovitch [1] and John [2] published in 1987. In these papers the authors point out the potential of photonic crystals as a tool to control the spontaneous emission. In the following years much effort was put into theoretical investigations of the band structure for different crystal symmetries and materials in order to determine structures which would posses a full photonic band gap. It was later shown that strong inhibition of the spontaneous emission rate also can occur in photonic crystals without a full photonic band gap; while the total density of optical states may only be weakly modified, the *local* density of optical states (LDOS) at the position of the emitter might still be strongly modified [3].

The first experimental verification of controlled spontaneous emission rates of emitters placed inside photonic crystals was reported in 2004 by Lodahl *et al.* [4]. LDOS-caused modifications in the spontaneous emission rates of embedded emitters were actually claimed in two earlier papers [5, 6], but the results reported in both papers were disputed shortly after publication: The modified rates reported

in Ref. [5] were later ascribed to changes in the chemical environment by authors working on a similar system [7]. The results reported in Ref. [6] were disputed both from a theoretical and an experimental point of view: i) due to the low dielectric contrast of the photonic crystal only weak modifications (below 10%) of the spontaneous emission rate are to be expected, and ii) measurements on a similar photonic crystal show no modification of the decay rate when compared with the proper reference [8]. Several groups have recently reported enhancement as well as inhibition of the spontaneous emission rate [9–17]. The focus of the research has mainly been on enhanced emission from defect cavities [9,10,13,14,17]. Only a few groups have performed systematic studies of the strongly modified light-emitter coupling in photonic crystals without cavities [4,11,18] and the potential of the modified LDOS in such photonic crystals is surprisingly often overlooked. However, quantitative comparison to theory has so far been lacking. It is our goal to obtain a quantitative understanding of the light-emitter coupling in photonic crystals. This will clarify the potential and set the limits of photonic crystals as the ultimate tool for control of spontaneous emission.

The measurements reported in Refs. [4,18] are performed on 3D inverse opal structures infiltrated with colloidal quantum dots, while the measurements in Ref. [11] are on PCMs with an embedded quantum well. The PCM-quantum-well system is not the ideal system for a quantitative study of the light-emitter coupling in photonic crystal as: i) non-radiative recombination via the surface states at the edges of the air holes is known to be a serious issue deteriorating the quantum efficiency [11,19], ii) the non-local property of a quantum well exciton, i.e., the Bohr radius is larger than for an exciton confined in a quantum dot and it is moreover possible for the exciton to diffuse in the quantum well plane, resulting in a non-trivial average over the spatially strongly varying LDOS.

In Refs. [4,18] systematic studies of LDOS effects were presented. However, obtaining a quantitative understanding using colloidal quantum dots in inverse opals is hindered by several factors: i) The main hindrance is the intrinsically multi-exponential decay of the spontaneous emission [20,21] and the lack of a simple model capable of describing the multi-exponential decay in terms of non-radiative and radiative contributions. ii) The random orientation of the quantum dots' transition dipole moments and their spatial distribution on the inside of the air spheres adds to the complexity of the interpretation of ensemble measurements. iii) The calculation of the 3D LDOS for the inverse opal structure is a tremendous task [18] as it must be performed for at large subset of positions and orientations on the

inside of the air sphere to support the interpretation of an ensemble measurement.

We propose to perform the study of the light-emitter coupling in a different system, namely, a photonic crystal membrane with embedded InAs quantum dots. This system is very appealing from a fabricational point of view as it is compatible with standard semiconductor nano-processing techniques and from an experimental point of view as it is possible to address single quantum dots using a high-resolution micro-photoluminescence setup. Before we can obtain a quantitative understanding of the complex spontaneous emission from quantum dot ensembles in photonic crystals, it is essential to have detailed knowledge of the intrinsic decay dynamics of the quantum dots. To gain this knowledge we start by a careful study of the spontaneous emission from quantum dot ensembles in much less complex systems, i.e., quantum dot ensemble positioned at known distances to a dielectric interface. In this system the LDOS can be calculated exactly, allowing us to measure important optical properties of the quantum dots necessary for a quantitative comparison to the LDOS calculations.

2.1 Photonic crystals as a tool to control spontaneous emission

Spontaneous emission is the process by which an emitter undergoes a transition from an excited state to a state of lower energy by emitting a photon. It is a pure quantum mechanical phenomenon which must be phenomenologically added if the light-matter interaction is described in a semi-classical picture [22]. A full quantum mechanical treatment, in which not only the emitter but also the electromagnetic field is quantized, is thus needed to give the correct description of spontaneous emission. In contrast to the classical description of the electric field, the quantized description leads to a non-zero variance of the field. This implies that even in the vacuum state the electric field exhibits fluctuations around its mean value of zero. These vacuum fluctuations, which sometimes are referred to as *virtual* photons, can stimulate the excited emitter to 'spontaneously' emit a photon.

Before the work of Purcell in 1946 [23] the rate of spontaneous emission was generally believed to be an intrinsic property of the emitter. Purcell, however, discovered that by placing an emitter in a cavity on resonance with the emitter the emission rate would increase by a factor of $F_{\mathrm{P}} = \frac{3Q\lambda^3}{4\pi^2 V_{\mathrm{c}}}$, where Q and V_{c} are the quality factor and the volume of the cavity respectively. The quantity F_{P} is better known today as the Purcell factor. Later Drexhage [24] proved that not only emitters in resonant interaction with cavities will display a modified decay rate; emitters placed nearby reflecting interfaces will also exhibit enhancement as well

as inhibition of their spontaneous emission rates - even though the modifications are more moderate in this case. Kleppner [25] pointed out that the emission rate of an emitter in a cavity not necessarily will be enhanced, but that the cavity also can be used to inhibit the rate of spontaneous emission. The inhibition occurs if the optical modes into which the spontaneous emission should take place is not supported by the cavity.

The observed enhancement and inhibition of spontaneous emission rates are due to variations in the density of optical states (DOS). In a non-homogeneous environment the electromagnetic waves will scatter on the inhomogeneities and these scattered waves will interfere with the non-scattered waves. This leads to both constructive (enhancement of the DOS) and destructive (inhibition of the DOS) interference depending on the spatial position and the wavelength of concern. This spatial dependence, which becomes very pronounced in strongly modified surroundings such as a inside a photonic crystal, is explicitly noted by referring to the *local* density of optical states (LDOS) [3].

2.1.1 Spontaneous emission

In this section we will use Fermi's Golden Rule and the quantized electromagnetic field as a starting point to obtain the explicit dependence of the spontaneous emission rate on the LDOS. We define the ground state of our system $|g\rangle$ to correspond to an unpopulated quantum dot, while the excited state $|e\rangle$ corresponds to a quantum dot occupied by an exciton.

Description of the atom-field interaction

According to Fermi's Golden Rule, which can be derived using time-dependent perturbation theory [26], the radiative transition rate γ_{rad} from an initial state $|i\rangle$ to a set of final states $|f\rangle$ is given as [22,27]

$$\gamma_{\mathrm{rad}} = \frac{2\pi}{\hbar^2} \sum_f \left| \langle f|\hat{\mathcal{H}}_{int}|i\rangle \right|^2 \delta(\omega_i - \omega_f), \tag{2.1}$$

where $\hat{H}_{int}$ is the interaction Hamiltonian describing the quantum-dot-field interaction and the delta-function ensures that the energy of the system is conserved. The interaction Hamiltonian is part of the Hamiltonian of the complete system which can be written as

$$\hat{\mathcal{H}} = \hat{\mathcal{H}}_{QD} + \hat{\mathcal{H}}_F + \hat{\mathcal{H}}_{int}, \tag{2.2}$$

where the Hamiltonians $\hat{\mathcal{H}}_{QD}$ and $\hat{\mathcal{H}}_F$ describes the uncoupled quantum dot and field. In second quantization the atomic Hamiltonian can be expressed as

$$\hat{\mathcal{H}}_{QD} = \hbar\omega\hat{\pi}^\dagger\hat{\pi}, \tag{2.3}$$

where $\omega = \omega_\mathrm{e} - \omega_\mathrm{g}$. The operator $\hat{\pi}^\dagger = |e\rangle\langle g|$ shifts the quantum dot from the ground state to the excited state, while $\hat{\pi} = |g\rangle\langle e|$ performs the reverse transition. In terms of the photon annihilation $\hat{a}_{\mathbf{k}\lambda}$ and creation $\hat{a}^\dagger_{\mathbf{k}\lambda}$ operators the Hamiltonian of the electric field is expressed as

$$\hat{\mathcal{H}}_F = \sum_{\mathbf{k}}\sum_{\lambda}\hbar\omega_k\left(\hat{a}^\dagger_{\mathbf{k}\lambda}\hat{a}_{\mathbf{k}\lambda} + \frac{1}{2}\right), \tag{2.4}$$

where the photon annihilation and creation operators act on photons in the particular field mode described by the wavevector $\mathbf{k}$ (and thus energy $\hbar\omega_k$) and polarization λ.

In the electric dipole approximation, where all higher order multipoles are neglected, the interaction Hamiltonian is given as the inner product of the dipole operator $\hat{\boldsymbol{\mu}} = e\hat{\mathbf{r}}$ and the operator for the quantized electric field $\hat{\mathbf{E}}(\mathbf{R})$:

$$\hat{\mathcal{H}}_{int} \quad = \quad \hat{\boldsymbol{\mu}}\cdot\hat{\mathbf{E}}(\mathbf{R}) = \boldsymbol{\mu}(\hat{\pi}^\dagger + \hat{\pi})\cdot\hat{\mathbf{E}}(\mathbf{R}). \tag{2.5}$$

Here e is the electron charge, $\hat{\mathbf{r}}$ denote the position operator for the electron and $\mathbf{R}$ the position of the quantum dot exciton's centre of mass. Inserting $\hat{\mathbf{E}}(\mathbf{R})$ expressed in terms of the annihilation and creation operators and the polarization vector $\mathbf{e}_{\mathbf{k}\lambda}$ for the electric field (and invoking the rotating-wave approximation) the Hamiltonian can be written as [22]

$$\hat{\mathcal{H}}_{int} = \mathrm{i}\sum_{\mathbf{k}}\sum_{\lambda}\hbar g_{\mathbf{k}\lambda}\left(\hat{\pi}^\dagger\hat{a}_{\mathbf{k}\lambda}e^{i\mathbf{k}\cdot\mathbf{R}} - \hat{a}^\dagger_{\mathbf{k}\lambda}\hat{\pi}e^{-i\mathbf{k}\cdot\mathbf{R}}\right), \tag{2.6}$$

where the coupling strength $g_{\mathbf{k}\lambda}$ between the atom and field is defined as

$$g_{\mathbf{k}\lambda} = \frac{1}{\hbar}\sqrt{\frac{\hbar\omega_k}{2\epsilon\epsilon_0 V}}\,\mathbf{e}_{\mathbf{k}\lambda}\cdot\boldsymbol{\mu}. \tag{2.7}$$

Here the factor $\sqrt{\frac{\hbar\omega_k}{2\epsilon\epsilon_0 V}}$ stems from the normalization of the electric field, ϵ is the dielectric constant of the material surrounding the atom, ϵ_0 is the permittivity of vacuum, and V is the quantization volume.

Rate of spontaneous emission in a homogeneous medium

To calculate the rate of spontaneous emission we must evaluate Eq. (2.1) for an initial state $|i\rangle = |\{0\}, e\rangle$ where the quantum dot is in the excited state $|e\rangle$ and the electric field is given by the vacuum state $|\{0\}\rangle$. The range of corresponding final states $|f\rangle = |1_{\mathbf{k}\lambda}, g\rangle$ are those where the quantum dot is in the ground state $|g\rangle$, and the electric field consists of a single photon in an arbitrary mode $|1_{\mathbf{k}\lambda}\rangle$. When operating on the vacuum state with the interaction Hamiltonian (Eq. (2.6)) only the second term leads to a non-zero result, reducing the summation to a summation over $g_{\mathbf{k}\lambda}$:

$$\begin{aligned}\sum_f \left|\langle f|\hat{\mathcal{H}}_{int}|i\rangle\right|^2 &= \sum_{\mathbf{k}}\sum_{\lambda}\left|\langle 1_{\mathbf{k}\lambda}, g|\hat{\mathcal{H}}_{int}|\{0\}, e\rangle\right|^2 \\ &= \sum_{\mathbf{k}}\sum_{\lambda}\left|-\mathrm{i}\hbar g_{\mathbf{k}\lambda} e^{-\mathrm{i}\mathbf{k}\cdot\mathbf{R}}\right|^2 \\ &= \sum_{\mathbf{k}}\sum_{\lambda}|\hbar g_{\mathbf{k}\lambda}|^2. \end{aligned} \tag{2.8}$$

In a homogeneous medium with a large volume ($V \to \infty$) the summation over $\mathbf{k}$ and λ can be substituted according to

$$\sum_{\mathbf{k}}\sum_{\lambda} \longrightarrow 2\frac{V}{(2\pi)^3}\int_0^{2\pi} d\phi \int_0^{\pi} d\theta \sin\theta \int_0^{\infty} dk\, k^2 \tag{2.9}$$

whereby the decay rate (Eq. (2.1)) can be expressed as

$$\begin{aligned}\gamma_{\mathrm{rad}} &= \frac{V}{2\pi\hbar}\int_0^{2\pi} d\phi \int_0^{\pi} d\theta \sin\theta \int_0^{\infty} dk\, k^2 |\hbar g_{\mathbf{k}\lambda}|^2 \delta(\omega) \\ &= \frac{n}{(2\pi)^2\epsilon_0\hbar c_0^3}\omega^3 \int_0^{2\pi} d\phi \int_0^{\pi} d\theta \sin\theta |\mathbf{e}_{\mathbf{k}\lambda}\cdot\boldsymbol{\mu}|^2 \\ &= \frac{n}{3\pi\epsilon_0\hbar c_0^3}\omega^3|\boldsymbol{\mu}|^2. \end{aligned} \tag{2.10}$$

In order to obtain Eq. (2.10) it has further been used that $\epsilon = n^2$ and $k = |\mathbf{k}| = n\frac{\omega_k}{c_0}$, where n is the refractive index of the surrounding material and c_0 is the speed of light in vacuum. The unit polarization vector of the electric field $\mathbf{e}_{\mathbf{k}\lambda} = (\sin(\phi)\sin(\theta), \sin(\phi)\cos(\theta), \cos(\phi))$ is averaged over the complete solid angle. Equation (2.10) is the well-known result for the decay rate of an emitter in a homogeneous medium.

The calculations above have been performed using the so-called $\mathbf{r}\cdot\mathbf{E}$ form of the interaction Hamiltonian, but an identical result can be obtained using the

$\mathbf{p}\cdot\mathbf{A}$ form of the Hamiltonian. In the latter, the interaction is described using the momentum operator of the electron $\hat{\mathbf{p}}$ and the operator for the vector potential $\hat{\mathbf{A}}$ which describes the quantized electric field. The interaction Hamiltonian can still be expressed as in Eq. (2.6), but in this form the coupling strength is defined as

$$g_{\mathbf{k}\lambda} = -\frac{e}{m_0}\sqrt{\frac{1}{2\epsilon\epsilon_0\omega_k\hbar V}}\,\mathbf{e}_{\mathbf{k}\lambda}\cdot\hat{\mathbf{p}}, \tag{2.11}$$

where m_0 denotes the free electron mass. To calculate the radiative decay rate we follow the path outlined above and find

$$\gamma_{\mathrm{rad}} = \frac{ne^2}{(2\pi)^2 m_0^2\epsilon_0\hbar c_0^3}\omega\int_0^{2\pi}d\phi\int_0^{\pi}d\theta\sin\theta|\langle g|\mathbf{e}_{\mathbf{k}\lambda}\cdot\hat{\mathbf{p}}|e\rangle|^2. \tag{2.12}$$

In order to calculate the decay rate, an integral over the projection of the electron momentum operator $\hat{\mathbf{p}}$ onto all field modes must thus be evaluated over the complete solid angle. In Chapter 4 we will return to the exact evaluation of this integral for the specific case of the ground state transition in InAs quantum dots.

Spontaneous emission rate in an inhomogeneous medium

The rate of spontaneous emission for a dipole emitter in an inhomogeneous medium, which is characterized by a loss-less and position dependent dielectric constant $\epsilon(\mathbf{r})$, can be calculated elegantly using a Green's function approach [27,28]. The dyadic Green's function $\overleftrightarrow{\mathbf{G}}(\mathbf{r},\mathbf{r}_0,\omega)$ defines the electric field $\mathbf{E}(\mathbf{r})$ at position $\mathbf{r}$ caused by an electric dipole emitter $\boldsymbol{\mu}$ located at $\mathbf{r}_0$ according to

$$\mathbf{E}(\mathbf{r}) = \omega^2\mu_0\mu_1\overleftrightarrow{\mathbf{G}}(\mathbf{r},\mathbf{r}_0,\omega)\cdot\boldsymbol{\mu}. \tag{2.13}$$

Here ω is the optical transition frequency, μ_0 is the vacuum permeability, and μ_1 is the permeability of the surrounding material. By expressing the electric field according to Eq. (2.13) it can be shown [27] that the rate of spontaneous emission can be calculated as

$$\gamma_{\mathrm{rad}} = \frac{\pi\omega}{3\hbar\epsilon_0}|\boldsymbol{\mu}|^2\rho_\mu(\mathbf{r}_0,\omega), \tag{2.14}$$

where the *projected* LDOS $\rho_\mu(\mathbf{r}_0,\omega)$ is defined by the dyadic Green's function (evaluated at the origin of the dipole) as

$$\rho_\mu(\mathbf{r}_0,\omega) = \frac{6\omega}{\pi c_0^2}[\mathbf{n}_\mu\cdot\mathrm{Im}\{\overleftrightarrow{\mathbf{G}}(\mathbf{r}_0,\mathbf{r}_0,\omega)\}\cdot\mathbf{n}_\mu]. \tag{2.15}$$

This *projected* LDOS differs from the DOS, $\rho(\omega)$, as it depends explicitly on position $\mathbf{r}_0$ and on the orientation of the transition dipole $\mathbf{n}_\mu$. For a dipole emitter with a fixed dipole axis $\mathbf{n}_\mu$, the orientation of the dipole axis will be important as the coupling to the different field modes, described by $\mathbf{k}$ and λ, is determined by the projection of the mode's polarization vector onto the dipole axis: $\mathbf{e}_{\mathbf{k}\lambda} \cdot \mathbf{n}_\mu$.

In an inhomogeneous medium the dyadic Green's function can be obtained as the sum of two dyadic Green's function: a free space (homogeneous) Green's function $\overleftrightarrow{\mathbf{G}}_0(\mathbf{r}, \mathbf{r}_0, \omega)$ and a scattering Green's function $\overleftrightarrow{\mathbf{G}}_s(\mathbf{r}, \mathbf{r}_0, \omega)$, where the latter describes the additional electric field caused by scattering on the inhomogeneities. As the contribution from the free space Green's function is the usual density of states, the ratio $\rho_\mu(\mathbf{r}_0, \omega)/\rho(\omega)$ can be written as

$$\frac{\rho_\mu(\mathbf{r}_0, \omega)}{\rho(\omega)} = 1 + \frac{6\pi c_0}{n\omega}[\mathbf{n}_\mu \cdot \mathrm{Im}\{\overleftrightarrow{\mathbf{G}}_s(\mathbf{r}_0, \mathbf{r}_0, \omega)\} \cdot \mathbf{n}_\mu]. \tag{2.16}$$

In order to obtain the normalized LDOS it is thus only necessary to calculate the scattering Green's function $\overleftrightarrow{\mathbf{G}}_s(\mathbf{r}_0, \mathbf{r}_0, \omega)$.

2.1.2 Photonic crystals

An ingenious way to modify the LDOS, and thus control the spontaneous emission, is by the using photonic crystals [1, 2, 29]. A photonic crystal is a periodic dielectric structure in which the refractive index varies on a length scale comparable to the wavelength of light. By proper design of a full 3D spatial periodicity of the refractive index, light will be Bragg reflected in all directions, whereby its propagation will be completely inhibited. In complete analogy with the electronic band gaps in solids in which the propagation of electrons is forbidden [30], this corresponds to the creation of a photonic band gap. Such a photonic band gap, i.e., the complete absence of *any* electromagnetic modes within a given energy interval, corresponds to a DOS which is identically zero.

Only a few structures, feasible to fabricate on a scale comparable to the wavelength of light, exhibit a full photonic band gap. These structures are: the woodpile structure [31, 32], the inverse opal structure [33, 34] and stacks of 2D photonic crystal slabs [35]. However, strong modification of the emission rate can also be obtained for structures without a complete photonic band gap [3]; even though the DOS at a given energy may by slightly enhanced, there can be specific positions in the structure for which the LDOS will be strongly reduced. The rate of spontaneous emission from an emitter placed at such a position will thus be strongly inhibited. Two-dimensional photonic crystals are technologically much

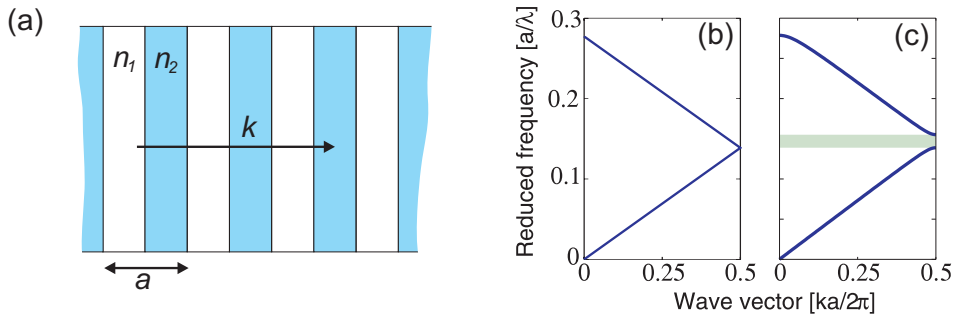

Fig. 2.1: **(a)** A sketch of a Bragg stack with period a and refractive indices n_1, n_2. The dispersion relations for light propagating at normal incidence to the Bragg stack are shown for alternating layers of GaAs-GaAs **(b)** and GaAs-air **(c)**. In the latter case a 1D band gap opens up a the zone edge. As the dispersion relations are plotted in reduced-zone scheme, i.e., only showing the k vectors belonging to the irreducible Brillouin zone, the lines are folded back into the zone when they reach its edge.

more compatible with standard semiconductor nano-fabrication techniques and offer a great and versatile platform for the incorporation of embedded emitters in the form of quantum dots. The dominant implementation of photonic crystals in semiconductors is thus the realization of 2D photonic crystals in slab waveguides suspended in air [14, 16, 17, 36–42]. These structures, known as photonic crystal membranes (PCMs), do not exhibit a complete photonic band gap, but they are capable of strongly modifying the spontaneous emission due to a strongly modified LDOS.

One-dimensional band gaps in photonic crystals

The appearance of band gaps is most easily understood by taking a brief look at the simplest photonic crystal at hand: the Bragg stack. The Bragg stack consists of alternating layers of dielectric materials with different refractive indices, c.f. Fig. 2.1(a). The lattice vector (period) of the stack is denoted by a. In Figs. 2.1(b) and (c) are shown the dispersion relation for light propagating at normal incidence to the Bragg stack. The wavevector k (abscissa) is normalized to the reciprocal lattice vector $K = 2\pi/a$ while the reduced frequency (ordinate) is given by $a/\lambda = \omega a/2\pi c_0$. In Fig. 2.1(b) the dispersion relation is shown for the trivial case of identical refractive indices of the two alternation layers. The

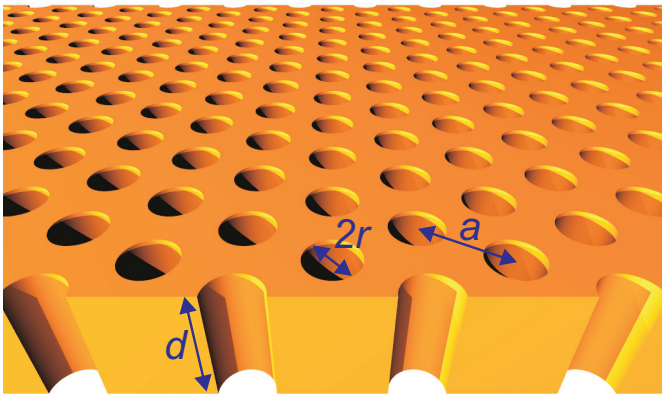

Fig. 2.2: Sketch of a photonic crystal membrane with a triangular lattice of air holes. The thickness of the membrane is denoted by d, while r denotes the radii of the air holes and a the lattice parameter.

dispersion relation is as expected found to be linear, $\omega = kc_0/n$. By changing the refractive index of one of the two materials, a 1D photonic band gap will open up as the degeneracy of the dispersion relation is lifted at the zone edge where the Bragg condition is met. This is shown in Fig. 2.1(c). At the zone edge the only extended waves in the Bragg stack will be standing waves. There are, however, two possible ways to centre these standing waves: either concentrated in the high index material or in the low index material. The two standing waves will thus experience different averaged refractive indices, and their frequencies will correspondingly be different resulting in a splitting of the dispersion relation at the zone edge [43]. However, only light propagating at normal incidence to the Bragg stack will experience this band gap; we refer therefore to it as a *1D* photonic band gap, while a full 3D band gap will be referred to simply as a photonic band gap.

Dispersion relation in a photonic crystal membrane

A sketch of a photonic crystal membrane (PCM), i.e., a waveguide slab suspended in air into which a 2D photonic crystal is defined, is shown in Fig. 2.2. The air holes are arranged in a triangular lattice with lattice constant a and hole radii r while the thickness of the membrane is d. Despite that the PCMs are only of a 2D

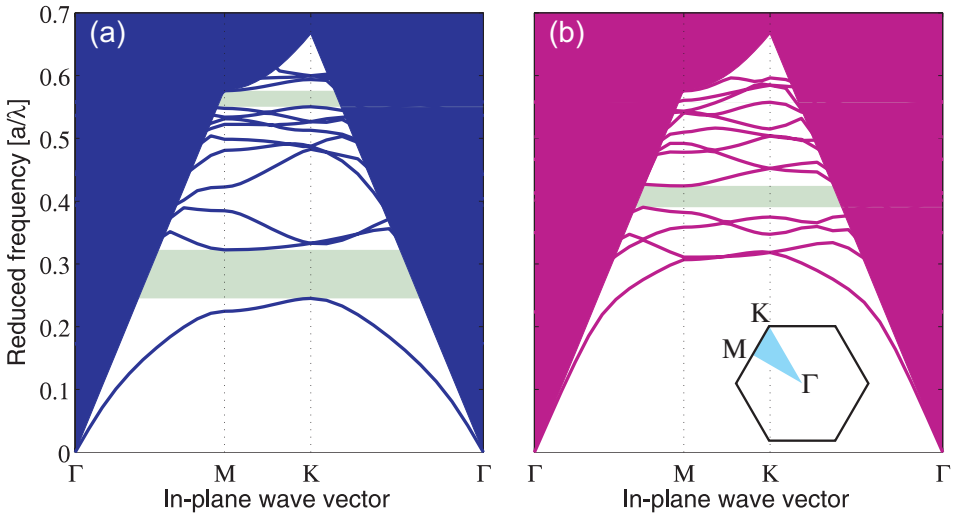

Fig. 2.3: Band diagrams for in-plane propagation within a photonic crystal membrane with $r/a = 0.3$, $d/a = 0.585$. The band diagrams are calculated for optical modes with in-plane polarization **(a)** and out-of-plane polarization **(b)**. Inset: The first Brillouin zone (BZ). The irreducible BZ is shaded light-blue and the high symmetry points Γ, M and K are indicated on the figure.

character they are still able to strongly modify the propagation of light; for the proper choice of the geometrical parameters (a, r, d) in-plane propagation will be strongly Bragg diffracted while total internal reflection causes strong confinement within the slab. The projected LDOS is found to be much stronger modulated in a PCM than in a ideal 2D photonic crystal extended to infinity in all three spatial directions [44]. The less pronounced LDOS modulation in the latter case is due to contributions from the modes allowed to propagate along the air cylinder which are only weakly affected by the photonic crystal, such modes cannot exist in the PCM.

In Figs. 2.3(a) and (b) the dispersion relations for the confined modes of a PCM are shown. The calculations, obtained with the freely-available software *MIT Photonic Bands* (MPB) [45], are done for a triangular lattice of air holes in a GaAs slab ($\epsilon_{\mathrm{GaAs}} = 13$) suspended in air. In the calculation the hole radii r and the thickness d are chosen to be $r/a = 0.3$ and $d/a = 0.585$, respectively, while the lateral dimensions of the membrane extend to infinity. We are only considering confined modes which propagate within the slab and thus appear below the light

cone indicated by the shaded areas. The calculations are performed for points on the edge of the irreducible Brillouin zone, shown in the inset in Fig. 2.3(b), as the band extrema are known to appear along these high-symmetry lines. The band diagram for modes polarized in the plane of the membrane (parallel to the membrane surface) is shown in Fig. 2.3(a), while the band diagram for the modes with an out-of-plane polarization is shown in Fig. 2.3(b). For the in-plane polarized modes two 2D band gaps appear as indicated by the light-green shaded areas; a wide gap at $a/\lambda = 0.3$ and a narrow one just below $a/\lambda = 0.6$. In case of out-of-plane polarization only a narrow 2D photonic band gap is found just above $a/\lambda = 0.4$. It is thus readily recognized that no complete photonic band gap exists in the PCM as the 2D photonic band gaps for the orthogonal polarizations do not coincide. However, the coincidence of the band gaps for the two polarizations would still not be enough to create a full photonic band gap, as we have not considered any modes not confined to the membrane. The DOS can be obtained directly from the band calculations, when all modes, i.e., including those propagating out of plane, are taken into account. However, for an emitter placed at a given position inside the PCM it is not the DOS, but the LDOS which is of relevance, i.e., the local density of optical modes at the particular emitter position and projected onto the orientation of the dipole emitter. Rigorous calculations of the projected LDOS for a similar PCM structure have been presented in Ref. [44].

Scalability of Maxwell's equations

An experimentally very important feature of photonic crystals is their scalability inherited from Maxwell's equations: as long as the system is macroscopic there is no fundamental length scale of the photonic crystals. This offers the advantage that instead of tuning the emitter wavelength, the size of the photonic crystal can be varied. This is of great experimental importance as the limitations imposed by a narrow tuning range of the emitter and by variations in the emitter properties caused by such tuning, can be completely avoided. In the measurements discussed in Chapter 6, the lattice parameter of photonic crystal is correspondingly varied while we keep probing quantum dots emitting at the same wavelength and thus probe identical sub-ensembles of the quantum dot ensemble. This is especially important as it will be shown in Chapter 3 that the quantum efficiency and the oscillator strength of quantum dots depend sensitively on their emission wavelength.

2.2 Electronic and optical properties of self-assembled quantum dots

Epitaxially grown semiconductor quantum dots have attracted significant attention recently as nano-scale light sources for use in solid state quantum electrodynamics. The quantum dots offer well-defined and tunable emission energies, nano-scale sizes and moreover the epitaxial growth facilitates spatial control in at least one dimension[1], which is highly desirable in photonic crystal membranes.

In this section we will briefly discuss how the electronic structure of quantum dots arises and which consequences the self-assembly process has on the electronic properties. The decay dynamics of the lowest energy level in the quantum dot is discussed in the usual two-level model, followed by a discussion of the effects of the exciton fine structure on the decay dynamics.

2.2.1 Electronic band structure of quantum dots

The electronic properties of solids are determined by the electrostatic potential of the crystal lattice caused by the atoms at the individual lattice sites. The potential, which inherits the periodicity and symmetry of the crystal lattice, will determine the dispersion relation of the electrons propagating in the crystal. Similar to the photonic band diagram shown in Fig. 2.1, a band diagram describing the electrons' dispersion relation in the solid can be calculated. The band structure provides a convenient way to describe the microscopic behaviour of the electrons and holes in the solid. Semiconductors differ from other solids by the existence of an electronic band gap between the highest occupied electron band (the valence band) and the lowest unoccupied electron band (the conduction band). In a direct semiconductor, e.g., GaAs or InAs, the maximum of the valence band and the minimum of the conductance band coincides at the origin of the Brillouin zone Γ. Near the origin, at which the wavevector of the electron is zero ($\boldsymbol{k} = 0$), the dispersion relation can be approximated as parabolic - similar to the dispersion relation for a free electron. The only difference in the two cases the curvature of the parabolic bands, which is accounted for by describing the electron by an *effective* mass instead of the free electron mass. This approach to a description of the motion of electrons in semiconductors is known as the *effective mass approximation* [30]. The

[1] Spatial control in three dimensions is immensely attractive as it allows for the precise lateral positioning within, e.g., cavities in PCMs. Impressive results have been attained by aligning the photonic crystal to a pre-measured quantum dot position [17].

effective mass approximation is also readily applicable to the motion of holes in the valence band, but in contrast to the conduction band the valence band is two-fold[2] degenerate at $\boldsymbol{k} = 0$. As the curvatures of the two bands are not identical the bands are described by different effective masses and are correspondingly termed the heavy hole and the light hole bands. The complexity of the valence bands is moreover increased as the effective masses assigned to the bands are anisotropic and thus depend on the direction of the wavevector.

Quantization of energy levels and excitonic effects

Confinement of the charge carriers can be obtained by embedding a semiconductor with a small band gap in a semiconductor with a larger band gap, hereby effectively creating a potential well in which the carriers will be trapped. Such *heterostructures* can be designed to confine the carriers in one, two or three directions. When the spatial width of the confinement potential is on the order of the de Broglie wavelength of the electron, the confinement will result in quantized energy levels and the structures confining the carriers in one, two and three dimensions are thus called quantum wells, quantum wires and quantum dots respectively. The quantization energy in these structures is not only dependent on the width of the confinement potential, but also on the barrier height and the effective mass of the carriers.

For free carriers in bulk semiconductors the Coulomb interaction between the electron and hole results in the formation of an electron-hole pair, known as an exciton. The motion of an exciton[3] can be separated into the motion of the centre of mass and the relative motion of the electron and hole. While the centre-of-mass motion is governed by the equations of motion for a free particle, the relative motion can be described by the Schrödinger equation for the hydrogen atom. In analogy with the case of the hydrogen atom, an exciton Bohr radius and the corresponding binding energy can be calculated. The exciton Bohr radii for the relevant semiconductors, i.e., GaAs and InAs, are 14 nm and 50 nm respectively [46, chap. 4], corresponding to binding energies of 5 meV and 1 meV. The sizes of the quantum dots considered in this thesis are small ($r_{\mathrm{QD}} \simeq 15\,\mathrm{nm}$) compared to the respective exciton Bohr radii and the exciton binding energies are thus

[2] In fact, the valence band is three-fold degenerate, but the third band, known as the split-off band, is permanently shifted towards lower energies due to spin-orbit coupling.

[3] We will only be concerned with weakly bound excitons, the so-called Wannier excitons, since Frenkel excitons are absent in InAs and GaAs as the electrons in the valence band screen the Coulomb interaction [30].

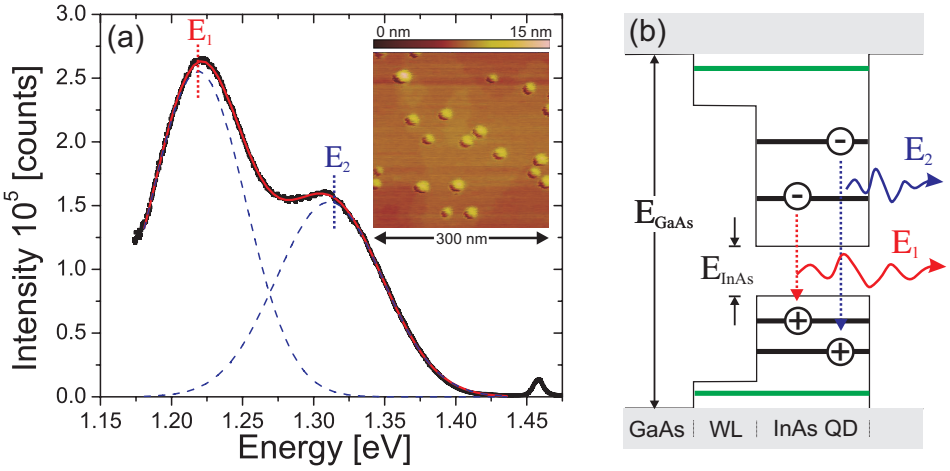

Fig. 2.4: **(a)** An emission spectrum from an ensemble of quantum dots showing the inhomogenously broadened ground state (E_1) and first excited state (E_2). The red line is a fit of two Gaussian distributions, each shown by the dashed blue lines. **Inset** An atomic force microscopy image of an uncapped layer of InAs quantum dots. **(b)** A schematic band diagram of a quantum dot. The continuum of electronic states in the GaAs is indicated by the grey shaded area. The wetting layer (WL) state is shown by the green-coloured level and two quantized energy levels with the energies E_1, E_2 indicated in the quantum dot. An exciton (electron-hole pair) is placed on each of the two levels.

negligible compared to the quantization energies in the quantum dot ($\sim 200\,\text{meV}$). The quantum dots are thus referred to as being in the regime of strong confinement and the exciton binding energy is safely neglected [46].

2.2.2 *Strain induced formation of self-assembled InAs/GaAs quantum dots*

The quantum dots which we use as our preferred light emitters are so-called *self-assembled* InAs/GaAs quantum dots. They are grown using molecular beam epitaxy (MBE) and the term self-assembled refers to their spontaneous formation during deposition of InAs on GaAs. Due to a large mismatch of the lattice constants of InAs and GaAs (6.06 Å and 5.65 Å respectively [47]), the InAs will be under a heavy compressive strain. The energy associated with the strain increases layer-by-layer until it reaches a critical value at which it is energetically more favourable to form extra surfaces than to form an extra InAs layer. Under the

proper growth conditions this results in the formation of dislocation-free 3D islands (quantum dots) on top of a few monolayers of heavily strained InAs (wetting layer) [46]. An atomic force microscopy image of such 3D islands is shown in the inset in Fig. 2.4(a). The wetting layer forms a very thin quantum well with energy levels just below the band gap of the GaAs. After formation of the quantum dots they are capped by a layer of GaAs, whereby the quantum dots are fully embedded in GaAs barriers. The self-assembly process results in the formation of quantum dots with slightly varying sizes and to some extend also with variations in chemical composition and shape. These variations will affect the quantized energy levels of the quantum dots causing an inhomogeneous broadening of the ensemble's emission spectrum, as shown in Fig. 2.4(a). The measured spectrum is very well modelled by the sum of two Gaussian distributions corresponding to the emission from two inhomogenously broadened states of the quantum dot ensemble. These states are the lowest lying states in the quantum dots and will thus be referred to as the exciton ground state and the first excited state. A schematic band diagram for a quantum dot is shown in Fig. 2.4(b) in which the wetting layer level, the first excited state, and the exciton ground state are indicated.

The compressive strain of the InAs leads to a deformation of the crystal lattice resulting in a loss of crystal symmetry. This affects the band structure causing a shift in the positions of the conduction and valence bands, changes in the effective masses, and also lifts the degeneracy of the light hole and heavy hole bands. In the case of compressive strain the light hole band is effectively shifted to higher energies [47], allowing us to assume that the quantum dot ground state is purely heavy hole like [48]. For all other states the picture becomes more complicated due to a possible mixing of the heavy and light hole bands [49, 50]. Whether the first excited state is predominantly of heavy hole or light hole character is thus an open question.

2.2.3 Calculations of the electronic properties of self-assembled quantum dots

The electronic properties of an idealized quantum dot, i.e., a quantum dot which can be described by a full rotational-symmetric potential, are easily obtained following the approach of any textbook on quantum mechanics, see e.g. Ref. [26]. For the colloidal CdSe/ZnS quantum dots discussed in Sec. 3.6 the use of such a model directly yields energy levels similar to those obtained in measurements. This is not surprising as the colloidal quantum dots are rotational symmetric and composed of unstrained materials. In the case of self-assembled quantum dots

the success of such an approach is, however, limited. This is mainly due to the complex strain distribution within and around the quantum dot and the spatial variations in intermixing of the quantum dot material and the surrounding barrier material [51, 52]. However, incorporating spatial distribution of strain as well as the chemical composition is only the first steps towards a more successful model and this demands knowledge of the exact geometrical shape of the quantum dot. Advanced atomistic models such as tight-binding models [53] or the empirical pseudo-potential approach [50, 54] might be the most promising approaches to a more successful modelling of quantum dots' electronic properties. These models do, however, still require knowledge of geometrical shape and size of the overgrown quantum dots, parameters which are not easily obtained. Moreover, due to the complexity such models can be hard to connect to physical quantities. In Chapter 4 we will discuss theoretical calculations of the electron and hole wavefunctions and compare our results to detailed experimental results.

2.2.4 Decay dynamics of quantum dot excitons

Quantum dots are often modelled as ideal two-level systems for which the decay dynamics is a simple single-exponential decay. Real quantum dots are however far from being ideal two-level systems and hence the decay dynamics shows a more complex behaviour. One of the causes for this increased complexity is the fine structure of the ground state exciton. The internal carrier dynamics among the individual fine structure levels of the exciton and their initial populations will have a significant influence on the decay curves [55]. In the present section we will discuss the decay dynamics of a two-level system with loss, and the decay dynamics of a three-level system based on the exciton fine structure levels.

Decay dynamics of a two-level system with loss

The decay dynamics of the ground state exciton is in the simplest model approximated as an ideal two-level system, in which we only consider the following two states: a populated and an unpopulated quantum dot ground state. A decay of the excited state will directly 'populate' the ground state. Here, we will immediately introduce loss into the system, i.e., the decay of the excited state can also occur without populating the ground state. For the sake of clarity, we have switched from describing the quantum dot using the electron and hole band structures to a description using the exciton level scheme. In the exciton level scheme the ground state $|g\rangle$ corresponds to the the crystal ground state, i.e., no excitons in the quan-

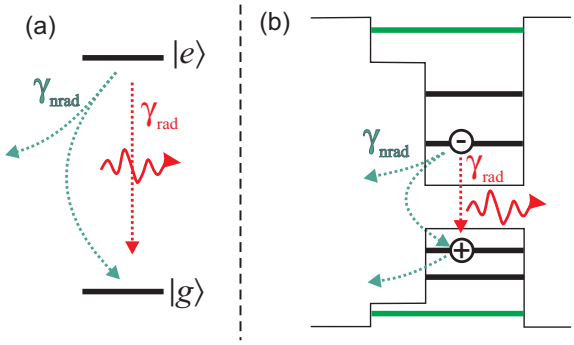

Fig. 2.5: **(a)** The two-level exciton scheme consists of the crystal ground state (no excitons) $|g\rangle$ and the exciton ground state $|e\rangle$. The populations of the excited state (exciton ground state) can decay by radiative recombination (γ_{rad}) or non-radiative processes (γ_{nrad}). Not all non-radiative processes imply a transition to the ground state $|g\rangle$ as indicated. **(b)** The equivalent band diagram.

tum dot, while the excited state $|e\rangle$ corresponds to the exciton ground state of the quantum dot, i.e., having an exciton in the ground state of the quantum dot. The excited state can decay by either radiative recombination (spontaneous emission) or by non-radiative processes, as shown schematically in Fig. 2.5(a) where the two processes have been assigned the rates γ_{rad} and γ_{nrad}, respectively. The equivalent band structure diagram is shown in Fig. 2.5(b) for comparison. While a radiative recombination directly implies a transition to the ground state, a non-radiative decay *may* lead to a transition to the ground state. The non-radiative rate includes loss of the exciton due to loss of the electron *or* the hole as well as loss due to non-radiative recombination of the exciton; only the latter implies a transition to the ground state.

In order to stress some basic points we will set up the rate equation for this simple system. Denoting the population probability of the excited state by ρ_{e} the rate equation reads:

$$\frac{\partial \rho_{\mathrm{e}}(t)}{\partial t} = -(\gamma_{\mathrm{rad}} + \gamma_{\mathrm{nrad}})\rho_{\mathrm{e}}(t). \tag{2.17}$$

From Eq. (2.17) the time evolution of the excited state population probability is readily identified as:

$$\rho_{\mathrm{e}}(t) = \rho_{\mathrm{e}}(0)e^{-(\gamma_{\mathrm{rad}}+\gamma_{\mathrm{nrad}})t}. \tag{2.18}$$

The total rate at which the exciton ground state decays is thus given by the sum

of the radiative and non-radiative decay rates. The photon flux from an ensemble of M quantum dots is given by the product of the radiative decay rate and the population:

$$L(t) = \gamma_{\mathrm{rad}} M \rho_{\mathrm{e}}(t) \quad = \quad \gamma_{\mathrm{rad}} M \rho_{\mathrm{e}}(0) e^{-(\gamma_{\mathrm{rad}}+\gamma_{\mathrm{nrad}})t}. \tag{2.19}$$

The signal detected in time-resolved measurements (number of counts/second) is thus given as

$$N(t) = \eta \gamma_{\mathrm{rad}} M \rho_{\mathrm{e}}(0) e^{-(\gamma_{\mathrm{rad}}+\gamma_{\mathrm{nrad}})t}, \tag{2.20}$$

where η denotes the total detection efficiency of our system, i.e., it takes into account the radiation pattern of the quantum dots, the collection efficiency of the optical setup and the detection efficiency of the detector. The time-resolved spontaneous emission from M quantum dots will thus decay single exponentially by a rate given by the total decay rate $(\gamma_{\mathrm{rad}} + \gamma_{\mathrm{nrad}})$, and the signal strength will be proportional to the radiative decay rate γ_{rad}.

The quantum efficiency of the quantum dots is given as the ratio of the radiative decay rate to the total decay rate: $QE = \frac{\gamma_{\mathrm{rad}}}{\gamma_{\mathrm{rad}}+\gamma_{\mathrm{nrad}}}$. This can also be obtained more rigorously by calculating the ratio of the number of excitons which decay by radiative decay to the total number of excitons initially in the system

$$QE = \frac{\int_0^\infty L(t)\,dt}{M\rho_{\mathrm{e}}(0)} = \frac{\int_0^\infty \gamma_{\mathrm{rad}} M \rho_{\mathrm{e}}(0) e^{-(\gamma_{\mathrm{rad}}+\gamma_{\mathrm{nrad}})t},dt}{M\rho_{\mathrm{e}}(0)} = \frac{\gamma_{\mathrm{rad}}}{\gamma_{\mathrm{rad}}+\gamma_{\mathrm{nrad}}}. \tag{2.21}$$

Decay dynamics in the presence of exciton fine structure

The ground state exciton is formed from the single-particle basis spanned by the electron ($S_e = 1/2$, $S_{e,z} = \pm 1/2$) and the heavy hole ($J_{hh} = 3/2$, $J_{hh,z} = \pm 3/2$). The light hole band ($J_{lh} = 1/2$, $J_{lh,z} = \pm 1/2$) can safely be neglected as the degeneracy of the light hole and heavy hole bands is lifted by the strain causing the formation of the quantum dots. The four exciton states, formed from the single-particle basis, are characterized by the projection of their total angular momentum onto the growth axis, $M_z = S_{e,z} + J_{hh,z}$, which can attain the values of either ± 1 or ± 2.[4] As photons carry an angular momentum of ± 1, they can only couple to excitons which have a total angular momentum of ± 1. These exciton states are thus termed bright, while the optically inactive states with a total angular momentum of ± 2 are termed dark excitons.

[4] The total *spin* angular momentum can take on values ± 1 (dark excitons) and 0 (bright excitons).

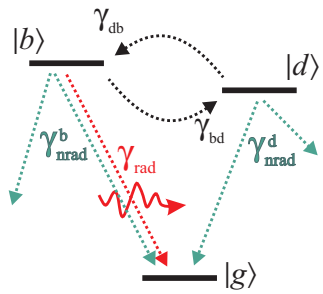

Fig. 2.6: The three-level scheme consists of a bright $|b\rangle$ and a dark $|d\rangle$ state, which couple through the spin-flip rates γ_{bd} and γ_{db}. Radiative recombination (γ_{rad}) is only possible for the bright state, while both the bright (γ^{b}_{nrad}) and the dark state (γ^{d}_{nrad}) can decay non-radiatively.

The exchange interaction, i.e., the coupling of the electron and hole spins, splits the energy levels of the bright and dark excitons by the electron-hole exchange energy ΔE_{bd} whereby the bright exciton level is displaced 300 to 400 μeV above the dark exciton level. The two dark states have a splitting on the order of $\sim 10\,\mu eV$, while the splitting of the two bright states depends on the rotational symmetry of the quantum dot and vary between $0\,\mu eV$ and $150\,\mu eV$ [48]. A detailed account of the exciton fine structure is given in Ref. [48]. In practice, the five-level scheme can be simplified to a scheme with only three levels: the ground state $|g\rangle$, the bright exciton levels $|b\rangle$, and the dark excitons levels $|d\rangle$, as depicted in Fig. 2.6. The bright and dark exciton states are coupled via spin flip, denoted by the rates γ_{bd} and γ_{db}. Apart from the spin-flip rates, radiative (γ_{rad}) and non-radiative processes (γ^{b}_{nrad}) lead to a decay of the bright exciton, while the dark exciton decay only takes place as non-radiative (γ^{d}_{nrad}).

The rate equations governing the temporal evolution of the bright and dark population probabilities are given as

$$\frac{\partial \rho_b}{\partial t} = -(\gamma_{rad} + \gamma^{b}_{nrad} + \gamma_{bd})\rho_b + \gamma_{db}\rho_d, \tag{2.22}$$

$$\frac{\partial \rho_d}{\partial t} = -(\gamma^{d}_{nrad} + \gamma_{db})\rho_d + \gamma_{bd}\rho_b, \tag{2.23}$$

where ρ_b and ρ_d are the population probabilities of the bright and dark exciton levels. The solution of the rate equations yields a bi-exponential decay of the populations probabilities of both bright and dark exciton states.

As we shall see in Chapter 5 the spin-flip rates are slow and by assuming $\gamma_{\mathrm{bd}}, \gamma_{\mathrm{db}} \ll (\gamma_{\mathrm{rad}} + \gamma^{\mathrm{b}}_{\mathrm{nrad}} - \gamma^{\mathrm{d}}_{\mathrm{nrad}})$ the temporal evolution of the bright state can be simplified to

$$\rho_{\mathrm{b}}(t) = \left[\rho_{\mathrm{b}}(0) - \frac{\gamma_{\mathrm{db}}}{\gamma_{\mathrm{rad}} + \gamma^{\mathrm{b}}_{\mathrm{nrad}} - \gamma^{\mathrm{d}}_{\mathrm{nrad}}}\rho_{\mathrm{d}}(0)\right] e^{-(\gamma_{\mathrm{rad}}+\gamma^{\mathrm{b}}_{\mathrm{nrad}}+\gamma_{\mathrm{bd}})t} + \frac{\gamma_{\mathrm{db}}}{\gamma_{\mathrm{rad}} + \gamma^{\mathrm{b}}_{\mathrm{nrad}} - \gamma^{\mathrm{d}}_{\mathrm{nrad}}}\rho_{\mathrm{d}}(0) e^{-(\gamma^{\mathrm{d}}_{\mathrm{nrad}}+\gamma_{\mathrm{db}})t}, \tag{2.24}$$

where $\rho_{\mathrm{b}}(0)$ and $\rho_{\mathrm{d}}(0)$ are the initial population probabilities of the bright and dark exciton levels, respectively. The bright population will thus undergo a bi-exponential decay. While the fast decaying term is caused by the direct recombination of the bright excitons, the slowly decaying term is caused by dark excitons undergoing a spin flip into bright excitons and then decaying by the bright decay rate. Due to the slow spin-flip rate the decay rate of the fast (slow) component is thus mainly given by the decay rate of the bright (dark) excitons:

$$\begin{aligned} \gamma_{\mathrm{f}} = &\quad \gamma_{\mathrm{rad}} + \gamma^{\mathrm{b}}_{\mathrm{nrad}} + \gamma_{\mathrm{bd}} &&\simeq \gamma_{\mathrm{rad}} + \gamma^{\mathrm{b}}_{\mathrm{nrad}} \\ \gamma_{\mathrm{s}} = &\quad \gamma^{\mathrm{d}}_{\mathrm{nrad}} + \gamma_{\mathrm{db}} &&\simeq \gamma^{\mathrm{d}}_{\mathrm{nrad}}. \end{aligned} \tag{2.25}$$

In accordance with Eq. (2.20), the time-resolved spontaneous emission from the bright exciton state is given as

$$\begin{aligned} N(t) &= \eta\gamma_{\mathrm{rad}} M \rho_{\mathrm{b}}(t) \\ &= A_{\mathrm{f}} e^{-\gamma_{\mathrm{f}} t} + A_{\mathrm{s}} e^{-\gamma_{\mathrm{s}} t}, \end{aligned} \tag{2.26}$$

where the second line defines the quantities for the fast A_{f} and slow A_{s} amplitude

$$\begin{aligned} A_{\mathrm{f}} &= \eta\gamma_{\mathrm{rad}} M \left[\rho_{\mathrm{b}}(0) - \frac{\gamma_{\mathrm{db}}}{\gamma_{\mathrm{rad}} + \gamma^{\mathrm{b}}_{\mathrm{nrad}} - \gamma^{\mathrm{d}}_{\mathrm{nrad}}}\rho_{\mathrm{d}}(0)\right], \\ A_{\mathrm{s}} &= \eta\gamma_{\mathrm{rad}} M \frac{\gamma_{\mathrm{db}}}{\gamma_{\mathrm{rad}} + \gamma^{\mathrm{b}}_{\mathrm{nrad}} - \gamma^{\mathrm{d}}_{\mathrm{nrad}}}\rho_{\mathrm{d}}(0). \end{aligned} \tag{2.27}$$

From Eqs. (2.26) and (2.27) we can thus conclude that the exciton fine structure leads to a bi-exponential decay of the spontaneous emission. While the fast rate is dominated by the decay of the bright excitons, the slow decay is given mainly by the decay of the dark excitons. However, the decay rates will not only affect the slopes of the fast and slow components, but also their relative amplitudes A_{f} and A_{s}. This will be exploited in Chapter 5 to quantify the spin-flip rate γ_{db}.

2.3 Summary

We have calculated the radiative decay rate of a quantum dot in a homogeneous medium. The radiative decay rate is expressed both in terms of the transition dipole moment and in terms of the electron momentum operator. The use of dyadic Green's functions to obtain the local density of optical states and thus the radiative decay rate in an inhomogeneous medium was introduced. The concept of photonic crystals was discussed and the occurrence of band gaps was explained in a one-dimensional model. Photonic crystal membranes were introduced and the calculations of the band diagrams were presented showing a wide in-plane 2D photonic band gap. The electronic properties of self-assembled quantum dots were discussed. A detailed discussion regarding the decay dynamics of self-assembled quantum dots was presented in the context of a simple two-level system and inclusion of the exciton fine structure. In the latter case the dynamics was found to be characterized by a bi-exponential decay.

References to Chapter 2

[1] E. Yablonovitch, *Inhibited Spontaneous Emission in Solid-State Physics and Electronics*, Phys. Rev. Lett. 58, 2059 (1987).

[2] S. John, *Strong Localization of Photons in Certain Disordered Dielectric Superlattices*, Phys. Rev. Lett. 58, 2486 (1987).

[3] R. Sprik, B. A. van Tiggelen, and A. Lagendijk, *Optical emission in periodic dielectrics*, EPL (Europhysics Letters) 35, 265 (1996).

[4] P. Lodahl, A. F. van Driel, I. S. Nikolaev, A. Irman, K. Overgaag, D. Vanmaekelbergh, and W. L. Vos, *Controlling the dynamics of spontaneous emission from quantum dots by photonic crystals*, Nature 430, 654 (2004).

[5] J. Martorell and N. M. Lawandy, *Observation of inhibited spontaneous emission in a periodic dielectric structure*, Phys. Rev. Lett. 65, 1877 (1990).

[6] E. P. Petrov, V. N. Bogomolov, I. I. Kalosha, and S. V. Gaponenko, *Spontaneous Emission of Organic Molecules Embedded in a Photonic Crystal*, Phys. Rev. Lett. 81, 77 (1998).

[7] B. Y. Tong, P. K. John, Y. tang Zhu, Y. S. Liu, S. K. Wong, and W. R. Ware, *Fluorescence-lifetime measurements in monodispersed suspensions of polystyrene particles*, J. Opt. Soc. Am. B 10, 356 (1993).

[8] M. Megens, H. P. Schriemer, A. Lagendijk, and W. L. Vos, *Comment on "Spontaneous Emission of Organic Molecules Embedded in a Photonic Crystal"*, Phys. Rev. Lett. 83, 5401 (1999).

[9] A. Kress, F. Hofbauer, N. Reinelt, M. Kaniber, H. J. Krenner, R. Meyer, G. Böhm, and J. J. Finley, *Manipulation of the spontaneous emission dynamics of quantum dots in two-dimensional photonic crystals*, Phys. Rev. B 71, 241304 (2005).

[10] D. Englund, D. Fattal, E. Waks, G. Solomon, B. Zhang, T. Nakaoka, Y. Arakawa, Y. Yamamoto, and J. Vučković, *Controlling the Spontaneous Emission Rate of Single Quantum Dots in a Two-Dimensional Photonic Crystal*, Phys. Rev. Lett. 95, 013904 (2005).

[11] M. Fujita, S. Takahashi, Y. Tanaka, T. Asano, and S. Noda, *Simultaneous Inhibition and Redistribution of Spontaneous Light Emission in Photonic Crystals*, Science 308, 1296 (2005).

[12] K. Kounoike, M. Yamaguchi, M. Fujita, T. Asano, J. Nakanishi, and S. Noda, *Investigation of spontaneous emission from quantum dots embedded in two-dimensional photonic-crystal slab*, Electronic lett. 41, 1402 (2005).

[13] A. Badolato, K. Hennessy, M. Atatüre, J. Dreiser, E. Hu, P. M. Petroff, and A. Imamoğlu, *Deterministic Coupling of Single Quantum Dots to Single Nanocavity Modes*, Science 308, 1158 (2005).

[14] W.-H. Chang, W.-Y. Chen, H.-S. Chang, T.-P. Hsieh, J.-I. Chyi, and T.-M. Hsu, *Efficient Single-Photon Sources Based on Low-Density Quantum Dots in Photonic-Crystal Nanocavities*, Phys. Rev. Lett. 96, 117401 (2006).

[15] M. Kaniber, A. Kress, A. Laucht, M. Bichler, R. Meyer, M.-C. Amann, and J. J. Finley, *Efficient spatial redistribution of quantum dot spontaneous emission from two-dimensional photonic crystals*, App. Phys. Lett. 91, 061106 (2007).

[16] M. Kaniber, A. Laucht, T. Hürlimann, M. Bichler, R. Meyer, M.-C. Amann, and J. J. Finley, *Highly efficient single-photon emission from single quantum*

dots within a two-dimensional photonic band-gap, Phys. Rev. B 77, 073312 (2008).

[17] K. Hennessy, A. Badolato, D. Gerace, M. Atatüre, S. Gulde, S. Fält, E. L. Hu, and A. Imamoğlu, *Quantum nature of a strongly coupled single quantum dot-cavity system*, Nature 445, 896 (2007).

[18] I. S. Nikolaev, P. Lodahl, A. F. van Driel, A. F. Koenderink, and W. L. Vos, *Strongly nonexponential time-resolved fluorescence of quantum-dot ensembles in three-dimensional photonic crystals*, Phys. Rev. B 75, 115302 (2007).

[19] H. g, D. Englund, and J. Vučković, *Ultrafast photonic crystal nanocavity laser*, Nature Physics 2, 484 (2006).

[20] G. Schlegel, J. Bohnenberger, I. Potapova, and A. Mews, *Fluorescence Decay Time of Single Semiconductor Nanocrystals*, Phys. Rev. Lett. 88, 137401 (2002).

[21] B. Fisher, H.-J. Eisler, N. Stott, and M. Bawendi, *Emission Intensity Dependence and Single-Exponential Behavior In Single Colloidal Quantum Dot Fluorescence Lifetimes*, J. Phys. Chem. B 108, 143 (2004).

[22] R. Loudon, *The Quantum Theory of Light*, Oxford University Press, Oxford, 3rd edition (2000).

[23] E. M. Purcell, *Spontaneous Emission Probabilities at Radio Frequencies*, Phys. Rev. 69, 681 (1946).

[24] K. H. Drexhage, *Influence of a Dielectric Interface on Fluorescence Decay Time*, J. Lumin. 1-2, 693 (1970).

[25] D. Kleppner, *Inhibited Spontaneous Emission*, Phys. Rev. Lett. 47, 233 (1981).

[26] B. H. Bransden and C. J. Joachain, *Physics of atoms and molecules*, Longman Scientific & Technical, Essex (1983).

[27] L. Novotny and B. Hecht, *Principles of Nano-Optics*, Cambridge University Press, New York (2006).

[28] R. R. Chance, A. Prock, and R. Silbey, *Molecular fluorescence and energy transfer near interfaces*, Adv. Chem. Phys. 37, 1 (1978).

[29] V. P. Bykov, *Spontaneous Emission from a Medium with a Band Spectrum*, Sov. J. Quant. Elec. 4, 861 (1975).

[30] P. Y. Yu and M. Cardone, *Fundamentals of Semiconductors*, Springer, Berlin, 3rd edition (2001).

[31] K. M. Ho, C. T. Chan, C. M. Soukoulis, R. Biswas, and M. Sigalas, *Photonic band gaps in three dimensions: New layer-by-layer periodic structures*, Solid State Comm 89, 413 (1994).

[32] S.-Y. Lin and J. G. Fleming, *A three-dimensional optical photonic crystal*, J. Lightwave Tech 17, 1944 (1999).

[33] H. S. Sözüer, J. W. Haus, and R. Inguva, *Photonic bands: Convergence problems with the plane-wave method*, Phys. Rev. B 45, 13962 (1992).

[34] Y. A. Vlasov, X.-Z. Bo, J. C. Sturm, and D. J. Norris, *On-chip natural assembly of silicon photonic bandgap crystals*, Nature 414, 289 (2001).

[35] M. Qi, E. Lidorikis, P. T. Rakich, S. G. Johnson, J. D. Joannopoulos, E. P. Ippen, and H. I. Smith, *A three-dimensional optical photonic crystal with designed point defects*, Nature 429, 538 (2004).

[36] J. Vučković and Y. Yamamoto, *Photonic crystal microcavities for cavity quantum electrodynamics with a single quantum dot*, App. Phys. Lett. 82, 2374 (2003).

[37] P. Michler, A. Kiraz, C. Becher, W. V. Schoenfeld, P. M. Petroff, L. Zhang, E. Hu, and A. Imamoğlu, *A Quantum Dot Single-Photon Turnstile Device*, Science 290, 2282 (2000).

[38] T. Yoshie, A. Scherer, J. Hendrickson, G. Khitrova, H. M. Gibbs, G. Rupper, C. Ell, O. B. Shchekin, and D. G. Deppe, *Vacuum Rabi splitting with a single quantum dot in a photonic crystal nanocavity*, Nature 432, 200 (2004).

[39] O. Painter, R. K. Lee, A. Scherer, A. Yariv, J. D. O'Brien, P. D. Dapkus, and I. Kim, *Two-Dimensional Photonic Band-Gap Defect Mode Laser*, Science 284, 1819 (1999).

[40] H. Y. Ryu, M. Notomi, E. Kuramoti, and T. Segawa, *Large spontaneous emission factor (> 0.1) in the photonic crystal monopole-mode laser*, App. Phys. Lett. 84, 1067 (2004).

[41] H. G. Park, S. H. Kim, S. H. Kwon, Y. G. Ju, J. K. Yang, J. H. Baek, S. B. Kim, and Y. H. Lee, *Electrically Driven Single-Cell Photonic Crystal Laser*, Science 305, 1444 (2004).

[42] S. Strauf, K. Hennessy, M. T. Rakher, Y.-S. Choi, A. Badolato, L. C. Andreani, E. L. Hu, P. M. Petroff, and D. Bouwmeester, *Self-Tuned Quantum Dot Gain in Photonic Crystal Lasers*, Phys. Rev. Lett. 96, 127404 (2006).

[43] J. D. Joannopoulos, R. D. Meade, and J. N. Winn, *Photonic Crystals - Molding the Flow of Light*, Princeton University Press, Princeton NJ (1995).

[44] A. F. Koenderink, M. Kafesaki, C. M. Soukoulis, and V. Sandoghdar, *Spontaneous emission rates of dipoles in photonic crystal membranes*, J. Opt. Soc. Am. B 23, 1196 (2006).

[45] S. G. Johnson and J. D. Joannopoulos, *Block-iterative frequency-domain methods for Maxwell's equations in a planewave basis*, Opt. Express 8, 173 (2001).

[46] D. Bimberg, M. grundmann, and N. N. Ledentsov, *Quantum Dot Heterostructures*, Wiley, Chichester (1999).

[47] S. L. Chuang, *Physics of Optoelectronic Devices*, Wiley-Interscience, New York (1995).

[48] M. Bayer, G. Ortner, O. Stern, A. Kuther, A. A. Gorbunov, A. Forchel, P. Hawrylak, S. Fafard, K. Hinzer, T. L. Reinecke, S. N. Walck, J. P. Reithmaier, F. Klopf, and F. Schäfer, *Fine structure of neutral and charged excitons in self-assembled In(Ga)As/(Al)GaAs quantum dots*, Phys. Rev. B 65, 195315 (2002).

[49] S. Cortez, O. Krebs, P. Voisin, and J. M. Gérard, *Polarization of the interband optical dipole in InAs/GaAs self-organized quantum dots*, Phys. Rev. B 63, 233306 (2001).

[50] G. A. Narvaez, G. Bester, and A. Zunger, *Dependence of the electronic structure of self-assembled (In,Ga)As/GaAs quantum dots on height and composition*, J. Appl. Phys. 98, 043708 (2005).

[51] I. Kegel, T. H. Metzger, A. Lorke, J. Peisl, J. Stangl, G. Bauer, J. M. García, and P. M. Petroff, *Nanometer-Scale Resolution of Strain and Interdiffusion in Self-Assembled InAs/GaAs Quantum Dots*, Phys. Rev. Lett. 85, 1694 (2000).

[52] D. M. Bruls, J. W. A. M. Vugs, P. M. Koenraad, H. W. M. Salemink, J. H. Wolter, M. Hopkinson, M. S. Skolnick, F. Long, and S. P. A. Gill, *Determination of the shape and indium distribution of low-growth-rate InAs quantum dots by cross-sectional scanning tunneling microscopy*, App. Phys. Lett. 81, 1708 (2002).

[53] S. Lee, O. L. Lazarenkova, P. von Allmen, F. Oyafuso, and G. Klimeck, *Effect of wetting layers on the strain and electronic structure of InAs self-assembled quantum dots*, Phys. Rev. B 70, 125307 (2004).

[54] L.-W. Wang and A. Zunger, *Linear combination of bulk bands method for large-scale electronic structure calculations on strained nanostructures*, Phys. Rev. B 59, 15806 (1999).

[55] G. A. Narvaez, G. Bester, A. Franceschetti, and A. Zunger, *Excitonic exchange effects on the radiative decay time of monoexcitons and biexcitons in quantum dots*, Phys. Rev. B 74, 205422 (2006).

3. ENERGY DEPENDENCE OF THE OSCILLATOR STRENGTH AND QUANTUM EFFICIENCY OF INAS QUANTUM DOTS MEASURED BY A MODIFIED LOCAL DENSITY OF OPTICAL STATES

In this chapter we present measurements of the radiative and non-radiative decay rates of InAs quantum dots. The rates are measured with an unprecedented accuracy using a modified local density of optical states. The rates allow for a determination of important optical properties of the quantum dots, such as e.g., the quantum efficiency and the oscillator strength. By probing different emission energies, we measure the energy dependence of these properties. Surprisingly, the radiative decay rate and thus the oscillator strength decrease with energy. The quantum efficiency and the oscillator strength are also found to be dependent on excitation density. Finally a series of time-resolved measurements of the spontaneous emission from colloidal CdSe quantum dots are presented.

3.1 Introduction

Quantum dots are very interesting light sources for use in solid state quantum optics experiments [1–6] as well as in future quantum optics devices. Exciting experiments have culminated in the demonstration of strong coherent coupling between a single quantum dot and the optical mode of a cavity [1–3]. These experiments are based on the control of spontaneous emission obtained by nano-structuring the dielectric environment surrounding the quantum dots. The dielectric nano-structures, i.e., photonic crystals, micro-pillars, and micro-discs, modify the local density of optical states (LDOS) [7], and hereby affect the radiative recombination rate of the embedded quantum dots.

The degree to which spontaneous emission is controlled is determined by three factors: i) the magnitude of the LDOS modifications, ii) the oscillator strength of the quantum dot transition, and iii) the non-radiative decay rate of the quan-

tum dot transition. While the modifications of the LDOS is controlled by the surrounding environment, the oscillator strength and the non-radiative decay rate are intrinsic properties of the quantum dot. The oscillator strength determines the strength of the coupling between the quantum dot transition and the optical field, and thus a decisive parameter in obtaining strong coupling. The oscillator strength may be ingeniously tailored due to the size dependence of the exciton wavefunctions [8, 9] or by the application of an electric field, causing a separation of the electron and hole wave functions [10, 11]. The non-radiative decay is unaffected by modifications of the LDOS and therefore sets an upper limit on the lifetime of the quantum dot exciton state. An upper bound on the inhibition of spontaneous emission rate is thus set by the quantum efficiency, i.e., the contribution of non-radiative processes to the total decay of the quantum dot. Surprisingly, the exact size dependence of the optical properties, i.e., the oscillator strength and the quantum efficiency, of the quantum dot exciton has remained an open question. Understanding these optical properties is essential to optimally engineer quantum dots for enhanced light-matter interaction.

In this chapter we present accurate measurements of the quantum efficiency and the oscillator strength of the quantum dot exciton ground state. We furthermore determine their dependence on emission energy and thus obtain knowledge of their size dependence. The measurements are performed by employing the modifications in the LDOS caused by a nearby interface. The simple system, i.e., the dielectric interface, offers the great advantage that the LDOS can be calculated exactly [12,13], whereby the quantum efficiency and the oscillator strength are determined without any adjustable parameters. The only parameter to be specified is the distance between the quantum dots and the interface which can be measured accurately. In contrast, alternative methods for determining the oscillator strength, e.g., absorption measurements [14–16], require estimates of parameters such as the density of quantum dots and the beam waist of excitation beam, which is hard to do accurately.

Recently the interface method has been employed to obtain knowledge of the quantum efficiency in two different material systems: ensembles of Si nanocrystals [17] and individual CdSe colloids [18]. In contrast to Ref. [17] our detailed understanding of the decay dynamics of InAs quantum dots allow us to directly extract physically meaningful parameters, i.e., the radiative and non-radiative rates, and thus obtain both the quantum efficiency and the oscillator strength. The measurements reported in Ref. [18] are performed on a single quantum dot and

it is therefore only possible to obtain two data points. This limit is not imposed on the ensemble measurements as they rely on the statistically averaged ensemble properties. For large sub-ensembles these properties can safely be assumed to be identical. We can thus obtain measurements for many different distances whereby the validity of the model can be confirmed. We do indeed identify a range of distances close to the interface in which the validity of the model is compromised. This readily suggests that several data points much be acquired for an indisputable determination of the decay rates.

3.2 Dipole emission near a dielectric interface

The total decay rate of an excited emitter is the sum of the radiative and the non-radiative decay rates, c.f. Sec. 2.2.4. To separate these two contributions, we exploit the periodic variation in the LDOS caused by reflections of the electric field in a nearby interface. While the non-radiative decay rate is expected to be constant, the radiative decay rate depends linearly on the LDOS and will thus depend explicitly on the distance to the interface. This method was pioneered by Drexhage who studied the radiation pattern and lifetime of europium ions positioned at known distances in front of a silver mirror [12]. Drexhage and co-workers demonstrated that the presence of the interface altered the lifetime of the molecules substantially. For large distances to the interface the lifetime was observed to oscillate as a function of the distance. The oscillation occurs since part of the emitted field is reflected in the interface, and arrives back at the position of the emitter where it interferes with the directly emitted field.

The behaviour of an emitter near a dielectric interface can be modelled exactly by calculating the projected LDOS as a function of the distance to the interface. From a classical point of view this corresponds to calculating the electric field at the dipole position caused by the dipole emission itself, i.e., taking into account both the emitted field and the reflected field. This can be done elegantly by using the dyadic Green's functions formalism as rigorously derived in Refs. [19] and [20] and briefly discussed in Sec. 2.1.1. In Fig. 3.1 calculations of the normalized LDOS are shown as a function of distance to an air-GaAs interface. The calculations, which are performed for two different dipole orientations, are obtained using experimentally relevant parameters: emission energy, $\hbar\omega = 1.20\,\mathrm{eV}$ and refractive index, $n_{\mathrm{GaAs}} = 3.5$. The Dyadic Green's functions for a dipole emitter near a dielectric interface is derived in [20, Chap. 10], which the reader is asked to consult for further details regarding the calculation.

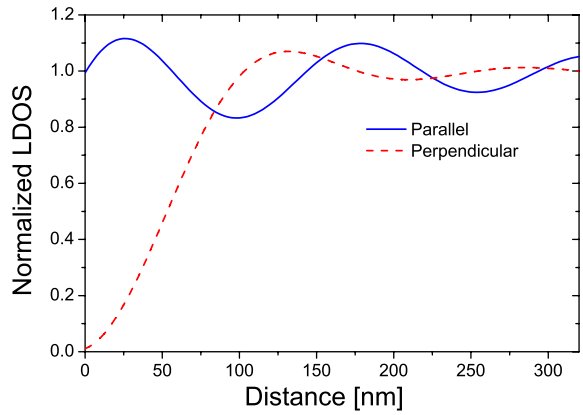

Fig. 3.1: The calculated LDOS normalized to the density of optical states in bulk GaAs. The calculation has been performed for an air-GaAs interface, an emission energy of 1.20 eV and for two different dipole orientations: parallel to the interface (solid, blue line) and perpendicular to the interface (dashed, red line).

The total decay rate of an emitter placed at a distance z to the interface is given as the sum of the non-radiative and radiative decay, where the latter is related to the LDOS by Fermi's Golden Rule (Eq. (2.14))

$$\begin{aligned} \gamma(\omega, z) &= \gamma_{\mathrm{nrad}}(\omega) + \gamma_{\mathrm{rad}}(\omega, z) \\ &= \gamma_{\mathrm{nrad}}(\omega) + \frac{\pi\omega}{3\hbar\epsilon_0}|\boldsymbol{\mu}(\omega)|^2 \rho_\mu(\omega, z), \end{aligned} \tag{3.1}$$

where $\boldsymbol{\mu}(\omega)$ is the (energy dependent) transition dipole moment and $\rho_\mu(\omega, z)$ is the projected LDOS. By defining the radiative decay rate for an emitter in a homogeneous medium $\gamma_{\mathrm{rad}}^{\mathrm{hom}}(\omega) = \frac{\pi\omega}{3\hbar\epsilon_0}|\boldsymbol{\mu}(\omega)|^2\rho(\omega)$, where $\rho(\omega)$ is the usual density of optical states (DOS) in a homogeneous medium, the measured total decay rate can be expressed as

$$\gamma(\omega, z) = \gamma_{\mathrm{nrad}}(\omega) + \gamma_{\mathrm{rad}}^{\mathrm{hom}}(\omega)\frac{\rho_\mu(\omega, z)}{\rho(\omega)}. \tag{3.2}$$

As $\rho_\mu(\omega, z)/\rho(\omega)$ can be calculated exactly, $\gamma_{\mathrm{rad}}^{\mathrm{hom}}(\omega)$ and $\gamma_{\mathrm{nrad}}(\omega)$ can be determined with high accuracy. The superscript hom is used to underline that $\gamma_{\mathrm{rad}}^{\mathrm{hom}}(\omega)$ is the radiative decay rate for an emitter in a homogeneous medium.

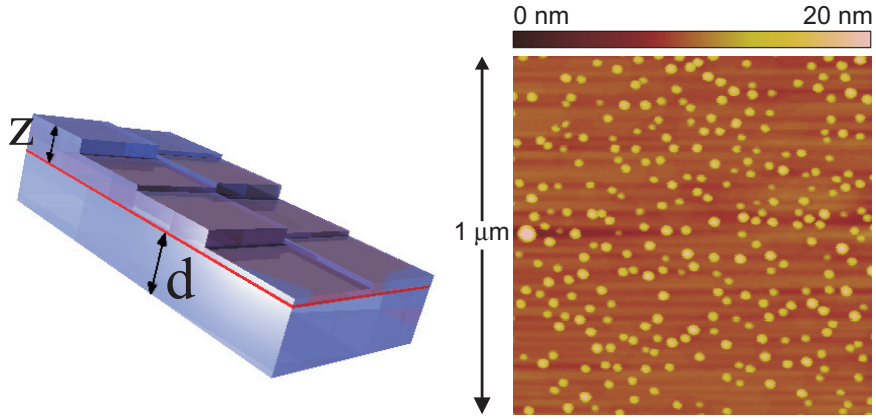

Fig. 3.2: **Left:** A sketch of 8 samples. The thin red layer indicates the quantum dot layer, while the surrounding GaAs is shown in blue. The distance z is varied between 30 nm and 300 nm for the different samples, while the distance d to the underlying AlAs layer is 650 nm, identical for all samples. **Right:** An atomic force microscopy scan of a uncapped layer of InAs quantum dots grown using identical parameters as for the quantum dot layer embedded in the GaAs. A quantum dot density of $\sim 300\,\mu\text{m}^{-2}$ is found.

3.3 Measuring the oscillator strength and quantum efficiency of InAs quantum dots

To determine the radiative and non-radiative decay rates of InAs quantum dots we have performed a series of time-resolved measurements of the spontaneous emission from quantum dots placed at 30 different distances to a air-GaAs interface. This experiment is very well suited for the epitaxially grown InAs quantum dots as the layer containing the quantum dot ensemble is very well defined within the wafer structure as well as the quantum dots are identically oriented.

3.3.1 Sample preparation

The wafer used for the experiments (NBI-167) is grown by molecular beam epitaxy on a GaAs (100) substrate where 2.0 monolayers of InAs are deposited at 524° C followed by a 30 s growth interrupt and deposition of a 300 nm thick GaAs cap. The quantum dot density is measured to be $\sim 300\,\mu\text{m}^{-2}$ using atomic force microscopy (AFM) on an uncapped quantum dot layer grown for this purpose, cf. Fig. 3.2(b). A 50 nm thick layer of AlAs is deposited 650 nm below the quantum

dots for an optional epitaxial lift-off. The wafer is processed in 5 steps consisting of standard UV lithography and wet chemical etching, whereby samples with different distances between the quantum dots and the interface are fabricated on the same wafer, see Figure 3.2(a). To obtain smooth surfaces and keep the etch rates low a mixture of $H_3PO_4(85\%) : H_2O_2(30\%) : DI\,H_2O$ in the ratio 3:1:60 was used [21]. In total, 30 samples are obtained covering distances from 30 to 300 nm. For the sample with the larges distance (not etched) a value of $z = 302.3 \pm 2.1$ nm is determined using secondary ion mass spectroscopy (SIMS) and surface profiling. The distances for the remaining samples are determined by surface profiling combined with the SIMS measurement. Five successive surface profiles are acquired on each sample whereby a typical precision of ± 3.0 nm is obtained.

3.3.2 Experimental setup

The setup used for the experiments is depicted in Fig. 3.3. The sample is placed inside a closed-cycle cryostat keeping the sample temperature at 12 K. The quantum dots can be optically excited using either a wavelength-tunable mode-locked Ti:sapphire laser (Mira 900) delivering $\sim$300 fs long pulses at a repetition rate of 82 MHz or a pulsed laser diode (PicoQuant, PDL-800) with a variable repetition rate between 5 to 80 MHz and a fixed wavelength of 781 nm (1.59 eV). The spontaneous emission is collected by the lens L2, c.f. Fig. 3.3. The effective numerical aperture is 0.32 limited by the cryostat windows. The lens system consisting of L2 and L3 image the sample onto the pinhole (PH) magnified by a factor of 10. The pinhole is used for spatial selection and can be changed depending on the size of the studied structures. A flip mirror (M) can be inserted in front of the pinhole to direct the image onto a CCD camera used for positioning the sample. The lens system consisting of L4 and L5 creates an image of the sample (pinhole) on the entrance slit of the spectrometer (SpectraPro, SP-2500i). The magnification is 0.4, resulting in a total magnification of 4 whereby the numerical aperture of the spectrometer (0.077) is matched. The spectrometer is used with a 150 g/mm grating and with an entrance slit width of either 60 or 150 µm depending on whether spectra are acquired using the CCD array, or the avalanche photo diode (APD) is used for time-resolved single-photon counting. This results in spectral resolutions of 1.0 meV and 2.6 meV. Two different APDs can be used: i) a fast APD (Micro Photon Devices, PDM-50CT) with a full-width at half-maximum value of the instrument response of 48 ps but a low detection efficiency of 5.5% (at 900 nm), and ii) an APD (PerkinElmer, SPCM-CD3226) with a high detection efficiency of 25%

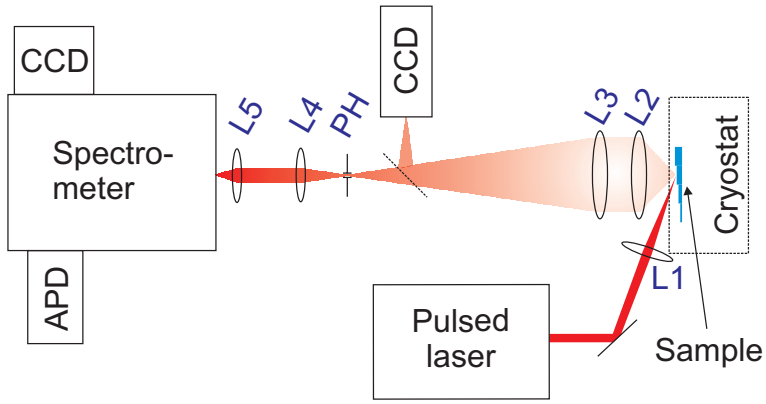

Fig. 3.3: Sketch of the experimental setup used throughout this thesis. The lenses L2 ($f = 75\,\mathrm{mm}$) and L3 ($f = 750\,\mathrm{mm}$) creates a 10-fold enlarged image of the sample on the pinhole (PH) which is used for spatial selection. To match the numerical aperture of the spectrometer the lenses L4 ($f = 150\,\mathrm{mm}$) and L5 ($f = 60\,\mathrm{mm}$) image the sample (pinhole) on the entrance slit with a magnification of 0.4. The focusing optics for the excitation beam is simplified to one lens L1. In pratice this lens can be exchanged to obtain different sizes of the excitation spot and to accommodate the different beam waist of the two lasers. The size of the excitation spot is obtained by imaging the photoluminescence on the CCD via the flip mirror (M).

(at 900 nm) and a full-width at half-maximum value of the instrument response of 310 ps. The APDs are connected to a time-correlated single-photon counting system (PicoQuant, PicoHarp300) with a resolution of 4 ps and a dead time of ~ 85 ns.

3.3.3 Spontaneous emission from InAs quantum dots

Time integrated emission spectra acquired at different excitation densities are shown in Fig. 3.4(a). For the lowest excitation density the spectrum corresponds to emission from the inhomogenously broadened ground state transitions. As the excitation density is increased the emission spectrum broadens towards higher energies due to emission from the excited states. At high intensities emission from the wetting layer (denoted by D in the figure) is dominating. Three additional peaks appear in the spectra. Denoted by: A) is the band gap exciton of GaAs at 1.513 eV, B) is the emission from carbon defects in GaAs at 1.493 eV [22], and C)

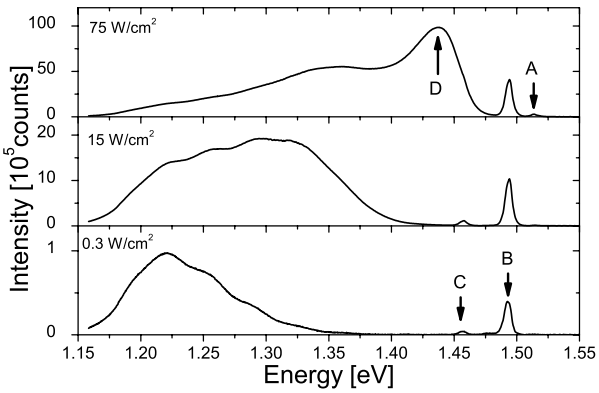

Fig. 3.4: Emission spectra from the quantum dot ensemble under various excitation intensities: at 0.3 W/cm^2 only emission from the ground state is observed, at 5 W/cm^2 additional emission from the excited states appears, and at 75 W/cm^2 emission from the wetting layer (D) becomes dominant. The peaks indicated by arrows A, B and C are related to bulk GaAs, see text for further details.

is a phonon replica of B) at 1.457 eV.

From the time-resolved measurements, we find that decay of spontaneous emission from the quantum dot ground state excitons can be well described by a bi-exponential model when it is studied within a time range of $\sim 13\,\mathrm{ns}^{-1}$. This is in accordance with the bi-exponential decay derived from the rate equations in Sec.2.2.4. In Fig. 3.5(a) the time-resolved photoluminescence from two quantum dot ensembles positioned at distances of $z = 109\,\mathrm{nm}$ and $z = 170\,\mathrm{nm}$ from the GaAs-air interface are shown. The fits of a bi-exponential model, $N(t) = A_\mathrm{f} e^{-\Gamma_\mathrm{f} t} + A_\mathrm{s} e^{-\Gamma_\mathrm{s} t} + C$, to the data are shown by the red lines. The background level C is determined by the measured dark-count rate and after-pulsing probability of the detector. The choice of a bi-exponential model is confirmed by the weighted residuals (c.f. Figs. 3.5(b) and (c)) as they are randomly distributed around a mean value of zero and thus result in low χ^2_R-values of 1.17 and 1.11.[1]

[1] The weighted residual is defined as $W_k = \frac{[N(t_k) - N_c(t_k)]}{\sigma_k}$, where $N(t_k)$ are the measured data, $N_c(t_k)$ the calculated model, $\sigma_k = \sqrt{N(t_k)}$ the standard deviation, and the subscript k denotes that the data is assigned discrete times. The model is fitted to the data using a least-squares approach in which the goodness-of-fit parameter $\chi^2 = \sum_k W_k^2$ is minimized. Here the sum over k runs over all n data points in the decay curve. Since χ^2 depends on the number of

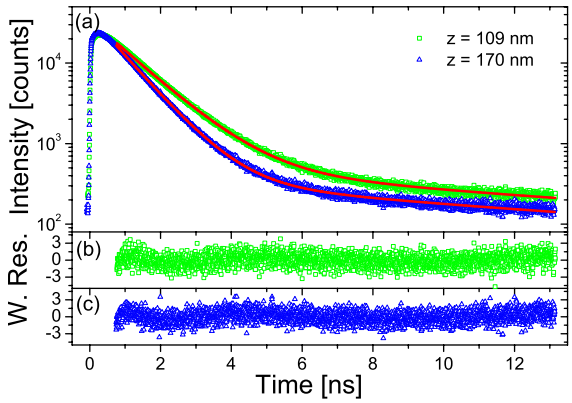

Fig. 3.5: **(a)** Decay of the spontaneous emission recorded at 1.204 eV for two different distances to the interface of $z = 109$ nm (green, upper curve) and $z = 170$ nm (blue, lower curve). The solid red lines are bi-exponential fits **(b)** The weighted residual for the bi-exponential fit for $z = 109$ nm (green, upper curve) resulting in a χ^2_R-value of 1.17. **(c)** The weighted residual for the bi-exponential fit for $z = 170$ nm (blue, lower curve) resulting in a χ^2_R-value of 1.11.

The specific measurements shown in Fig. 3.5(a) are obtained for optical excitation in the wetting layer states and detected for an emission energy of 1.204 eV, but similar χ^2_R-values close to unity are obtained for excitation in the GaAs barrier states. The fast decay takes place on a time scale of about 1 ns corresponding to the decay of bright ground state excitons in InAs quantum dots [23]. The slow decay time is approximately 10 ns and is due to recombination of dark excitons [24, 25] as will be discussed in detail in Chapter 5. In the present section we will only focus on the fast decay rate.

Experimental conditions

To measure the oscillator strength and quantum efficiency of the ground state transition accurately, it is important to keep a low and constant excitation density for all samples. The density must be kept low to avoid population of the bi-

data points, the reduced χ^2 is a better measure of the goodness of fit. It is defined as $\chi^2_R = \frac{\chi^2}{n-p}$, where n is the number of data points and p is the number of adjustable parameters in the model.

exciton and excited states, since this affects the oscillator strength, c.f. Sec. 5.3. A constant density is needed as the fast decay rate is weakly dependent on the excitation density, as will be discussed in Sec. 5.3. A constant excitation density is most easily obtained by exciting electron-hole pairs in the wetting layer states, as the thickness of the wetting layer is constant for all 30 samples, as opposed to the GaAs barriers. The excitation is therefore performed at an energy of 1.45 eV, corresponding to the energy of the wetting layer states, using the mode-locked Ti:sapphire laser. The excitation spot has a diameter of $\sim$250 µm and the excitation density is kept at 7 W/cm^2. By comparing the intensity and spectrum with those obtained for optical pumping of the GaAs barrier states, we find that this corresponds to an excitation density of less than 0.3 excitons per quantum dot.[2] With such low excitation densities the formation of bi-excitons and the filling of higher excited states can be neglected, i.e., only light from the quantum dot ground state is observed. The calculated excitation density is also supported by emission spectra acquired at different excitation intensities. The spectra stays unaffected for an excitation intensity < 15 W/cm^2, while the excited states appear for higher densities. The detection energy is varied between 1.170 eV and 1.272 eV to probe different sub-ensembles of the inhomogenously broadened ground state. The time resolution is 48 ps and the spectral resolution of the monochromator (2.6 meV) is narrow relative to the bandwidth of the LDOS changes.

Data analysis

The two decay curves shown in Fig. 3.5 show a clear change with distance to the interface. The complete series of decay rates obtained from the measurements acquired at an energy of 1.204 eV are presented in Figure 3.6(a) as a function of distance from the quantum dots to the interface. A damped oscillation of the total decay rate with distance is observed. The data are compared to the LDOS calculated for GaAs (assuming $n = 3.5$) and projected onto a dipole orientation parallel to the interface (solid blue line). Only the parallel projection is relevant, since the orientation of the transition dipole moments has been observed to be predominantly in the plane parallel to the interface [26]. This is also consistent with the formation of the ground state exciton from a hole in the heavy hole band and an electron in the conductance band, resulting in an in-plane polarized emission pattern. The low χ^2_R-values obtained from the respective fits of the bi-exponential model are shown in Fig. 3.6(b), confirming that all the different decay

[2] See. App. A for further details.

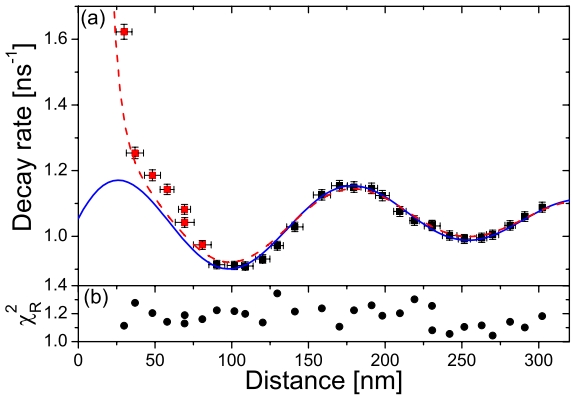

Fig. 3.6: **(a)** Measured decay rates versus distance z to the GaAs-air interface (squares), acquired at E = 1.204 eV. Calculated LDOS projected onto a dipole orientation parallel to the interface (solid blue line). Calculated LDOS including dissipation at the surface (dashed red line). **(b)** The χ^2_R-values obtained for the various fits.

curves are well described by the bi-exponential model.

For distances of $z \geq 75\,\text{nm}$ we find an excellent agreement between the measured decay rates and theory. This explicitly confirms the validity of the theoretical model, thus it can be used to reliably extract properties of the emitter. For quantum dots closer than 75 nm to the GaAs-air interface the measured decay rates are systematically larger than the calculated rates. We identify three different processes which could lead to an increase of the decay rate near the surface: i) tunnelling of carriers from the quantum dot to the surface, ii) absorption and scattering at the interface caused by surface roughness, or iii) a breakdown of the dipole approximation since the size of the emitter ($\sim$ size of the quantum dot) becomes non-negligible when the distance to the interface becomes small. We rule out tunnelling as a possible cause; surface-induced tunnelling of quantum dot carriers has been reported to be important only within distances of less than $\sim 15\,\text{nm}$ from the surface [27]. In order to examine whether case ii) could be a plausible cause, we include a thin absorbing surface layer in the LDOS calculations. We obtain qualitative agreement between theory and measurements by including a 5 nm thick layer with refractive index of $3.5 + \text{i}\,1.0$ as shown by the dashed line

in Fig. 3.6(b). iii) The measurements reported by Drexhage [12] and rigorously analysed by Chance *et al.* [13] concern emitters (molecules) which are very small compared to the size of the InAs quantum dots. The finite size of the quantum dots can have an effect on the decay rate, but for a realistic quantum dot radius of 10 nm and in the case of an air-semiconductor interface the effect has been evaluated to be negligible [28].

For quantum dots sufficiently far away from the interface, the influence of any surface effects is negligible, and the data can be used to reliably extract the radiative and non-radiative decay rates. The measured decay rates (from Fig. 3.6(a)) are shown in Fig. 3.7(a) as a function of the LDOS calculated for the respective distances. The measured rates clearly display the expected linear relation on the LDOS. To determine which data points are influenced by surface effects unaccounted for by Eq. (3.2) a linear regression analysis is used. The linear correlation parameters $|r|$ obtained as the data close to the interface are excluded point by point are shown in Fig. 3.7(b). After exclusion of the seven closest data points the correlation parameter converges to unity (> 0.99), hence Eq. (3.2) is valid. By fitting Eq. (3.2) to the remaining data points we determine the radiative and non-radiative decay rates at 1.204 eV to be $\gamma_{\mathrm{rad}}^{\mathrm{hom}} = 0.95 \pm 0.03\,\mathrm{ns}^{-1}$ and $\gamma_{\mathrm{nrad}} = 0.11 \pm 0.03\,\mathrm{ns}^{-1}$. It should be noted that by fitting Eq. (3.2) to the data, the phase and period of the oscillation shown in Fig. 3.6(a) are given by the distance and the emission energy. Thus, only the offset (the non-radiative rate) and the amplitude (the radiative rate) are obtained from the fitting.

Having obtained the radiative and non-radiative decay rates the quantum efficiency is readily determined to be $QE = 90 \pm 4\%$ for ground state excitons having an emission energy of 1.204 eV. This result confirms that the InAs quantum dots have a high quantum efficiency, even though the non-radiative contributions cannot be neglected. An even higher intrinsic quantum efficiency can be obtained by selecting the quantum dots emitting on the red side (low energy) of the inhomogenously broadened ground state spectrum as will be discussed below.

The oscillator strength is a dimensionless measure of the transition strength relative to the transition strength of a classical electrical oscillator, i.e., a sinusoidally oscillating electron with resonance frequency ω which is embedded in a dielectric material characterized by $\epsilon\,(= n^2)$. Using the radiative decay rate of a classical electrical oscillator $\gamma_{\mathrm{rad}}^{\mathrm{CEO}}$, the oscillator strength can be expressed as [29, Chap. 2]:

$$f_{\mathrm{osc}} = \frac{\gamma_{\mathrm{rad}}}{\gamma_{\mathrm{rad}}^{\mathrm{CEO}}} = \frac{6\pi m_0 \epsilon_0 c_0^3}{n e^2 \omega^2}\,\gamma_{\mathrm{rad}} = \frac{2 m_0 \omega}{e^2 \hbar}|\boldsymbol{\mu}|^2, \tag{3.3}$$

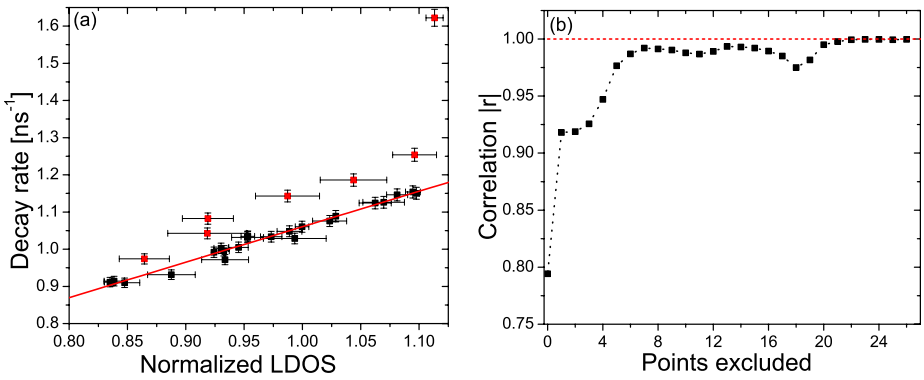

Fig. 3.7: **(a)** Measured decay rates versus the LDOS calculated for the respective distances. **(b)** The linear correlation parameter, which is obtained as the data close to the interface are excluded point by point, converges towards unity for exclusion of seven or more data points.

where the decay rate in a homogeneous medium (Eq. (2.10)) has been used to express the oscillator strength in terms of the transition dipole moment. For the quantum dots emitting at 1.204 eV, the measured value of $\gamma_{\mathrm{rad}}^{\mathrm{hom}}$ results in an oscillator strength of $f_{\mathrm{osc}} = 13.0 \pm 0.4$.[3] For comparison various estimates of the oscillator strength based on absorption measurements have been reported in the literature and are generally in the range of f_{osc}=5-10 [14, 15]. However, the technique implemented here provides unprecedented precision since it only relies on accurate measurements of the distance of the quantum dots to the interface and is independent of, e.g., the quantum dot density.

3.4 *Energy dependence of the oscillator strength and quantum efficiency*

We determine the energy dependence of the oscillator strength and the quantum efficiency by performing the time-resolved measurements for different emission energies. The inhomogeneous broadening of the emission spectrum reflects the different sizes of quantum dots, i.e., small quantum dots have a large quantization energy and hence high emission energies and *vice versa*. By probing different

[3] This corresponds to a transition dipole moment of $(10.3 \pm 0.15) \cdot 10^{-29}$ C m or equivalently 30.9 ± 0.4D.

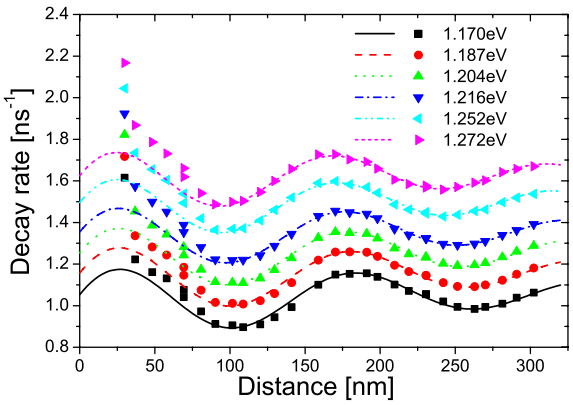

Fig. 3.8: Decay rates versus distance for all six detection energies (solid symbols) and the corresponding theory curve (lines). Each curve is offset by an additional 0.1 ns^{-1} for clarity.

energies we can thus probe quantum dots of different sizes. The measured decay rates versus distance are shown in Fig. 3.8 together with the respective theoretical calculations for all six energies. Using the method described in the previous section, we derive the radiative and non-radiative decay rates (shown in Fig. 3.9) and obtain their dependence on emission energy.

Surprisingly, the radiative decay rate is found to decrease with increasing energy as opposed to the total decay rate which, caused by the drastic increase in the non-radiative recombination rate, increases slightly with increasing energy. The reduction of the radiative decay rate with energy can only be explained by a reduction in the overlap of the electron and hole wavefunctions as the size of the quantum dot is reduced; this will be discussed in details in Chapter 4. The increased non-radiative recombination rate at higher energies (small quantum dot sizes) could indicate trapping of carriers at the quantum dot's surface, since the relative importance of the surface is large for small quantum dots. While such a size dependence would be general for all quantum dots, the absolute values of the non-radiative rates would most likely depend on sample growth.

The energy dependence of the oscillator strength and the quantum efficiency are presented in Figure 3.10. Both quantities are seen to decrease with increasing energy. The measured oscillator strengths are in good agreement with the theo-

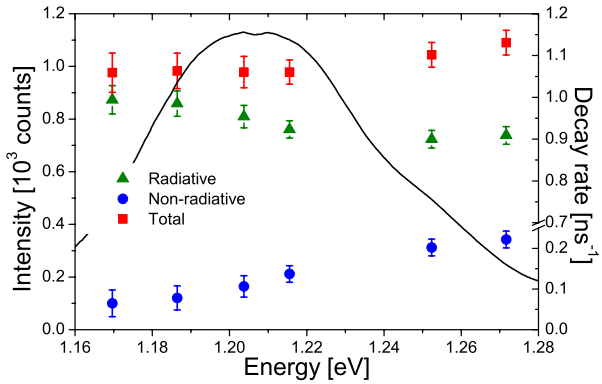

Fig. 3.9: Left axis: Photoluminescence from the inhomogenously broadened ground state measured at $z = 281\,\mathrm{nm}$ (solid line). Right axis: Radiative (green triangles), non-radiative (blue circles) and total (red squares) decay rates versus emission energy.

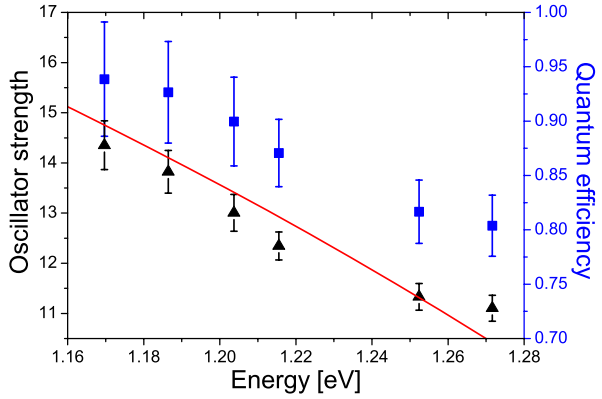

Fig. 3.10: Left axis: Measured oscillator strength versus energy (triangles) and theoretical calculation (solid, red line) based on effective mass approximation, c.f. Chapter 4. Right axis: quantum efficiency (squares) versus energy.

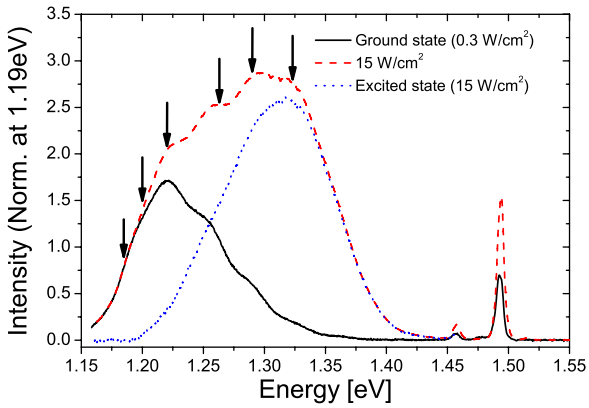

Fig. 3.11: Spectra acquired under excitation intensities of 0.3 W/cm^2 (solid black line) and 15 W/cm^2 (dashed red line). While the spectrum obtained at weak excitation corresponds to emission from the ground state, the emission from the excited states can be obtained by subtracting the ground state emission from the emission spectrum (dotted blue line).

retical calculation shown by the solid red line. The calculation will be explained in details in Chapter 4. The quantum efficiency decreases from around 95% to 80% and the oscillator strength from 14.5 to 11 over the emission spectrum. This result shows that large quantum dots with a high exciton confinement potential possess much better optical properties than small quantum dots. We thus make the general statement that strong coupling is most easily obtained for large InAs quantum dots.

3.5 Oscillator strength and quantum efficiency probed under strong excitation

To study how the oscillator strength and the quantum efficiency are affected by additional carriers in and around the quantum dot, a series of measurements are performed under a strong excitation of ~ 20 excitons per quantum dot.

Experimental conditions

The excitation is done by introducing carriers in the GaAs barrier at an energy of 1.63 eV. Apart from the excitation energy the remaining experimental parameters are kept as in Sec. 3.3. To compensate for the various thickness of the GaAs barrier, which will cause variations in the excitation density, the intensity is adjusted in order to obtain similar spectra from the different samples. The intensity is thus varied between 12 W/cm^2 and 30 W/cm^2. This method does, however, result in relative large uncertainties on the excitation densities, and it would have been preferable to obtain the high excitation densities by excitation in the wetting layer instead. For these measurements the spectral resolution of the monochromator is adjusted 0.7 meV and the time-resolution of the setup is 310 ps .

Two emission spectra from the sample with $z = 302$ nm are shown in Fig. 3.11. For excitation intensities ≤ 0.3 W/cm^2 the spectrum is independent of excitation intensity, and it can thus be concluded to correspond to emission from the inhomogenously broadened ground state. At an excitation intensity of 15 W/cm^2 the emission spectrum clearly displays emission from the excited states causing the spectrum to broaden towards higher energies. The difference of the two spectra, shown by the dotted blue line, corresponds to the emission spectrum stemming from the excited states. Time-resolved measurements are performed at six different emission energies in the range from 1.184 eV to 1.322 eV as marked by the arrows in Fig. 3.11. At the three lowest energies the excited states do not contribute substantially to the luminescence, while they become successively more and more dominating for the three highest energies.

Time-resolved measurements

The spectral overlap of the ground and excited states for energies above ~ 1.24 eV is also apparent in the time-resolved measurements. In Fig. 3.12(a) two decay curves obtained for the sample with $z = 159$ nm at energies of 1.201 eV and 1.322 eV are shown. At 1.201 eV, where the contribution from excited states is negligible, the decay curve is again very well modelled as a bi-exponential decay resulting in a weighted residual which is randomly distributed around zero, c.f. Fig. 3.12(b). The rates obtained for the fast (~ 1 ns^{-1}) and slow (~ 0.1 ns^{-1}) components are similar to those found in the weak excitation regime. When the contribution from the excited states becomes substantial, as exemplified by the decay curve obtained at 1.322 eV, an initial fast decay appears in the measurements. We attribute this initial decay to spontaneous emission from the excited states.

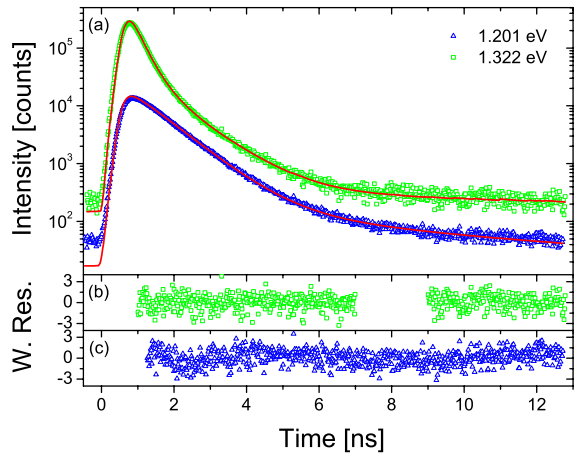

Fig. 3.12: **(a)** Decay curves obtained for the sample with $z = 159$ nm at 1.201 eV (blue triangles) and 1.322 eV (green squares). **(b)** The weighted residual for the triple-exponential fit for 1.32 eV (green, upper curve) resulting in a χ^2_R-value of 1.11. **(c)** The weighted residual for the bi-exponential fit for 1.32 eV (blue, lower curve) resulting in a χ^2_R-value of 1.17. The models have only been fitted to the data in the ranges indicated by the residuals, but to verify the proper adjustment of the time axis, the models are calculated and shown over the complete time range.

The initial decay is very well accounted for by adding a third term to the model whereby it becomes triple-exponential, $N(t) = A_{\mathrm{ex}}e^{-\Gamma_{\mathrm{ex}}t} + A_{\mathrm{f}}e^{-\Gamma_{\mathrm{f}}t} + A_{\mathrm{s}}e^{-\Gamma_{\mathrm{s}}t} + C$. Here the subscripts ex denotes the contribution from the excited states. The fit of the triple-exponential model is shown by the solid red line, and the corresponding weighted residual is shown in Fig. 3.12(c).

Excited states

The decay rates of the excited states Γ_{ex}, shown in Fig. 3.13(a), do not display any clear variations which immediately can be attributed to LDOS variations. The expected LDOS dependence of the excited state's decay rate is however not as simple as is the case for the ground state exciton. A schematic diagram of the energy levels of the quantum dot is shown in Fig. 3.13(c). As indicated in the

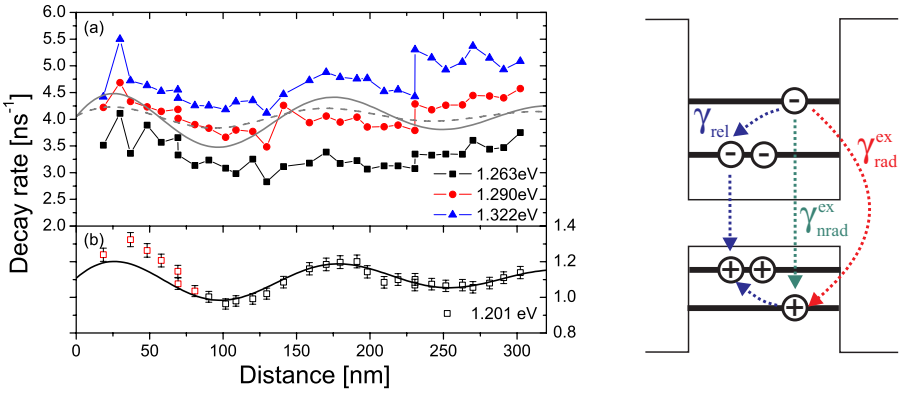

Fig. 3.13: **Left: (a)** The initial decay rates versus distance at 1.263 eV, 1.290 eV and 1.322 eV. **(b)** The fast decay rate from the ground state transitions. Acquired at 1.201 eV. **Right:** Schematic level diagram showing a quantum dot populated by three excitons and the decay channels for the excited state.

figure, the excited state can decay through three distinct channels: the radiative channel (γ^{ex}_{rad}), the non-radiative channel (γ^{ex}_{nrad}), and a relaxation channel down to the bi-exciton level (γ_{rel}). The total decay rate is thus given as a sum of the three rates, $\gamma^{ex} = \gamma^{ex}_{rad} + \gamma^{ex}_{nrad} + \gamma_{rel}$. While the non-radiative contribution is independent of the LDOS, both the radiative decay rate and the relaxation rate will depend on the LDOS as will be explained below.

Due to mixing of the heavy and light hole bands for the excited states [26, 30] the nature of the transition dipole moment is more complex than in the case for the ground state exciton. The emission pattern of the excited state depends on the exact mixture of light and heavy holes forming the exciton. It is, however, far from a trivial task to determine the exact composition, so here we will assume that the transition dipole of the excited state is heavy-hole like, and the radiative decay rate γ^{ex}_{rad} will correspondingly be modelled to follow the variations in the parallelly projected LDOS. The relaxation channel γ_{rel} will only open after a decay of the bi-exciton. When the channel is open, this intra-dot relaxation is expected to be very fast compared to the decay of the bi-exciton. In this case the relaxation rate γ_{rel} will be dominated by the decay rate of the bi-exciton, which is dominated by radiative decay and thus depends on the LDOS.

In Fig. 3.13(a) two theoretical calculations for the decay rate of the excited state

at 1.290 eV are shown. The calculations are based on the following assumptions: i) the relaxation rate is given by the decay rate of the bi-exciton, which is assumed to be 1.5 times faster than the ground state exciton [31], ii) the corresponding ground state is ~ 90 meV below the exited state (1.201 eV), and iii) the transition dipole of the excited state is parallel to the interface. The solid line is calculated for a negligible $\gamma_{\mathrm{nrad}}^{\mathrm{ex}}$, while the dashed line is calculated using the ratio $\gamma_{\mathrm{nrad}}^{\mathrm{ex}}/\gamma_{\mathrm{rad}}^{\mathrm{ex}} = 10$. However, the quality of the present data does not allow us to determine whether the excited state is dominated by non-radiative or radiative decay.

Exciton ground states

The fast decay rates of the ground state, Γ_{f}, oscillate in accordance with the projected LDOS as shown in Fig. 3.13(b). An analysis similar to the one described in Sec. 3.3 is used to obtain the radiative and non-radiative decay rates for the six different transition energies. Based on the findings from the previous section the data obtained for distances $z < 75$ nm are excluded in the data analysis. The radiative and non-radiative rates are shown in Fig 3.14(a) together with the rates obtained in the weak excitation regime. For increasing energy the non-radiative decay rate is found to increase, while the radiative decay rate is found to decrease. This is identical with the behaviour observed in the weak excitation regime and results in a decrease of the quantum efficiency with energy.

The non-radiative decay rates obtained in the strong excitation regime are substantially faster than in the weak excitation regime. We suggest that this is due to scattering of the quantum dot excitons on, e.g., excess excitons captured in the quantum dot, carriers trapped at defect centres in the GaAs or at the quantum dot's surface. Quite remarkably, the radiative decay rate is also affected by the excitation density. A reduction in the oscillator strength of $\sim 20\%$ is found by comparing the obtained values, shown in Fig 3.14(b), to the radiative decay rates obtained under weak excitation. A possible cause could be a loss of overlap between the electron and hole wavefunctions caused by perturbations of the wavefunctions by excess carriers in the quantum dot. Introducing excess carriers or even an extra exciton will affect the wavefunctions of the ground state exciton already present, this could maybe lead to a reduction in the oscillator strength of $\sim 20\%$.

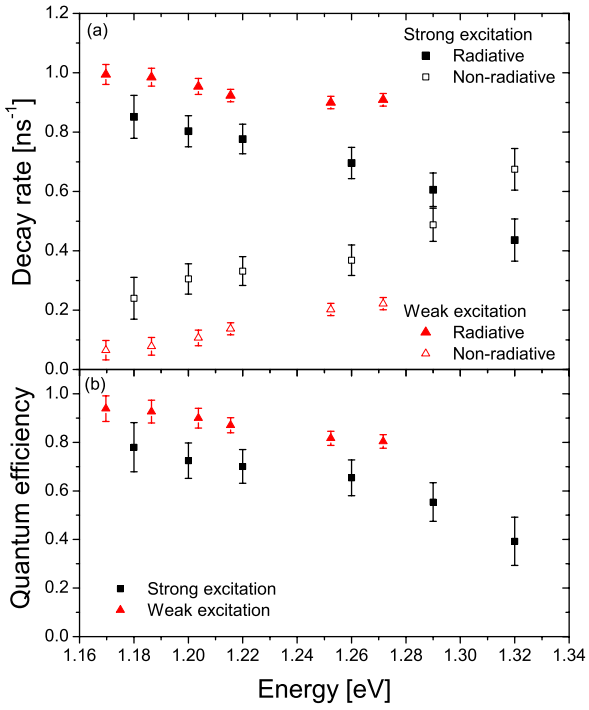

Fig. 3.14: **(a)** Radiative (filled symbols) and non-radiative (open symbols) decay rates obtained in the strong excitation regime (black squares) compared to those obtained under weak excitation (red triangles). **(b)** The quantum efficiency obtained under strong excitation (black squares) is significantly lower than under weak excitation (red triangles).

3.6 Experiments on colloidal CdSe quantum dots

Another type of quantum dots are nanocrystalline semiconductor colloids, often referred to as colloidal quantum dots or nanocrystals. Typical materials used for colloidal quantum dots are: CdSe, CdS, CdTe, PbSe. The quantum dots can be fabricated using wet-chemical synthesis, and they are commercially available in solutions with high monodispersity resulting in well-defined emission energies with a full width at half maximum of $\sim 5\%$ [32]. Fabrication by wet-chemical synthesis results in the colloids being covered by molecular ligands. The quantum dots consist thus in general of an inorganic core, e.g., CdSe, encapsulated by a shell

of organic molecular ligands. The ligands can function as molecular bounds to, e.g., binding sites in biological systems and the colloidal quantum dots can thus be used for biological labelling [33]. The fluorescence of the colloidal quantum dots are however strongly influenced by the ligands as charge carriers in some cases will be transferred to the ligands whereby the luminescence is quenched [34]. To passivate the surface and thus avoid this charge transfer, the colloids can be coated by an inorganic shell of a material with a higher band gap. The colloidal quantum dots studied in this section are CdSe overcoated by a few monolayers of ZnS to passivate the surface states.

In this section we present time-resolved measurement of CdSe/ZnS quantum dot ensembles positioned at various distances to an Ag-SiO_2 interface. As discussed previously, measurements for a single CdSe/ZnS quantum dot near an interface have been reported in Ref. [18]. In contrast to that work, our purpose is to obtain the ensemble-averaged properties for several emission energies and to perform the measurements for several positions. The latter in order to validate the theoretical interpretation.

3.6.1 Properties of CdSe quantum dots

The colloidal CdSe quantum dots differ from MBE-grown InAs quantum dots on two points which will increase the complexity of the time-resolved measurements: i) the individual quantum dots are randomly oriented and ii) the spontaneous emission from single quantum dots exhibits a multi-exponential decay. The random orientation is a direct consequence of the quantum dots being in suspension. The intrinsic multi-exponential decay of single quantum dot is not fully understood. It is, however, a commonly accepted hypothesis that it is caused by fluctuations in the non-radiative decay rate of the single quantum dot caused by charge carriers trapped at the surface [18, 35, 36].

To extract physically meaningful parameters from a multi-exponential decay is in itself a non-trivial task. Moreover, by placing an ensemble of randomly oriented quantum dots in an environment with an anisotropic LDOS, the complexity of the decay curve is increased as the radiative decay rate of the individual quantum dot will depend on its orientation. The properties of an ensemble of CdSe placed close to an interface differ thus strongly from the properties of the InAs quantum dots studied in the previous sections. Where the spontaneous emission from an energetically identical ensemble of InAs quantum dots displays a well understood bi-exponential decay, an ensemble of CdSe will display a complex decay being a

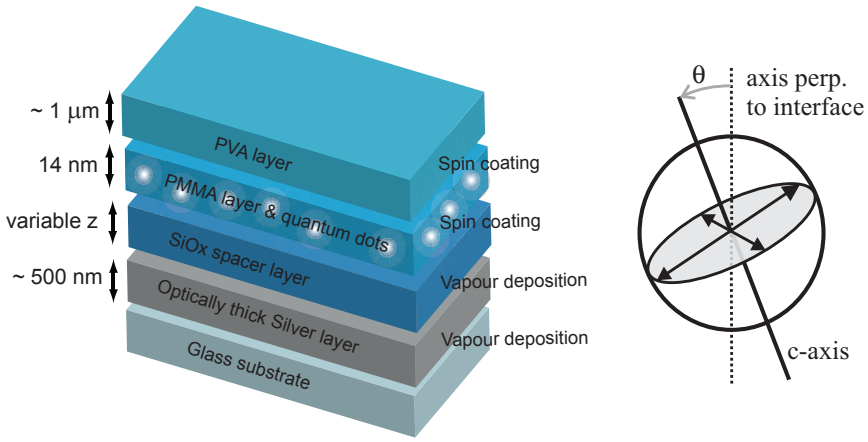

Fig. 3.15: **Left:** A schematic drawing of the sample. Courtesy of M. Leistikow. **Right:** The 2D dipole of the CdSe quantum dots. The dipole plane is perpendicular to the crystal axis c. The angle θ between an axis perpendicular to the interface and the c-axis describes the quantum dot orientation.

sum of multi-exponential decays from the individual quantum dots.

To interpret the complex multi-exponential decay, we adopt the approach of modelling the decay using a log-normal distribution of decay rates:

$$N(t) = A_0 \int_0^\infty \sigma(\Gamma) e^{-\Gamma t}\, d\Gamma, \qquad \sigma(\Gamma) = C \exp\left[-\left(\frac{\ln\Gamma - \ln\Gamma_{\mathrm{mf}}}{w} \right)^2 \right]. \tag{3.4}$$

Here Γ_{mf} is the most frequent decay rate, corresponding to the maximum of $\sigma(\Gamma)$. w is a dimensionless width parameter from which the $1/e$ width can be determined as $\Delta\Gamma = 2\Gamma_{\mathrm{mf}} \sinh w$. The normalization constant C ensures that $\int_0^\infty \sigma(\Gamma)\, d\Gamma = 1$.

3.6.2 Sample preparation

The samples, depicted in Fig. 3.15(a), consist of a glass substrate on which is evaporated an optically thick silver layer (500 nm) followed by the evaporation of a layer of SiO_2. The thickness of the SiO_2 layer is varied from sample to sample to obtain different distances between the quantum dots and the Ag-SiO_x interface. On top of the SiO_2 layer a suspension of CdSe/ZnS quantum dots[4] and polymethyl methacrylate (PMMA) dissolved in toluene is spin coated. This results in a thin PMMA layer (14 ± 5 nm) in which the randomly oriented quantum

[4] The quantum dots (ED-C11-TOL-0600) are supplied by Evident Technologies.

dots are embedded. Finally a 1 µm thick layer of polyvinyl alcohol (PVA) is spin coated on top of the quantum-dot-PMMA layer in order to shift the PMMA-air interface further away from the quantum dots. The SiO_2 alloy and the PVA are the choice for the layers surrounding the quantum dots as their refractive indices resemble the one of the PMMA, i.e., the three layers effectively appear as a single homogeneous optical layer. The refractive indices are: $n_{SiO_2} = 1.55 \pm 0.01$ (measured by ellipsometry), $n_{PMMA} = 1.49 \pm 0.01$ and $n_{PVA} = 1.50 \pm 0.01$. At the quantum dot emission energy the refractive index of silver is $n_{Ag} = 0.266 + i\,4.00$ [37].

Due to the random orientation of the quantum dots, it is necessary to consider the nature of the transition dipole. The hexagonal crystal structure of CdSe reduces the degeneracy of the valence band whereby the lowest excitonic energy level is only two-fold degenerate. The projection of the angular momentum of these two states along the c-axis of the crystal can acquire the values $\pm\hbar$ [38]. This results in the transition dipole to be 2D degenerate and located in a plane perpendicular to the c-axis [38, 39] as observed in single-quantum dot studies performed at both cryogenic and room temperature [18, 40, 41]. Since the samples have rotational symmetry about an axis perpendicular to the interface, the orientation of the dipole planes can be describe solely by the angle θ as sketched in Fig. 3.15(b).

3.6.3 Experimental setup

The quantum dots are optically pumped at 2.33 eV using 75 ps long pulses at a repetition rate of 8.4 MHz created by a Cougar laser (Time Bandwidth). The spectral selection is obtained using a Carl Leiss prism monochromator adjusted to a resolution of 6 nm. The spontaneous emission directed onto a microchannel plate photomultiplier tube (MCP-PMT, Hamamatsu R3809U) used for the single photon detection. The collecting optics of the setup has an effective numerical aperture of 0.09. To avoid photo-oxidation[5] the samples are placed in a nitrogen-purged chamber during measurements.

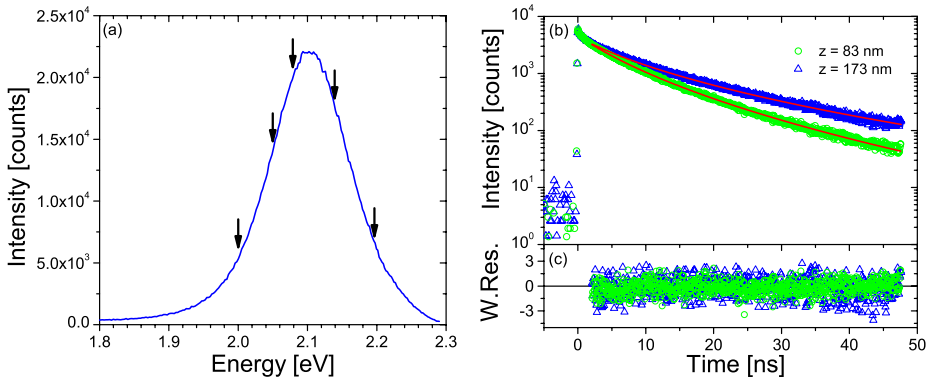

Fig. 3.16: **(a)** Spectra of CdSe/ZnS quantum dots positioned 80 nm from the Ag-SiO_2 interface. The five emission energies probed are indicated by the arrows. **(b)** Decay of the spontaneous emission from CdSe quantum dots for 80 nm (green squares) and 173 nm (blue triangles). **(c)** The weighted residuals from the fit of a log-normal model to the data (solid red lines in (b)).

3.6.4 *Time-resolved measurements of spontaneous emission from CdSe/ZnS quantum dots*

We have acquired time-resolved measurements on six different samples for which the distance z between the quantum dot layer and the Ag-SiO_2 interface is varied between 80 nm and 173 nm. At each distance the decay curves are acquired for five different emission energies as indicated in Fig. 3.16(a) where the emission spectrum from the CdSe ensemble ($z = 80$ nm) is shown. Two decay curves acquired at an emission energy of 2.082 eV are shown in Fig. 3.16(b) for the distances $z = 80$ nm (green squares) and $z = 173$ nm (blue triangles). As in the case of InAs quantum dots, a clear effect of the LDOS variations can be observed.

The solid red lines shown in Fig. 3.16(b) are fits of a log-normal model to the data, resulting in the randomly distributed residuals shown in Fig. 3.16(c). The χ^2_{R}-values for the two fits are 0.72 and 1.44 respectively. In Fig. 3.17(a) the most-frequent decay rates Γ_{mf} obtained from log-normal fits to the data acquired at 2.082 eV are shown. Together with the data the most-frequent decay rates calcu-

[5] Photo-oxidation is caused by oxygen, which penetrates the ZnS shell and reacts with the CdSe core forming of an oxide layer. The process is photo induced and results in quenching of the luminescence and a blue-shift of the emission spectrum as the size of the core is reduced [42].

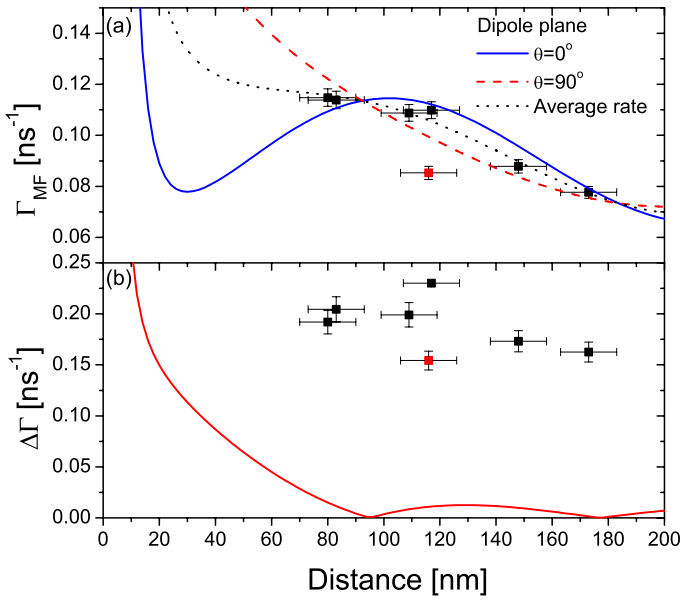

Fig. 3.17: **(a)** The most-frequent decay rate obtained at 2.08 eV for the various distances. The decay rate calculated for a projection of the normalized LDOS onto a dipole plane parallel, $\theta = 0^o$ (solid blue line) and perpendicular, $\theta = 90^o$ (dashed red line). The dotted, black line is the average of the two rates. **(b)** The $1/e$ width corresponding to the Γ_{mf} shown in (a). The solid red line is the difference between the rates for $\theta = 0^o$ and $\theta = 90^o$.

lated for the LDOS projected onto *dipole plane* which is either parallel ($\theta = 0^0$) to the interface or perpendicular ($\theta = 90^0$) to the interface are shown. Let us recapitulate the ensemble properties: The spontaneous emission from each quantum dot displays a multi-exponential decay. The spontaneous emission from the ensemble of randomly oriented quantum dots is thus a sum of multi-exponential decays. To obtain quantitative information, this sum of multi-exponentials is fitted by a single log-normal distribution of decay rates. As the most-frequent decay rate is an ensemble property, it is not expected to follow the most-frequent decay rates calculated for neither a dipole plane parallel nor perpendicular to the interface. Instead it is expected to be given by a weighted average of the two, where the

weights depend on the dipole radiation pattern. Here we neglect the specific dependence of the weights on the radiation patterns, and model the most-frequent decay rate for the ensemble by the average of the decay rates obtained for the two orientations of the dipole planes. This rate is shown by the dotted black line in Fig. 3.17(a) and is indeed in good agreement with the measured most-frequent decay rates.

The $1/e$ widths obtained from the log-normal fits are shown in Fig. 3.17(b). In correspondence with the interpretation described above, the difference in the most-frequent decay rates obtained for different orientations of the dipole planes is expected to affect the width of the distribution. This difference is shown by the solid red line in Fig. 3.17(b). The additional radiative broadening of the distributions caused by the orientation of the dipole planes is small compared to the intrinsic non-radiative broadening. It is thus not possible to determine whether this additional broadening is present or not.

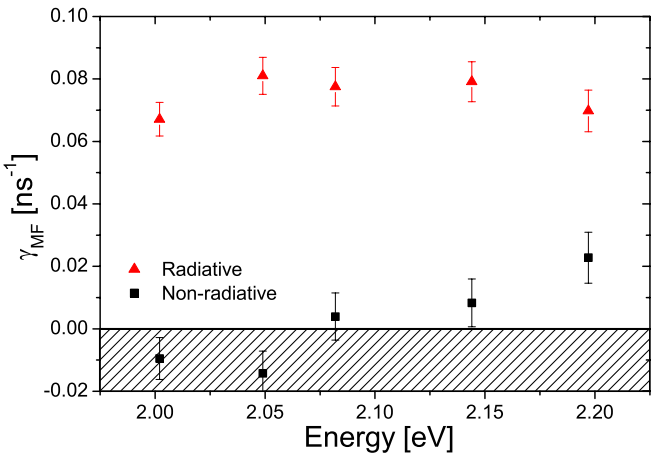

Fig. 3.18: The radiative (red triangles) and non-radiative decay rate obtained from the most-frequent decay rates. The shaded area indicates unphysical (negative) rates.

The radiative and non-radiative decay rates obtained from the measured most-frequent decay rates (using Eq. (3.2)) are shown in Fig. 3.18(a) as a function of energy. The radiative decay rate varies between $0.067\,\mathrm{ns}^{-1}$ and $0.081\,\mathrm{ns}^{-1}$ for en-

ergies between 2.00 and 2.20 eV, showing no clear dependence on emission energy. The non-radiative decay rate shows an overall increase from a value of $-0.010\,\mathrm{ns}^{-1}$ at 2.00 eV to $0.023\,\mathrm{ns}^{-1}$ at 2.20 eV. The unphysical negative decay rates could indicate a failure of the model which most likely could be due to the log-normal distribution failing to model the ensemble decay correct. However, the average values for the radiative and non-radiative decay rates correspond to a radiative life time of $\sim 13.3\,\mathrm{ns}$ and a high quantum efficiency of 0.97. This is in good agreement with measurements on single quantum dots showing mono-exponential decay [18]. It should be noted here that by analyzing the most-frequent decay rate, we are effectively selecting the quantum dots with high quantum efficiency. This is probably the reason for the good correspondence to the results obtained on mono-exponentially decaying single quantum dots.

3.7 Conclusion

In summary, we have measured the radiative and non-radiative decay rates of InAs quantum dots by employing the modified LDOS near a dielectric interface. The oscillator strength and quantum efficiency of the quantum dots and their dependence on the emission energy were accurately determined in two different excitation regimes. The radiative decay rate decreases with increasing energy corresponding to a reduction of the oscillator strength. In contrast, the non-radiative recombination rate increases with increasing energy. Consequently, quantum dots emitting on the low-energy side of the inhomogenously broadened ground state transition attain the highest oscillator strength and the highest quantum efficiency. Thus the low-energy quantum dots are most suitable as nanophotonic light sources due to their better optical properties. Under strong excitation the radiative decay rates are found to be slower, while the non-radiative decay rates are faster. This corresponds to a reduction of both the quantum efficiency and the oscillator strength of the quantum dot under strong excitation.

The effect of LDOS variations was also studied for the case of colloidal CdSe quantum dots. Due to the intrinsic multi-exponential decay dynamics and random orientation of the individual quantum dots the decay of spontaneous emission from an ensemble possess a high complexity. Despite this, we are able to obtain a good agreement between the measured and calculated most-frequent decay rates. This is obtained by calculating the average of the LDOS projected onto dipole planes either parallel or perpendicular to the interface.

References to Chapter 3

[1] J. P. Reithmaier, G. Sęk, A. Löffler, C. Hofmann, S. Kuhn, S. Reitzenstein, L. V. Keldysh, V. D. Kulakovskii, T. L. Reinecke, and A. Forchel, *Strong coupling in a single quantum dot-semiconductor microcavity system*, Nature 432, 197 (2004).

[2] T. Yoshie, A. Scherer, J. Hendrickson, G. Khitrova, H. M. Gibbs, G. Rupper, C. Ell, O. B. Shchekin, and D. G. Deppe, *Vacuum Rabi splitting with a single quantum dot in a photonic crystal nanocavity*, Nature 432, 200 (2004).

[3] E. Peter, P. Senellart, D. Martrou, A. Lemaître, J. Hours, J. M. Gérard, and J. Bloch, *Exciton-Photon Strong-Coupling Regime for a Single Quantum Dot Embedded in a Microcavity*, Phys. Rev. Lett. 95, 067401 (2005).

[4] P. Lodahl, A. F. van Driel, I. S. Nikolaev, A. Irman, K. Overgaag, D. Vanmaekelbergh, and W. L. Vos, *Controlling the dynamics of spontaneous emission from quantum dots by photonic crystals*, Nature 430, 654 (2004).

[5] A. Kress, F. Hofbauer, N. Reinelt, M. Kaniber, H. J. Krenner, R. Meyer, G. Böhm, and J. J. Finley, *Manipulation of the spontaneous emission dynamics of quantum dots in two-dimensional photonic crystals*, Phys. Rev. B 71, 241304 (2005).

[6] D. Englund, D. Fattal, E. Waks, G. Solomon, B. Zhang, T. Nakaoka, Y. Arakawa, Y. Yamamoto, and J. Vučković, *Controlling the Spontaneous Emission Rate of Single Quantum Dots in a Two-Dimensional Photonic Crystal*, Phys. Rev. Lett. 95, 013904 (2005).

[7] R. Sprik, B. A. van Tiggelen, and A. Lagendijk, *Optical emission in periodic dielectrics*, EPL (Europhysics Letters) 35, 265 (1996).

[8] L. C. Andreani, G. Panzarini, and J. M. Gérard, *Strong-coupling regime for quantum boxes in pillar microcavities: Theory*, Phys. Rev. B 60, 13276 (1999).

[9] J. Hours, P. Senellart, E. Peter, A. Cavanna, and J. Bloch, *Exciton radiative lifetime controlled by the lateral confinement energy in a single quantum dot*, Phys. Rev. B 71, 161306 (2005).

[10] J. J. Finley, M. Sabathil, P. Vogl, G. Abstreiter, R. Oulton, A. I. Tartakovskii, D. J. Mowbray, M. S. Skolnick, S. L. Liew, A. G. Cullis, and M. Hopkinson,

Quantum-confined Stark shifts of charged exciton complexes in quantum dots, Phys. Rev. B 70, 201308 (2004).

[11] A. F. Jarjour, R. A. Oliver, A. Tahraoui, M. J. Kappers, C. J. Humphreys, and R. A. Taylor, *Control of the Oscillator Strength of the Exciton in a Single InGaN-GaN Quantum Dot*, Phys. Rev. Lett. 99, 197403 (2007).

[12] K. H. Drexhage, *Influence of a Dielectric Interface on Fluorescence Decay Time*, J. Lumin. 1-2, 693 (1970).

[13] R. R. Chance, A. H. Miller, A. Prock, and R. Silbey, *Fluorescence and Energy-Transfer Near Interfaces - Complete and Quantitative Description of Eu+3-Mirror Systems*, J. Chem. Phys. 63, 1589 (1975).

[14] D. Birkedal, J. Bloch, J. Shah, L. N. Pfeiffer, and K. West, *Femtosecond dynamics and absorbance of self-organized InAs quantum dots emitting near 1.3 mu m at room temperature*, App. Phys. Lett. 77, 2201 (2000).

[15] R. J. Warburton, C. S. Dürr, K. Karrai, J. P. Kotthaus, G. Medeiros-Ribeiro, and P. M. Petroff, *Charged Excitons in Self-Assembled Semiconductor Quantum Dots*, Phys. Rev. Lett. 79, 5282 (1997).

[16] K. L. Silverman, R. P. Mirin, S. T. Cundiff, and A. G. Norman, *Direct measurement of polarization resolved transition dipole moment in InGaAs/GaAs quantum dots*, App. Phys. Lett. 82, 4552 (2003).

[17] R. J. Walters, J. Kalkman, A. Polman, H. A. Atwater, and M. J. A. de Dood, *Photoluminescence quantum efficiency of dense silicon nanocrystal ensembles in SiO2*, Phys. Rev. B 73, 132302 (2006).

[18] X. Brokmann, L. Coolen, M. Dahan, and J. P. Hermier, *Measurement of the Radiative and Nonradiative Decay Rates of Single CdSe Nanocrystals through a Controlled Modification of their Spontaneous Emission*, Phys. Rev. Lett. 93, 107403 (2004).

[19] R. R. Chance, A. Prock, and R. Silbey, *Molecular fluorescence and energy transfer near interfaces*, Adv. Chem. Phys. 37, 1 (1978).

[20] L. Novotny and B. Hecht, *Principles of Nano-Optics*, Cambridge University Press, New York (2006).

[21] Y. Mori and N. Watanabe, *A new etching solution system: H3PO4-H2O2-H2O for GaAs and its kinetics*, J. Electrochem. Soc. 125, 1510 (1978).

[22] M. R. Brozel and G. E. Stillman (eds.), *Properties of Gallium Arsenide*, chapter 9.6, INSPEC, The Institution of Electrical Engineers, London, 3rd edition (1996).

[23] R. Heitz, M. Veit, N. N. Ledentsov, A. Hoffmann, D. Bimberg, V. M. Ustinov, P. S. Kop'ev, and Z. I. Alferov, *Energy relaxation by multiphonon processes in InAs/GaAs quantum dots*, Phys. Rev. B 56, 10435 (1997).

[24] I. Favero, G. Cassabois, C. Voisin, C. Delalande, P. Roussignol, R. Ferreira, C. Couteau, J. P. Poizat, and J. M. Gérard, *Fast exciton spin relaxation in single quantum dots*, Phys. Rev. B 71, 233304 (2005).

[25] P. A. Dalgarno, J. M. Smith, B. D. Gerardot, A. O. Govorov, K. Karrai, P. M. Petroff, and R. J. Warburton, *Dark exciton decay dynamics of a semiconductor quantum dot*, Phys. Stat. Sol. (a) 202, 2591 (2005).

[26] S. Cortez, O. Krebs, P. Voisin, and J. M. Gérard, *Polarization of the interband optical dipole in InAs/GaAs self-organized quantum dots*, Phys. Rev. B 63, 233306 (2001).

[27] C. F. Wang, A. Badolato, I. Wilson-Rae, P. M. Petroff, E. Hu, J. Urayama, and A. Imamoğlu, *Optical properties of single InAs quantum dots in close proximity to surfaces*, App. Phys. Lett. 85, 3423 (2004).

[28] K. J. Ahn and A. Knorr, *Radiative lifetime of quantum confined excitons near interfaces*, Phys. Rev. B 68, 161307 (2003).

[29] A. E. Siegman, *Lasers*, Oxford University Press, Oxford (1986).

[30] G. A. Narvaez, G. Bester, and A. Zunger, *Dependence of the electronic structure of self-assembled (In,Ga)As/GaAs quantum dots on height and composition*, J. Appl. Phys. 98, 043708 (2005).

[31] C. Santori, G. S. Solomon, M. Pelton, and Y. Yamamoto, *Time-resolved spectroscopy of multiexcitonic decay in an InAs quantum dot*, Phys. Rev. B 65, 073310 (2002).

[32] C. B. Murray, D. J. Norris, and M. G. Bawendi, *Synthesis and characterization of nearly monodisperse CdE (E = sulfur, selenium, tellurium) semiconductor nanocrystallites*, J. Am. Chem. Soc. 115, 8706 (1993).

[33] W. C. W. Chan and S. Nie, *Quantum Dot Bioconjugates for Ultrasensitive Nonisotopic Detection*, Science 281, 2016 (1998).

[34] O. Schmelz, A. Mews, T. Basche, A. Herrmann, and K. Mullen, *Supramolecular Complexes from CdSe Nanocrystals and Organic Fluorophors*, Langmuir 17, 2861 (2001).

[35] B. Fisher, H.-J. Eisler, N. Stott, and M. Bawendi, *Emission Intensity Dependence and Single-Exponential Behavior In Single Colloidal Quantum Dot Fluorescence Lifetimes*, J. Phys. Chem. B 108, 143 (2004).

[36] G. Schlegel, J. Bohnenberger, I. Potapova, and A. Mews, *Fluorescence Decay Time of Single Semiconductor Nanocrystals*, Phys. Rev. Lett. 88, 137401 (2002).

[37] D. R. Lide, *CRC Handbook of Chemistry and Physics*, CRC Press, Boca Raton, Florida, 84th edition (2003).

[38] A. L. Efros, M. Rosen, M. Kuno, M. Nirmal, D. J. Norris, and M. Bawendi, *Band-edge exciton in quantum dots of semiconductors with a degenerate valence band: Dark and bright exciton states*, Phys. Rev. B 54, 4843 (1996).

[39] F. Koberling, U. Kolb, G. Philipp, I. Potapova, T. Basche, and A. Mews, *Fluorescence Anisotropy and Crystal Structure of Individual Semiconductor Nanocrystals*, J. of Phys. Chem. B 107, 7463 (2003).

[40] S. A. Empedocles, R. Neuhauser, and M. G. Bawendi, *Three-dimensional orientation measurements of symmetric single chromophores using polarization microscopy*, Nature 399, 126 (1999).

[41] I. Chung, K. T. Shimizu, and M. G. Bawendi, *Room temperature measurements of the 3D orientation of single CdSe quantum dots using polarization microscopy*, PNAS 100, 405 (2003).

[42] W. G. J. H. M. van Sark, P. L. T. M. Frederix, D. J. Van den Heuvel, H. C. Gerritsen, A. A. Bol, J. N. J. van Lingen, C. de MelloDonega, and A. Meijerink, *Photooxidation and Photobleaching of Single CdSe/ZnS Quantum Dots Probed by Room-Temperature Time-Resolved Spectroscopy*, J. Phys. Chem. B 105, 8281 (2001).

4. MEASURING THE OVERLAP OF THE ELECTRON AND HOLE WAVEFUNCTIONS

The transition matrix element of the ground state transition in an InAs quantum dot is evaluated in the effective mass approximation, whereby the measured oscillator strength can be related to the overlap of the electron and hole wavefunctions in the quantum dot. We investigate the energy dependence of the wavefunction overlap and find a reduction with increasing energy. The experimental findings are explained by theoretical calculations of the electron and hole wavefunctions. The different energy dependence of the radiative decay in InAs and CdSe/ZnS quantum dots is explained by comparing wavefunction calculations on the two different systems.

4.1 Introduction

The electronic properties of quantum dots and other confining structures are determined by the confined particles' wavefunctions. The wavefunctions are thus a very important key in obtaining fundamental understanding of the properties of quantum dots. Performing measurements which directly yields knowledge of the wavefunctions is a difficult task. However, having obtained the oscillator strength of the ground state transition, we have acquired knowledge which allows us to obtain a fundamental property of the electron and hole wavefunctions, namely, the overlap of the wavefunctions. The measured energy dependence of the oscillator strength is therefore able to determine the energy (size) dependence of the wavefunctions overlap.

Different approaches to modelling the size dependence of the wavefunction overlap in self-assembled quantum dots leads to different conclusions: while $\mathbf{k} \cdot \mathbf{p}$ theory predicts an increase in the overlap for decreasing quantum dot size [1], the atomistic pseudo-potential approach predicts the opposite trend [2]. Different reports of the measured decay rates' dependence on the energy (size) also result in a unclear picture: both an decrease [3], a constant [4], and an increase [5, 6] in

the decay rate with increasing energy are observed for InAs quantum dots. We suggest that these diverging observations partly are due to different non-radiative contributions. As we discussed in the previous chapter, the measured total decay rate experience an increase with energy while the radiative decay rate decreases with energy.

In order to obtain the correct oscillator strength, and thus the wavefunction overlap, a separation of the non-radiative and radiative decay rates must be performed. Using the carefully derived radiative decay rates from the previous chapter, we are able to experimentally determined the wavefunction overlap without invoking any unjustified omission of the non-radiative decay rates.

4.2 Evaluation of the transition matrix element

To establish the relation between the oscillator strength and the wavefunction overlap, we must evaluate the transition matrix element for InAs quantum dots. Using the $\mathbf{p}\cdot\mathbf{A}$ form of the interaction Hamiltonian derived in Sec. 2.1.1, the radiative decay rate can be expressed as (Eq. (2.12))

$$\gamma_{\mathrm{rad}} = \frac{ne^2}{(2\pi)^2 m_0^2 \epsilon_0 \hbar c_0^3}\omega \int_0^{2\pi} d\phi \int_0^{\pi} d\theta \sin\theta |\langle g|\mathbf{e}_{\mathbf{k}\lambda}\cdot\hat{\mathbf{p}}|e\rangle|^2. \tag{4.1}$$

where $\mathbf{e}_{\mathbf{k}\lambda}$ is the polarization vector of the electric field and $\hat{\mathbf{p}}$ is the momentum operator of the electron which must be evaluated for the transition from state $|e\rangle$ to state $|g\rangle$. In the calculation of the radiative decay rate of the quantum dot ground state exciton the state $|g\rangle$ is the crystal ground state (no excitons in the quantum dot) and $|e\rangle$ is the state with one exciton in the quantum dot (the quantum dot exciton ground state).

To evaluate the transition matrix element in Eq. (4.1) for a quantum dot transition two assumptions must be made: i) the Coulomb interaction between the electron and the hole can be neglected, and ii) the electron and hole wavefunctions of the quantum dot can be described in the effective mass approximation. In the strong confinement regime where the excitonic Bohr radius is smaller than the size of the quantum dot, the energy associated with the Coulomb interaction is much smaller than the quantization energy [7, Chap. 5]. Thus, the Coulomb interaction can be safely neglected and the exciton can be described by uncorrelated electron and hole wavefunctions. The use of the effective mass approximation for small structures as quantum dots has been examined and validated by *Burt et al.* [8]. Thus, the wavefunctions can be expressed in the effective mass approxima-

tion as products of a Bloch function[1] $u(\mathbf{r})$ and an envelope function $F(\mathbf{r})$. Having justified the two assumptions, the transition matrix element can be written as

$$\langle g|\mathbf{e}_{\mathbf{k}\lambda}\cdot\hat{\mathbf{p}}|e\rangle = \langle F_{\mathrm{h}}(\mathbf{r})u_{\mathrm{v}}(\mathbf{r})|\mathbf{e}_{\mathbf{k}\lambda}\cdot\hat{\mathbf{p}}|F_{\mathrm{e}}(\mathbf{r})u_{\mathrm{c}}(\mathbf{r})\rangle, \tag{4.2}$$

where $F_{\mathrm{e}}(\mathbf{r})$ ($F_{\mathrm{h}}(\mathbf{r})$) is the envelope function of the electron (hole) and $u_{\mathrm{c}}(\mathbf{r})$ ($u_{\mathrm{v}}(\mathbf{r})$) is the Bloch function of the conduction band electron (valence band hole). Recognizing the differential properties of the momentum operator, $\hat{\mathbf{p}} = -\mathrm{i}\hbar\nabla$, Eq. (4.2) can be rewritten using the product rule for differentiation

$$\begin{aligned}\langle g|\mathbf{e}_{\mathbf{k}\lambda}\cdot\hat{\mathbf{p}}|e\rangle \quad = \quad & \langle F_{\mathrm{h}}(\mathbf{r})u_{\mathrm{v}}(\mathbf{r})u_{\mathrm{c}}(\mathbf{r})|\mathbf{e}_{\mathbf{k}\lambda}\cdot\hat{\mathbf{p}}|F_{\mathrm{e}}(\mathbf{r})\rangle \quad + \\ & \langle F_{\mathrm{h}}(\mathbf{r})u_{\mathrm{v}}(\mathbf{r})F_{\mathrm{e}}(\mathbf{r})|\mathbf{e}_{\mathbf{k}\lambda}\cdot\hat{\mathbf{p}}|u_{\mathrm{c}}(\mathbf{r})\rangle. \end{aligned}\tag{4.3}$$

The integrals, denoted by the Dirac brackets, must be performed over the complete crystal volume V. Since the envelope functions are slowly varying over the unit cell while the Bloch functions are strongly varying over the unit cell, this integral can be split into a product of two integrals where one is taken over the volume of the unit cell while the other is taken over the crystal volume, c.f. [9, Chap. 9]:

$$\begin{aligned}\langle g|\mathbf{e}_{\mathbf{k}\lambda}\cdot\hat{\mathbf{p}}|e\rangle \quad \simeq \quad & \langle u_{\mathrm{v}}(\mathbf{r})|u_{\mathrm{c}}(\mathbf{r})\rangle\langle F_{\mathrm{h}}(\mathbf{r})|\mathbf{e}_{\mathbf{k}\lambda}\cdot\hat{\mathbf{p}}|F_{\mathrm{e}}(\mathbf{r})\rangle \quad + \\ & \langle F_{\mathrm{h}}(\mathbf{r})|F_{\mathrm{e}}(\mathbf{r})\rangle\langle u_{\mathrm{v}}(\mathbf{r})|\mathbf{e}_{\mathbf{k}\lambda}\cdot\hat{\mathbf{p}}|u_{\mathrm{c}}(\mathbf{r})\rangle. \end{aligned}\tag{4.4}$$

The expression can be simplified further since the valence and conduction band Bloch functions are orthogonal $\langle u_{\mathrm{v}}(\mathbf{r})|u_{\mathrm{c}}(\mathbf{r})\rangle = 0$. The evaluation of the the transition matrix element is thus reduced to an evaluation of the electron and hole wavefunctions' overlap $\langle F_{\mathrm{h}}(\mathbf{r})|F_{\mathrm{e}}(\mathbf{r})\rangle$ and an evaluation of the momentum matrix element $\langle u_{\mathrm{v}}(\mathbf{r})|\mathbf{e}_{\mathbf{k}\lambda}\cdot\hat{\mathbf{p}}|u_{\mathrm{c}}(\mathbf{r})\rangle$:

$$\langle g|\mathbf{e}_{\mathbf{k}\lambda}\cdot\hat{\mathbf{p}}|e\rangle \quad \simeq \quad \langle F_{\mathrm{h}}(\mathbf{r})|F_{\mathrm{e}}(\mathbf{r})\rangle\langle u_{\mathrm{v}}(\mathbf{r})|\mathbf{e}_{\mathbf{k}\lambda}\cdot\hat{\mathbf{p}}|u_{\mathrm{c}}(\mathbf{r})\rangle. \tag{4.5}$$

It is important to notice that the evaluation of the momentum matrix element only involves the Bloch functions and thus does not depend on the symmetry or the size of the quantum dot but only on the bulk semiconductor properties. The effect of the quantum dot size, shape and symmetry is accounted for by the wavefunctions $|F_{\mathrm{e}}\rangle$ and $|F_{\mathrm{h}}\rangle$. In the following the explicit $\mathbf{r}$ dependence of the Bloch and the envelope functions will be omitted to simplify the notation.

[1] In the weak confinement regime the excitonic wavefunction is more conveniently expressed in Wannier functions.

4.2.1 The momentum matrix element in strained InAs

In the case of self-assembled quantum dots, the strain of the InAs will lift the degeneracy of the light hole and heavy hole bands whereby the heavy hole states become the highest lying hole states. The evaluation of the momentum matrix element thus only includes transitions from the conduction band to the heavy hole valence band:

$$\langle u_{\mathrm{v}}|\mathbf{e}_{\mathbf{k}\lambda}\cdot\hat{\mathbf{p}}|u_{\mathrm{c}}\rangle = \langle u_{\mathrm{hh}}|\mathbf{e}_{\mathbf{k}\lambda}\cdot\hat{\mathbf{p}}|u_{\mathrm{c}}\rangle. \tag{4.6}$$

The valence band Bloch functions ($|u_{hh}\rangle$, $|u_{lh}\rangle$, $|u_{so}\rangle$) can be written as linear combinations of the basis functions ($|u_x\rangle$, $|u_y\rangle$, $|u_z\rangle$) which carry the same symmetry properties as the p-orbitals [10]. In particular if the electron's **k**-vector is directed along the z-axis, i.e., the growth axis which is normal to the quantum dot layer[2], the two spin degenerate combinations for the heavy hole spin up $|u_{hh}\rangle$ and spin down $|\bar{u}_{hh}\rangle$ are

$$|u_{hh}\rangle = -\frac{1}{\sqrt{2}}\big(|u_x\rangle + i|u_y\rangle\big) \qquad |\bar{u}_{hh}\rangle = \frac{1}{\sqrt{2}}\big(|\bar{u}_x\rangle - i|\bar{u}_y\rangle\big). \tag{4.7}$$

In the dipole approximation the only allowed transitions are those between an electron and a hole state of opposite spin, c.f., Sec. 2.2.4. Here we consider the case of spontaneous emission, i.e., the recombination of an electron with a given spin with a hole with the opposite spin. Hence, only one of the heavy-hole spin states is of relevance. By expressing $\mathbf{e}_{\mathbf{k}\lambda}$ and $\hat{\mathbf{p}}$ in Cartesian coordinates Eq. (4.6) can thus be written as

$$\langle u_{\mathrm{v}}|\mathbf{e}_{\mathbf{k}\lambda}\cdot\hat{\mathbf{p}}|u_{\mathrm{c}}\rangle = -\frac{1}{\sqrt{2}}\big(\langle u_x| - i\langle u_y|\big)\begin{bmatrix}\sin\theta\cos\phi\\ \sin\theta\sin\phi\\ \cos\theta\end{bmatrix}\cdot\begin{bmatrix}\hat{p_{\mathrm{x}}}\\ \hat{p_{\mathrm{y}}}\\ \hat{p_{\mathrm{z}}}\end{bmatrix}|u_{\mathrm{c}}\rangle. \tag{4.8}$$

The only non-zero elements of the inner product in Eq. (4.8) are those for which the momentum operator and the wavefunction have the same symmetry, i.e., $\langle u_i|\hat{p}_j|u_c\rangle \neq 0$ only if $i = j$. Using the definition of the Kane energy

$$E_p \equiv \frac{2}{m_0}|\langle u_i|\hat{p}_i|u_c\rangle^2|, \qquad i = \{x, y, z\} \tag{4.9}$$

the square of the momentum matrix element simplifies to

$$|\langle u_{\mathrm{v}}^*|\mathbf{e}_{\mathbf{k}\lambda}\cdot\hat{\mathbf{p}}|u_{\mathrm{c}}\rangle|^2 = \frac{m_0 E_p}{4}\sin^2\theta. \tag{4.10}$$

[2] In our case the growth axis corresponds to the crystal axis [001].

The evaluation of the momentum matrix element has thus been simplified to the evaluation of a basic trigonometric function.

4.2.2 Wavefunction overlap in InAs/GaAs quantum dots

The radiative decay rate can now be obtained by substituting Eq. (4.10) and Eq. (4.5) into Eq. (4.1):

$$\begin{aligned}\gamma_{\mathrm{rad}}(\omega) &= \frac{2\pi n e^2 E_p}{4(2\pi)^2 m_0 \epsilon_0 \hbar c_0^3}\,\omega |\langle F_{\mathrm{h}}^*(\omega)|F_{\mathrm{e}}(\omega)\rangle|^2 \int_0^\pi d\theta\, \sin^3\theta \\ &= \frac{n e^2 E_p}{6\pi m_0 \epsilon_0 \hbar c_0^3}\,\omega\, |\langle F_{\mathrm{h}}^*(\omega)|F_{\mathrm{e}}(\omega)\rangle|^2. \qquad (4.11)\end{aligned}$$

The radiative decay rate is thus found to depend linearly on the emission frequency ω and on the overlap of the electron and hole wavefunctions $|\langle F_{\mathrm{h}}(\omega)|F_{\mathrm{e}}(\omega)\rangle|^2$. Expressed in terms of the oscillator strength, Eq. (4.11) can be put on the more elegant form

$$f_{\mathrm{osc}}(\omega) = \frac{E_p}{\hbar\omega}|\langle F_{\mathrm{e}}(\omega)|F_{\mathrm{h}}(\omega)\rangle|^2. \qquad (4.12)$$

For InAs the Kane energy has a value of $E_p^{\mathrm{InAs}} = 22.2\,\mathrm{eV}$ [11].

4.3 Measurements of wavefunction overlap in InAs quantum dots

With the use of Eq. (4.12) the measured oscillator strengths (shown in Fig. 3.10) are thus capable of providing insight into the energy dependence of the overlap of the electron and hole wavefunctions. The energy dependence of the wavefunctions is due to the size dependence inherited by all quantum dot properties. Strictly speaking, it is in fact the size of the quantum dot which determines the wavefunction and thus the quantization energy related to the wavefunction. For large quantum dots the quantization energy is low and the wavefunction is very well confined to the quantum dot hardly penetrating into the barriers. On the contrary a small quantum dot has a large quantization energy and the wave function will penetrate deeper into the barriers, i.e., the effective barrier height will appear smaller. Clearly, the barrier height and the mass of the carriers will also influence the energy levels.

From the measured oscillator strength, presented in the previous chapter, we have calculated the overlap of the wavefunctions as shown in Fig. 4.1. The overlap decreases from about 0.75 at 1.17 eV to 0.63 at 1.27 eV. This reduction in the

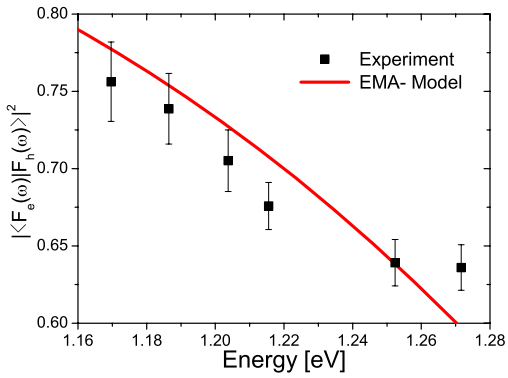

Fig. 4.1: Measured (squares) overlap of the envelope wavefunctions of electrons and holes obtained using Eq. (4.12). The calculated overlaps (red solid line) readily reproduce the measured energy dependence.

wavefunction overlap for increasing energy corresponds to an increasing mismatch between the electron and hole wavefunctions with decreasing quantum dot size. A different size dependence of the electron and hole wavefunctions can readily be explained by the difference in their respective effective masses: The low effective mass of the electron ($m^*_{e,\mathrm{InAs}} = 0.023m_0$, $m^*_{e,\mathrm{GaAs}} = 0.067m_0$) compared to the effective mass of the hole ($m^*_{hh,\mathrm{InAs}} = 0.40m_0$, $m^*_{hh,\mathrm{InAs}} = 0.50m_0$) results in more sensitive size dependence of the hole wavefunction than of the electron wavefunction. As the size of the quantum dot is decreased the electron wavefunction will only be weakly modified, while the extent of the hole wavefunction will follow the quantum dot size. This will cause a reduction of the overlap [12].

To examine whether this is a plausible explanation for the observed energy dependence of the oscillator strength, the deduced overlaps are compared to calculations of the wavefunction overlap. For this purpose, we implement a rotationally symmetric quantum dot model within the framework of the effective mass approximation. The finite element method[3] is used to calculate the electron and hole wavefunctions, from which both the emission energy and the wavefunction overlap are obtained. The wavefunctions calculated for a lens-shaped quantum dot with a radius of 7 nm and a height of 2.6 nm and 1.6 nm are shown in Fig. 4.2 and Fig. 4.3 respectively. The electron wavefunctions are shown to the left, while

[3] FemLab version 3.1i is used for the calculations.

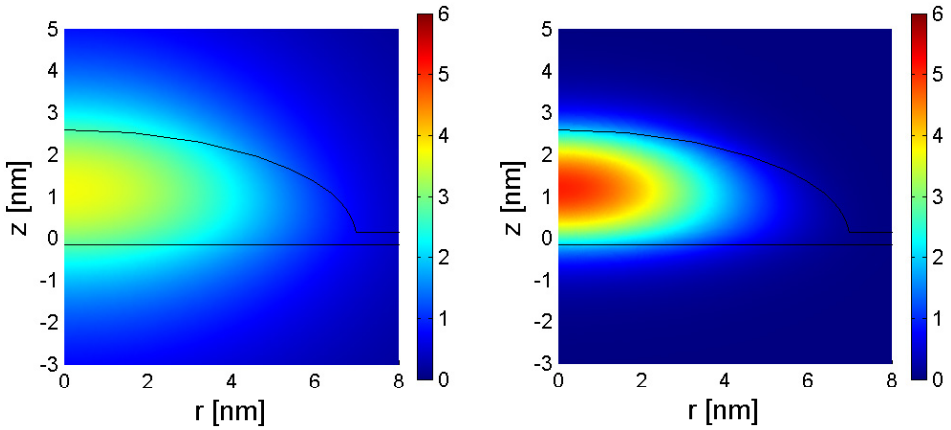

Fig. 4.2: The electron (left) and hole (right) wavefunctions calculated for a dot height of 2.6 nm resulting in an emission energy of 1.177 eV and an overlap of 0.79.

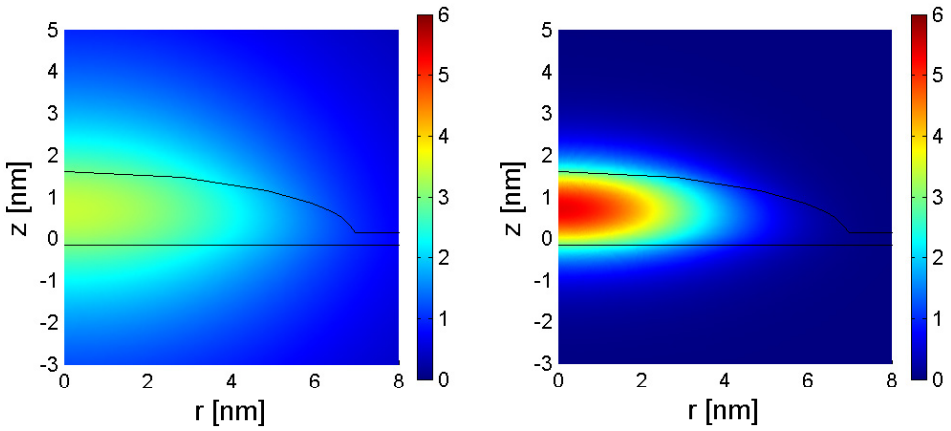

Fig. 4.3: The electron (left) and hole (right) wavefunctions calculated for a dot height of 1.6 nm resulting in an emission energy of 1.283 eV and an overlap of 0.61.

Tab. 4.1: Energies and effective masses used in the calculations.

	$In_{0.75}Ga_{0.25}As$-QD	GaAs-barrier
E_{gap}	0.647 eV	1.518 eV
m_e^*	$0.034\,m_0$	$0.067\,m_0$
m_h^*	$0.44\,m_0$	$0.50\,m_0$

the hole wavefunctions are shown to the right and the cross section of the quantum dot is indicated by the black lines. The colour scale, identical for all four plots, indicates the amplitude of the wavefunction. In general, the hole wavefunctions are found to be spatially localized within the quantum dot, while the electron wavefunctions penetrate into the barrier material. Reducing the quantum dot height from 2.6 to 1.6 nm (going from Fig. 4.2 to Fig. 4.3) the extent of the electron is hardly affected while the the hole wavefunction is found to be strongly bounded by the quantum dot height, causing a reduction in the spatial extend. This readily leads to a reduction in the overlap of the wavefunctions, as the quantum dot size is reduced. The curve in Fig. 4.1 displays the wavefunction overlap calculated for heights varying between 1.6 nm and 2.6 nm. Very good agreement with the experimental data is observed, and theory clearly confirms a pronounced reduction of the electron-hole wavefunction overlap as the size of the quantum dot is decreased. The following parameters are used in the calculations: a wetting layer thickness of 0.3 nm, 60% of the band edge discontinuity is in the conduction band, and the GaAs content in the quantum dots is taken to be 25%. The energies and effective masses used are tabulated in Tab. 4.1. The general validity has been tested by calculating for different sizes, shapes, and amount of GaAs content in the quantum dot, and they all show a decrease of overlap with increasing energy. The same behaviour is also obtained from more involved quantum dot models which also take into account the effect of strain [13].

This is, to the best of our knowledge, the first comparison between experimentally determined wavefunction overlap and theory. It is important to stress that this comparison is only worthwhile due to our knowledge of the *radiative* decay rates obtained in the previous chapter.

4.4 Wavefunctions in colloidal CdSe/ZnS quantum dots

Interestingly, the radiative rate of CdSe quantum dots has been reported to display the opposite dependence on energy as InAs quantum dots, i.e., an increase in the radiative rate with increasing energy [14]. However, this report is based on the assumption of a negligible non-radiative decay rate. To make an indisputable conclusion on the energy dependence it is necessary to quantify the non-radiative contributions for the various energies. Unfortunately, the data presented in Sec. 3.6 on CdSe/ZnS quantum dots did not allow for an accurate determination of the radiative decay rate, hence we can not experimentally determine the energy dependence of the radiative decay rate.

Under the assumption that it is the energy dependence of the *radiative* decay rate which is measured and reported in [14], the conclusion illustrates a striking difference in the optical properties of colloidal quantum dots compared to self-assembled quantum dots. The reported behaviour of colloidal CdSe could be explained by a wavefunction overlap which is independent of emission energy (size). In this case the radiative decay rate will increase linearly with energy according to Eq. (4.11). Comparing the colloidal CdSe/ZnS quantum dots with the self-assembled InAs quantum dots, it is immediately noted that the quantum dots are smaller, their confinement potential is larger, and the effective mass of the electron is heavy. These properties leads to wavefunctions which are strongly confined in the core of the quantum dots, i.e., the extent of the wavefunctions is strictly bounded by the size of the quantum dot core.

We have calculated the electron and hole wavefunctions for a spherical CdSe/ZnS quantum dot. The core radius is varied between 3.5 nm and 2.5 nm while the ZnS shell thickness is kept at 2.0 nm. These values correspond well with the actual sizes of chemically synthesized CdSe/ZnS quantum dots as specified by the supplier. The band gap and effective masses used for the calculations are tabulated in Tab. 4.2. The electron and hole wavefunctions obtained for core radii of 3.5 nm and 2.5 nm are shown in Fig. 4.4(a-b) and Fig. 4.4(c-d) respectively. The emission energies are calculated to be 1.938 eV and 2.117 eV. The obtained energies correspond remarkably well with those obtained in the measurements in Sec. 3.6. In contrast to the case of InAs quantum dots, both the electron and hole wavefunctions are strongly localized within the core of the quantum dot hardly extending into the ZnS shell. This difference is brought along by a reduction of the effective mass ratio m_h^*/m_e^* by a factor ~ 3 and an increase of the potential difference $E_{\text{gap}}^{\text{barrier}} - E_{\text{gap}}^{\text{QD}}$ by a factor of ~ 2 when comparing to InAs quantum dots. As the

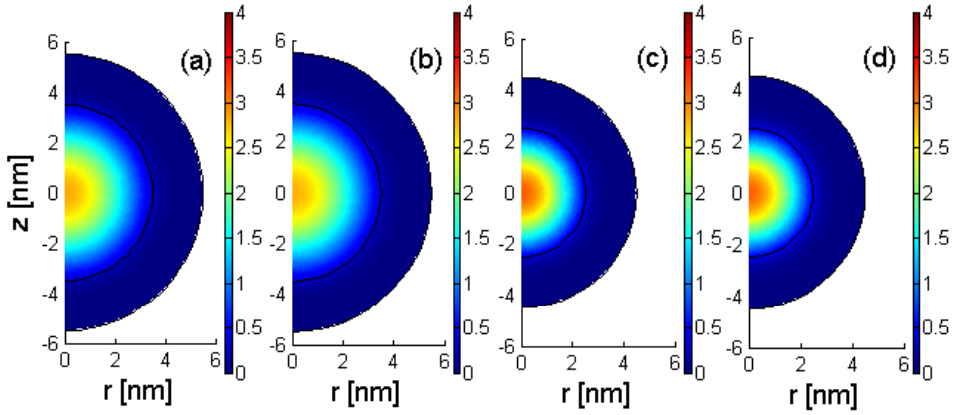

Fig. 4.4: The electron **(a)** and hole **(b)** wavefunctions calculated for a core radius of 3.5 nm resulting in an emission energy of 1.938 eV. The electron **(c)** and hole **(d)** wavefunctions calculated for a core radius of 2.5 nm resulting in an emission energy of 2.117 eV.

Tab. 4.2: Energies and effective masses used in the calculations.

	CdSe-QD	ZnS-barrier
E_{gap}	1.72 eV	3.54 eV
m_e^*	0.15 m_0	0.42 m_0
m_h^*	0.60 m_0	0.61 m_0

electron and hole wavefunctions dependence on the quantum dot size are similar, the overlap is independent of the quantum dot size, and the values obtained for the overlap deviate from unity by less than 10^{-4}. Judging from these calculations alone, it is plausible that the radiative decay rate increases linearly with increasing energy.

4.5 Conclusion

We have described how to evaluate the quantum dot transition matrix element in the effective mass approximation and hereby obtain the relation between the oscillator strength and the overlap of the electron and hole wavefunctions. The measurements presented in Chap. 3, thereby enables us to quantify the energy

dependence of the wavefunction overlap for InAs/GaAs quantum dots. It is important to stress that this is only possible due to our explicit knowledge of the *radiative* decay rates. The overlap is reduced from 0.75 at 1.17 eV to 0.63 at 1.27 eV. The experimental findings are supported by theoretical calculations and the reduction of the wavefunction overlap is determined to stem from a different sensitivity of the electron and hole wavefunctions to the quantum dot size. To the best of our knowledge, this the first comparison of experimentally determined wavefunction overlap and theory. The observation of improved wavefunction overlap for large quantum dots is important for optimization of the strong coupling in QED experiments.

The energy dependence of the wavefunction overlap in self-assembled InAs quantum dots is compared to the energy dependence calculated for colloidal CdSe/ZnS quantum dots. In the latter case the wavefunction overlap is found to be independent on size, which explains the observed [14] difference in the energy dependence of the radiative decay rate for the two different quantum dot types.

References to Chapter 4

[1] O. Stier, M. Grundmann, and D. Bimberg, *Electronic and optical properties of strained quantum dots modeled by 8-band k.p theory*, Phys. Rev. B 59, 5688 (1999).

[2] G. A. Narvaez, G. Bester, and A. Zunger, *Excitons, biexcitons, and trions in self-assembled (In,Ga)As/GaAs quantum dots: Recombination energies, polarization, and radiative lifetimes versus dot height*, Phys. Rev. B 72, 245318 (2005).

[3] T. F. Boggess, L. Zhang, D. G. Deppe, D. L. Huffaker, and C. Cao, *Spectral engineering of carrier dynamics in In(Ga)As self-assembled quantum dots*, App. Phys. Lett. 78, 276 (2001).

[4] H. Yu, S. Lycett, C. Roberts, and R. Murray, *Time resolved study of self-assembled InAs quantum dots*, App. Phys. Lett. 69, 4087 (1996).

[5] S. Malik, E. C. Le Ru, D. Childs, and R. Murray, *Time-resolved studies of annealed InAs/GaAs self-assembled quantum dots*, Phys. Rev. B 63, 155313 (2001).

[6] L. Y. Karachinsky, S. Pellegrini, G. S. Buller, A. S. Shkolnik, N. Y. Gordeev, V. P. Evtikhiev, and V. B. Novikov, *Time-resolved photoluminescence measurements of InAs self-assembled quantum dots grown on misorientated substrates*, App. Phys. Lett. 84, 7 (2004).

[7] D. Bimberg, M. grundmann, and N. N. Ledentsov, *Quantum Dot Heterostructures*, Wiley, Chichester (1999).

[8] M. G. Burt, *On the validity and range of applicability of the particel in a box model*, App. Phys. Lett. 65, 717 (1994).

[9] S. L. Chuang, *Physics of Optoelectronic Devices*, Wiley-Interscience, New York (1995).

[10] P. Y. Yu and M. Cardone, *Fundamentals of Semiconductors*, Springer, Berlin, 3rd edition (2001).

[11] P. Lawaetz, *Valence-Band Parameters in Cubic Semiconductors*, Phys. Rev. B 4, 3460 (1971).

[12] G. A. Narvaez, G. Bester, and A. Zunger, *Dependence of the electronic structure of self-assembled (In,Ga)As/GaAs quantum dots on height and composition*, J. Appl. Phys. 98, 043708 (2005).

[13] A. D. Andreev and E. P. O'Reilly, *Optical matrix element in InAs/GaAs quantum dots: Dependence on quantum dot parameters*, App. Phys. Lett. 87, 213106 (2005).

[14] A. F. van Driel, G. Allan, C. Delerue, P. Lodahl, W. L. Vos, and D. Vanmaekelbergh, *Frequency-Dependent Spontaneous Emission Rate from CdSe and CdTe Nanocrystals: Influence of Dark States*, Phys. Rev. Lett. 95, 236804 (2005).

5. DECAY DYNAMICS OF BRIGHT AND DARK EXCITONS

The decay dynamics of quantum dot ensembles is studied using time-resolved spectroscopy. Within a time span of $\sim 13\,ns$ *the decay is very well described by a bi-exponential model which arises from the fine structure of the exciton. The intrinsic spin-flip rate between bright and dark excitons can be determined, and we find ensemble averaged spin-flip rates in the range between* 2 *and* $50\,\mu s^{-1}$*. The spin-flip rate displays a clear dependence on excitation density, excitation energy, the presence of a nearby interface, and temperature.*

5.1 Introduction

Quantum dots are often considered as artificial atoms due to their atom-like property, i.e., their discrete spectrum of electronic states. The standard approach of studying the decay dynamics of *atoms* is in terms of single exponential decay. This approach has conveniently been adopted for the study of quantum dot decay dynamics. Real quantum dots are however far from being ideal two-level emitters causing the decay dynamics to reveal a much richer complexity. One of the reasons for the complex decay dynamics is the exciton fine structure which, as discussed in Sec. 2.2.4, leads to a bi-exponential decay. Obtaining knowledge of the decay dynamics of quantum dots is important to improve and expand their potential as nanophotonic light sources in quantum electrodynamics experiments and devices. This has most recently been exemplified by the suppression of dark exciton creation leading to the highest reported repetition rate of a quantum dot based single-photon emitter [1]. Knowledge of the decay dynamics cannot only facilitate improvement of devices, but is crucial to interpret experiments involving inhibition of the spontaneous emission as will be evident in Chapter 6.

We present here a detailed analysis of the time-resolved measurements acquired over time spans of 13 ns and 200 ns. The knowledge gained in Chapter 3 serves as a basis for the analysis, i.e., an omission of the non-radiative decay rate leads to an inconsistent picture. To identify the processes affecting the radiative and

non-radiative decay rates, we study the dynamics under different excitation conditions, temperatures and at different distances to the dielectric interface introduced previously. The time-resolved measurements are analysed by employing the model based on the fine structure of the quantum dot ground state derived in Sec. 2.2.4. This careful analysis allows us to determine the *intrinsic* spin-flip rate between the bright and dark exciton states.

The coherence properties and dynamics of the spin states have drawn much attention since the proposal of quantum bit gates based on the spin states of electrons in quantum dots [2]. Different time-resolved schemes, based on the spontaneous decay of polarisation, have been used to deduce the spin-flip rate of the individual carriers [3–6]. Using these schemes the *intrinsic* spin-flip rate can however only be deduced under strictly resonant excitation as reported in Ref. [6], only. The specific method applied in Ref. [6] is based on the presence of an additional carrier in the quantum dot which could affect the spin-flip rate, e.g., by an increased carrier-carrier scattering. Moreover, the measurements are acquired over a short time span $< 2.5\,\mathrm{ns}$ which only allows for a direct determination of rates higher than $\sim 0.2\,\mathrm{ns}^{-1}$.

The method presented here exploits the bi-exponential nature of the decay dynamics. The spin-flip rate can be determined from the ratio of photon counts in the fast and slow components. The lowest spin-flip rate which can be measured is thus not limited by the repetition rate of the excitation source. Furthermore, as no restrictions apply to the excitation energy (resonant / non-resonant) or to excitation intensity, we are able to study the *intrinsic* spin-flip rate as a function of both excitation energy and intensity. To reveal the bi-exponential decay the time-resolved measurements must be performed over long time spans. Recently, only a few groups have presented time-resolved measurements of spontaneous emission from single quantum dots performed over more than just a few ns [7–9]. However, the purpose of these studies have been to display control over the spin-flip rate by an applied gate voltage [7], to report the existence of a strikingly high bright-bright spin-flip rate in some individual InAs quantum dots [8], and to study the temperature dependence of spontaneous emission from CdSe/ZnS colloidal quantum dots [9].

In this chapter we present extensive studies of the decay dynamics and thus the spin-flip rate of an ensemble of quantum dots under various excitation densities and energies, various distances to an interface, and various temperatures. The spin-flip rates can be determined correctly only by recognizing the existence of the

non-radiative decay, and are thus based on our findings from Chapter 3.

5.2 Obtaining the spin-flip rate from the bright-dark model

In Sec. 2.2.4 the decay dynamics of the ground state exciton was discussed in a model including the exciton fine structure, i.e., the bright and dark exciton states. The outcome of the model is a bi-exponential decay of the luminescence from the bright state

$$N(t) = A_{\mathrm{f}} e^{-\gamma_{\mathrm{f}} t} + A_{\mathrm{s}} e^{-\gamma_{\mathrm{s}} t}, \tag{5.1}$$

where the fast and slow rates are defined by

$$\begin{aligned} \gamma_{\mathrm{f}} &= \gamma_{\mathrm{rad}} + \gamma_{\mathrm{nrad}}^{\mathrm{b}} + \gamma_{\mathrm{bd}} \\ \gamma_{\mathrm{s}} &= \gamma_{\mathrm{nrad}}^{\mathrm{d}} + \gamma_{\mathrm{db}}. \end{aligned} \tag{5.2}$$

and the corresponding fast and slow amplitudes are defined as

$$\begin{aligned} A_{\mathrm{f}} &= \eta \gamma_{\mathrm{rad}} M \left[\rho_{\mathrm{b}}(0) - \frac{\gamma_{\mathrm{db}}}{\gamma_{\mathrm{rad}} + \gamma_{\mathrm{nrad}}^{\mathrm{b}} - \gamma_{\mathrm{nrad}}^{\mathrm{d}}} \rho_{\mathrm{d}}(0) \right], \\ A_{\mathrm{s}} &= \eta \gamma_{\mathrm{rad}} M \frac{\gamma_{\mathrm{db}}}{\gamma_{\mathrm{rad}} + \gamma_{\mathrm{nrad}}^{\mathrm{b}} - \gamma_{\mathrm{nrad}}^{\mathrm{d}}} \rho_{\mathrm{d}}(0). \end{aligned} \tag{5.3}$$

This bi-exponential decay of the luminescence arises due to the spin-flip coupling between the bright and the dark states; while the initial population of the bright excitons will contribute directly to the spontaneous emission through radiative decay, the dark excitons must flip their spin before they can decay radiatively and thus contribute to the spontaneous emission. The model was derived under the assumption that the spin-flip rate γ_{db} was slow compared to the radiative decay rate. If the opposite was the case, the fast spin-flip rate would bring the two exciton populations into equilibrium and the spontaneous emission would decay mono-exponentially. It can thus be argued from the mere appearance of the bi-exponential decay that the spin-flip rate γ_{db} must be slow compared to the fastest rate causing de-population of the bright and dark excitons, i.e., the radiative decay rate of the bright excitons γ_{b}.

We would like to stress that had we neglected the the non-radiative decay and thus assumed a quantum efficiency of 100% the slow rate γ_{s} in Eq. (5.1) would be given alone by the spin-flip rate γ_{db}. However, as we have verified the presence of the non-radiative decay rate, we can conclude that the slow rate is given by the sum of the non-radiative decay rate and the spin-flip rate.

The spin-flip rate can be obtained by taking the ratio of the fast and slow amplitudes stated in Eq. (5.3) and rearranging the terms leading to

$$\gamma_{\mathrm{db}}\frac{\rho_{\mathrm{d}}(0)}{\rho_{\mathrm{b}}(0)} = (\gamma_{\mathrm{rad}} + \gamma_{\mathrm{nrad}}^{\mathrm{b}} - \gamma_{\mathrm{nrad}}^{\mathrm{d}})\frac{A_{\mathrm{s}}}{A_{\mathrm{f}} + A_{\mathrm{s}}} \simeq (\gamma_{\mathrm{f}} - \gamma_{\mathrm{s}})\frac{A_{\mathrm{s}}}{A_{\mathrm{f}} + A_{\mathrm{s}}}. \tag{5.4}$$

To express the spin-flip rate solely with parameters obtained from the bi-exponential model (A_{f}, A_{s}, γ_{f}, γ_{s}), the following approximation has been used $\gamma_{\mathrm{rad}} + \gamma_{\mathrm{nrad}}^{\mathrm{b}} - \gamma_{\mathrm{nrad}}^{\mathrm{d}} \simeq \gamma_{\mathrm{f}} - \gamma_{\mathrm{s}} = (\gamma_{\mathrm{rad}} + \gamma_{\mathrm{nrad}}^{\mathrm{b}} + \gamma_{\mathrm{bd}}) - (\gamma_{\mathrm{nrad}}^{\mathrm{d}} + \gamma_{\mathrm{db}})$. By carefully analysing the measurements, we are thus able to obtain knowledge of the spin-flip rate and the ratio of the initial populations.

It should be noted that to obtain quantitative knowledge from the amplitudes it is necessary to take into account that the histograms forming the decay curves are built over many consecutive excitation events. The ratio of the initial populations will be affected by the repetitive nature of the experiment, i.e., the population of the slowly decaying dark excitons will not be negligible at the arrival time of the next excitation pulse. In the weak excitation regime this effect can be accounted for solely by correcting the measured slow amplitude for emission events caused by earlier excitations. The correction is given by a geometric series whereby the corrected amplitude A_{s} can be expressed as

$$A_{\mathrm{s}} = \tilde{A}_{\mathrm{s}}\big(1 - \exp(-\gamma_{\mathrm{s}}T)\big), \tag{5.5}$$

where T is the excitation period and $\tilde{A}_{\mathrm{s}}$ refers to the measured amplitude. The slow amplitudes A_{s} and the total number of counts in the slow component N_{s} reported here will all be corrected according to Eq. (5.5).

5.2.1 Spin-flip processes in quantum dots

In bulk III-V semiconductors the valence band states possess a mixed spin character as the spin-orbit coupling mixes the degenerate heavy and light hole valence band states [10]. Any scattering from one state to another can thus result in a relaxation of the spin. This mechanism, known as the Elliot-Yafet mechanism, is dominant near the band edge in bulk semiconductors where the large density of states enhances the probability of scattering on phonons, other carriers, defects, etc. At room temperature this rapid spin-flip channel provided by the Elliot-Yafet mechanism results in spin-flip times as short as $\sim 110\,\mathrm{fs}$ for holes in bulk GaAs [11].

The removal of the degeneracy of the light and heavy hole bands and the discretisation of the energy levels in quantum dots are expected to drastically

reduce or even eliminate the efficiency of this spin-flip channel. Several other spin-flip mechanisms are known, but the exact mechanisms actually causing the spin flip of carriers and excitons in quantum dots are still being discussed [10]. The predominant point of views are that the spin-flip can be explained either by spin-orbit interaction combined with phonon scattering [4, 12, 13] or by the hyperfine interaction of the spin with the spins of the lattice nuclei [14].

Several studies [15–17] have focused on the spin flip between the two bright exciton states, i.e., the spin-flip of both the electron and the hole. In case of sequential spin flip the spin-flip rate between the two bright states will be given by the slowest of the two. In the model presented here we are only concerned with the spin flip between the bright and the dark states and vice-versa. This rate is on the contrary given by the fastest of the two spin-flip processes. In our case the spin flip is most likely to be explained by the spin-orbit coupling as the hyperfine interaction of the electron[1] spin with the lattice nuclei can be neglected in the case of neutral (uncharged) excitons for which the field caused by the exchange interaction with the hole is stronger than the effective field created by the lattice nuclei [14].

5.3 Excitation intensity dependence of the spin-flip rate

Experimental conditions

Two different measurement series are acquired: one in which the quantum dots are excited through pumping in the GaAs barriers states at 1.64 eV and one in which the excitation is performed by pumping in the wetting layer states at 1.45 eV. For the case of barrier pumping the intensity is varied over more than 4 orders of magnitude from $3\,\mathrm{mW/cm^2}$ to $70\,\mathrm{W/cm^2}$ corresponding to a variation in the excitation density in the GaAs barrier from 0.003 to 70 excitons per quantum dot. The count rates obtained for the various excitation densities are shown in Fig. 5.1(b). A deviation from a linear dependence on excitation density (shown by the solid red line) sets in for densities around ~ 1 exciton per quantum dot supporting the estimate of the excitation density[2]. In the case of wetting-layer

[1] The hole spin is only weakly coupled to the lattice due to the p-symmetry of the wavefunctions. [14]

[2] For excitation densities above ~ 5 excitons per quantum dot the emission from the GaAs-exciton increases super-linearly, i.e., at strong excitation densities a larger fraction of the created excitons will not be captured into the quantum dots, but emitted from the bulk GaAs and the wetting-layer states.

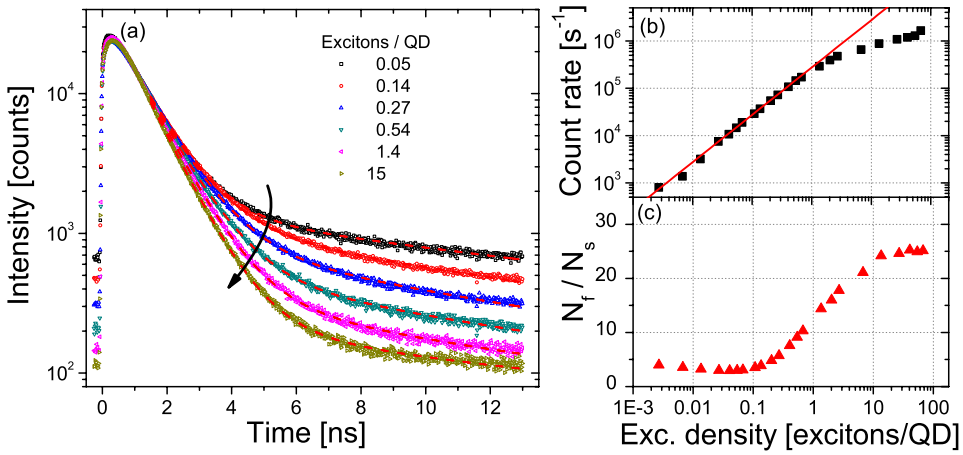

Fig. 5.1: **(a)** Decay curves (excitation in GaAs barrier) for a series of measurements for excitation densities between 0.05 and 15.0 excitons. The decay curves have been scaled to the decay curve obtained at an excitation density of 0.05 excitons per quantum dot at $t = 1.0$ns. **(b)** Count rate versus excitation density. **(c)** The ratio of the total number of photon counts in the fast and and slow components. As the excitation density is increased the photon counts are redistributed from the slow to the fast component.

excitation the density is varied between 0.03 and 7 excitons per quantum dot. The wafer used in the experiment (NBI-167) is the same as used in the previous chapters and the sample chosen for the measurements is the one furthest away from the interface, $z = 302$ nm. The measurements are performed at 1.201 eV.

Time-resolved measurements

The decay curves for a series of measurements for excitation densities between 0.05 and 15 excitons per quantum dot are shown in Fig. 5.1(a). The five decay curves show a clear dependence on the excitation density; as the excitation density is increased the slow component is suppressed. By visual inspection we find that the decay curves saturate in the lower limit as well as in the upper limit of the excitation densities (not shown in Fig. 5.1(a)). This observation is confirmed by the saturation of the ratio of the total number of photons in the fast and slow components shown in Fig. 5.1(c) in both the weak and the strong excitation limits.

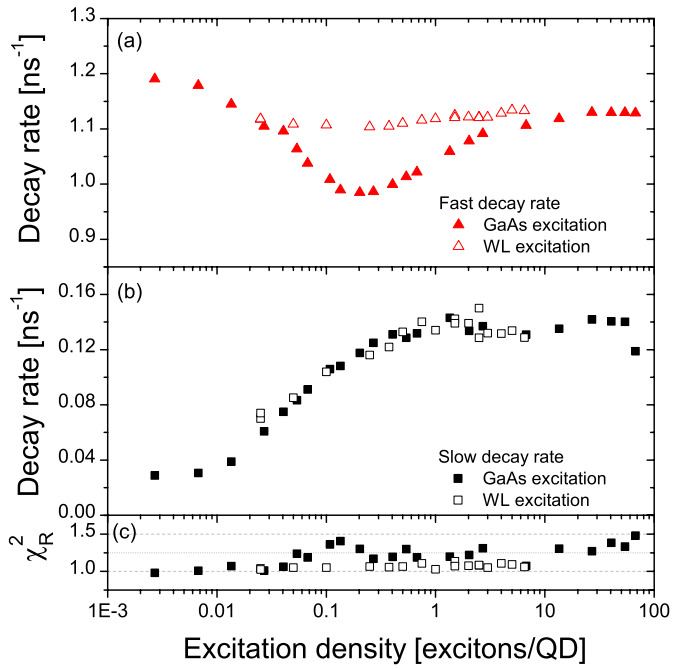

Fig. 5.2: **(a)** The fast and **(b)** the slow decay rates obtained from the bi-exponential fits and **(c)** the corresponding χ^2_{R}-values.

The total number of photons in the fast and slow components are readily calculated from the bi-exponential model as $N_i = \int_0^\infty A_i \exp(-\gamma_i t)\, dt = A_i/\gamma_i$, where $i = \mathrm{s,f}$. A redistribution of photon counts from the slow to the fast component is readily observed with increasing excitation intensity. This redistribution is mainly attributed to changes in the population probabilities of the bright and dark states as will be explained in details below. However, part of this redistribution is caused by changes in the spin-flip rate.

The fast and slow decay rates obtained from the bi-exponential model fitted to the data are shown in Figs. 5.2(a) and 5.2(b) respectively. In accordance with this model we assign the fast rate to the total decay of bright excitons, i.e., the sum of the radiative decay rate, the non-radiative decay rate, and the spin-flip rate from bright to dark excitons: $\Gamma_{\mathrm{f}} = \gamma_{\mathrm{rad}} + \gamma^{\mathrm{b}}_{\mathrm{nrad}} + \gamma_{\mathrm{bd}}$, while the slow rate is due to the total decay of the dark excitons, i.e., the sum of the non-radiative decay rate and

the spin-flip rate from dark to bright excitons: $\Gamma_s = \gamma^d_{nrad} + \gamma_{db}$. The fast decay rate exhibits an interesting non-monotonically dependence on the excitation density. This suggests the existence of two competing processes: one which decreases with excitation density and one which increases with excitation density. We identify two processes which could cause an increased rate with increased excitation: i) carrier-carrier scattering, leading to an increase in the non-radiative or spin-flip rates, ii) radiative recombination of bi-excitons, which are known to decay faster than the excitons [18–20]. The reduction in the decay rate with increasing excitation density could be due to a reduction of the wavefunction overlap as more and more carriers are introduced into the quantum dots. While the qualitative behaviour is identical for excitation in the GaAs barrier and in the wetting layer, the quantitative variations are strikingly different: in the case of wetting layer excitation the variation is about 2% while the excitation in GaAs results in much stronger variations on the order of 20%. In both cases a minimum rate is found at an excitation density of ~ 0.2 excitons per quantum dot. We have not identified a plausible cause for this quantitative deviation. However, it excludes radiative recombination of bi-excitons (ii) as a possible cause of the increased decay rate with increasing excitation density; for a given excitation density the possibility for a quantum dot to be populated by a bi-exciton is similar in the two cases.

The slow decay rate experiences a monotonically five-fold increase with an increase in the excitation density from 0.003 to 1 excitons per quantum dot after which it settles at a value of $\sim 0.14\,\mathrm{ns}^{-1}$. Again an increased carrier-carrier scattering could be the process behind, causing an increase in the non-radiative or spin-flip rate. The fact that the rate settles at a constant value for excitations above 1-2 excitons per quantum dot indicates a relation to the filling of the ground state exciton level, i.e., the decay rate saturates as the possibility of the dark exciton being created by the *non-radiative* decay of a bi-exciton becomes dominant. For the slow decay rate there is no quantitative deviation between the rates obtained under different excitation energy.

The spin-flip rate γ_{db} can be obtained from Eq. (5.4) if the ratio of the initial populations is known. This ratio depends in general on the exact excitation conditions, i.e., excitation energy and density. However, in the case of weak excitation in the GaAs (non-resonant), the probability of generating bright and dark excitons can be assumed to be equal: $\frac{\rho_d(0)}{\rho_b(0)} = 1$. This assumption is based on the observation of non-geminate capture of carriers into quantum wells under non-resonant excitation [21] and a very rapid hole-spin relaxation prior to capture into

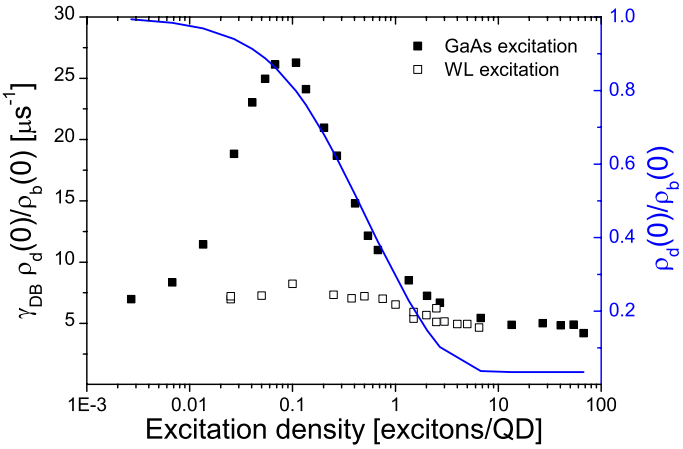

Fig. 5.3: Left axis: $\gamma_{\mathrm{db}}\frac{\rho_{\mathrm{d}}(0)}{\rho_{\mathrm{b}}(0)}$ deduced from the bi-exponential fit. Right axis: $\frac{\rho_{\mathrm{d}}(0)}{\rho_{\mathrm{b}}(0)}$ calculated using a numerical five level model.

the quantum dot states [10]. In the weak excitation regime the spin-flip rate is thus accordingly determined to be $\gamma_{\mathrm{db}} = 7\,\mu\mathrm{s}^{-1}$. This is in agreement with an upper limit of $\gamma_{\mathrm{db}} < 20\,\mu\mathrm{s}^{-1}$ deduced from measurements on electrically gated single quantum dots [7] and with single quantum dot measurements at 5 K for which rates of $5\,\mu\mathrm{s}^{-1}$ and $70\,\mu\mathrm{s}^{-1}$ are reported [8]. The low value of the spin-flip rate clearly justifies the assumption of $\gamma_{\mathrm{bd}}, \gamma_{\mathrm{db}} \ll \gamma_{\mathrm{rad}} + \gamma^{\mathrm{b}}_{\mathrm{nrad}} - \gamma^{\mathrm{d}}_{\mathrm{nrad}}$ made in Sec. 2.2.4. The measured rate is in strong contrast to the high spin-flip rates ($> 5\,\mathrm{ns}^{-1}$) reported in [3–5] obtained under non-resonant excitation. This large discrepancy readily displays the difference between the *intrinsic* spin-flip rate and the decay rate of the spin-polarization during relaxation in the quantum dot. These results thus confirm a fast spin relaxation either during the short time in the bulk prior to capture into the quantum dot or during the energy relaxation through the excited states.

In Fig. 5.3 we plot $\gamma_{\mathrm{db}}\frac{\rho_{\mathrm{d}}(0)}{\rho_{\mathrm{b}}(0)}$ deduced from the measurements at the various excitation densities. In the weak excitation limit ($\frac{\rho_{\mathrm{d}}(0)}{\rho_{\mathrm{b}}(0)} = 1$) the spin-flip rate is readily seen to attain a value of $\gamma_{\mathrm{db}} = 7\,\mu\mathrm{s}^{-1}$. By calculating the dependence of the ratio of the initial populations on excitation density, it is possible to obtain knowledge of the spin-flip rate's dependence on the excitation density. The initial populations are calculated by solving a five-level rate equation which apart from

the ground, bright and dark states include the bi-exciton level and a reservoir level. The model is discussed in Appendix B, so here the results will be used without further justification. The ratio of the calculated initial populations is shown by the solid blue line in Fig. 5.3. The ratio decreases from its initial value of unity to a value of ~ 0.05 for excitation densities above ~ 3 excitons per quantum dot. The change in population ratio is due to the different possibilities of the bi-exciton decay leaving either a bright or a dark exciton behind. A radiative decay of the bi-exciton will always leave a bright exciton behind, while a non-radiative decay results in equal possibilities of leaving either a bright or a dark exciton behind. The possibility of the quantum dot being in a bright or a dark exciton state after a decay of the bi-exciton is thus given by the quantum efficiency of the bi-exciton. The reduction in the ratio of the calculated initial populations can qualitatively explain the corresponding decrease in the measured $\gamma_{\mathrm{db}}\frac{\rho_{\mathrm{d}}(0)}{\rho_{\mathrm{b}}(0)}$ for densities above 0.01 exciton per quantum dot. Assuming a quantum efficiency of 0.9 (0.8) for the bi-exciton[3] we obtain a spin-flip rate of $\gamma_{\mathrm{db}} = 95\,\mu\mathrm{s}^{-1}$ $(45\,\mu\mathrm{s}^{-1})$ in the limit of strong excitation. While the precise determination of the spin-flip rate in the strong excitation limit is difficult, it can safely be concluded that the spin-flip rate increases with increasing excitation density as the initial increase in $\gamma_{\mathrm{db}}\frac{\rho_{\mathrm{d}}(0)}{\rho_{\mathrm{b}}(0)}$ must be due to a corresponding increase in γ_{db}.

The same qualitative dependence of the spin-flip rate on excitation density is observed under the two different excitation conditions. However, the wetting layer excitation results in values of $\gamma_{\mathrm{db}}\frac{\rho_{\mathrm{d}}(0)}{\rho_{\mathrm{b}}(0)}$ which are approximately 4 times lower than those obtained under excitation in the GaAs barrier. It is not likely that the spin-flip rate will be so strongly affected by a change in the excitation energy. The difference is more likely due to a change in the ratio of the initial populations. When the excitation energy is resonant with the wetting layer states and thus close to the energy levels of the quantum dots, it is plausible that the ratio of the excitons (germinate) to the individual carriers (non-germinate) which are captured in the quantum dot increases. This would lead to a higher ratio of bright to dark excitons in the quantum dots and thus a lower value of $\gamma_{\mathrm{db}}\frac{\rho_{\mathrm{d}}(0)}{\rho_{\mathrm{b}}(0)}$.

From the analysis of the decay dynamics above we can conclude that the spin-flip rate is dependent on the excitation density. Under weak excitation we find a spin-flip rate of $\gamma_{\mathrm{db}} = 7\,\mu\mathrm{s}^{-1}$ which increases for increasing excitation density. By

[3] In a first approximation we can assume that the bi-exciton simply inherits the properties of the excitons, whereby it acquires a radiative decay rate which is twice the radiative decay rate of the excitons and a non-radiative decay rate which is twice the non-radiative decay rate of the exciton. The quantum efficiency of the bi-exciton and the exciton will thus be identical.

assuming identical quantum efficiencies of the exciton and bi-exciton, we find a spin-flip rate under strong excitation which is $\gamma_{\mathrm{db}} = 95\,\mu\mathrm{s}^{-1}$. While the increase in the spin-flip rate is substantial, it accounts only partly for the increase in slow and fast rates shown in Fig. 5.2. We can therefore conclude that the non-radiative decay rate also increases with increasing excitation density.

5.4 Excitation energy dependence of the spin-flip rate

Sample preparation

The measurements for various excitation energies are performed on a wafer (NBI-178) containing InAs/GaAs quantum dots which are nominally identical to those used in the experiments in the previous chapters. The quantum dots under study have been grown on a GaAs (100) substrate where 2.0 monolayers of InAs are deposited at 515° C followed by a 30 s growth interrupt and deposition of a 80 nm thick GaAs cap. The quantum dot density is $250\,\mu\mathrm{m}^{-2}$. A 2 µm thick layer of $Al_{0.7}Ga_{0.3}As$ is deposited 80 nm below the quantum dots for an optional under etch since the wafer is grown for the purpose of fabricating photonic crystal membranes, c.f. Chapter 6. The inhomogenously broadened ground state is centred at an emission energy of 1.264 eV.

Experimental conditions

An excitation density of 0.2 excitons per quantum dot is chosen in order to stay in the weak excitation regime. The density must be similar for all different excitation energies as it will otherwise influence the decay dynamics as discussed in the previous section. Similar excitation densities are obtained by adjusting the power to keep the count rates at a constant level ($\sim 3.4 \cdot 10^4$ cps) when changing the excitation energy. A verification of the close-to-constant excitation density is shown in the inset of Fig. 5.4 where the count rate stemming from the quantum dot signal is shown as a function of the excitation energy. The variation in the count rate corresponds to ±15%. The excitation energy is varied between 1.319 eV and 1.531 eV and the spectral FWHM of the excitation pulse is typically 10 meV. The time-resolved measurements are acquired at 1.264 eV, i.e., at the centre of the ground state emission.

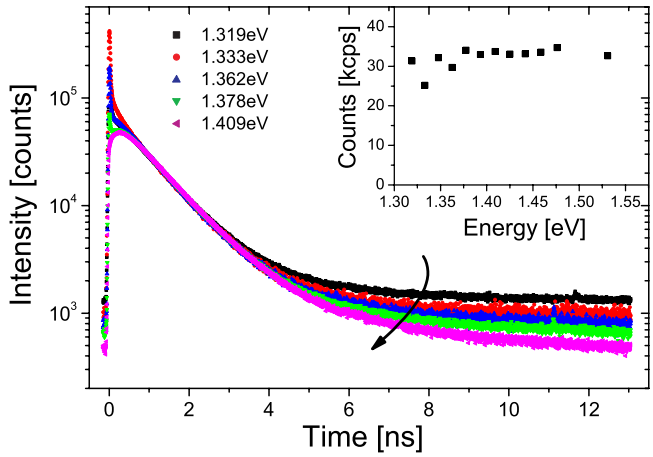

Fig. 5.4: Decay curves for a series of measurements for excitation energies between 1.319 eV and 1.409 eV. The decay curves have been scaled to the decay curve obtained for an excitation density of 1.319 eV at $t = 1.0$ns. **Inset**: The count rate for which the laser contribution has been subtracted verifies a close-to-constant excitation density.

Time-resolved measurements

The excitation energy for the decay curves shown in Fig. 5.4 is varied between 1.319 eV and 1.409 eV. While the fast rate is almost unaffected by the variation in the excitation energy, the slow rate exhibits a clear decrease with decreasing excitation energy. The spectral tails of the excitation laser start to appear in the decay curves as the separation of the excitation energy and detection energy is reduced. The bi-exponential model is thus fitted from $t = 1.25$ ns and onward. The fast and slow rates obtained are shown in Fig. 5.5(a). While the fast decay rate varies less than $\pm 4\%$, the slow decay rate displays an almost linear increase with increasing excitation energy below the energy of the wetting layer states. For excitation energies above the wetting layer the slow rate is nearly constant. The abrupt change in the dependence of the slow decay rate occurs as the excitation energy is close-to resonant with the wetting layer. This indicates that the slow decay rate is dependent on:

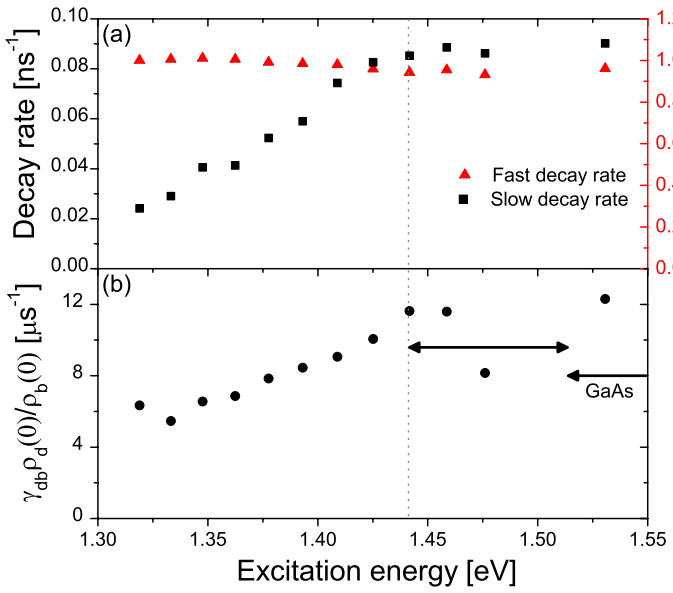

Fig. 5.5: **(a)** The slow (left) and fast (right) decay rates under various excitation energies. **(b)** The product of the spin-flip rate and the ratio of the initial populations. The GaAs states and the wetting layer states are indicated by the arrows - the vertical dotted line indicates the bottom of the wetting layer states.

- The relaxation of the excess energy of the initially hot excitons. The measurements are performed under weak excitation and carrier-carrier scattering are therefore neglected whereby phonon emission is the only process for dissipating the excess energy. The linear dependence is only observed below the wetting layer, suggesting that only the excess energy dissipated after the exciton has been captured in the quantum dot which affects the decay rate. This implies that phonons which are emitted from the exciton while it is localized in the quantum dot have a clear effect on the slow decay rate.

- The presence of single carriers due non-geminate population capture. While excitation in the GaAs leads to a random capture of single carriers [21], strictly resonant excitation corresponds to a direct injection of an exciton in the quantum dot. The non-geminate carrier capture leads to a equal population of dark and bright excitons, while strictly resonant excitation

leads to the formation of bright excitons only. It is thus plausible that an abrupt change in the dark-bright ratio $\frac{\rho_{\mathrm{d}}(0)}{\rho_{\mathrm{b}}(0)}$ will occur at the energy of the wetting layer, as direct non-geminate capture is not possible at energies below the wetting layer.

The product of the spin-flip rate and the ratio of the initial populations $\gamma_{\mathrm{db}}\frac{\rho_{\mathrm{d}}(0)}{\rho_{\mathrm{b}}(0)}$ is shown in Fig. 5.5(b) as a function of excitation energy. As in the case of the slow decay rate an increase with increasing energy is observed for energies below the wetting layer. Above the wetting layer energy the rates do not show a clear constant level, however, three of the four data points have very similar values. Unfortunately, we do not have sufficient data to conclude whether the low value obtained at an excitation energy of 1.47 eV is caused by some kind of resonance. The apparent difference from the value obtained for GaAs excitation is in qualitative agreement with the deviation observed and discussed in Sec. 5.3.

The nearly linear dependence of the spin-flip rate on excitation energy below the wetting layer could, as argued above, be due to a direct change in the ratio of the initial populations, implying a change in the ratio by a factor of ~ 3. Another possible explanation could be an increase in the spin-flip rate due to scattering on a non-equilibrium phonon population created during relaxation. The latter has been suggested as the cause of the drastic reduction in the spin-flip rate under resonant excitation compared with excitation in the barrier [22].

Since a separation of the spin-flip rate from the ratio of the initial populations is not possible, we cannot conclude which of the two possible causes is the most likely.

5.5 Energy and structural dependence of the spin-flip rate

By analysing the data presented in Sec. 3.3, from which we have obtained the oscillator strength and quantum efficiency in the bright-dark exciton model, the energy and structural dependence of the spin-flip rates can be obtained. The experimental conditions and sample preparation are given in Sec. 3.3.

We expect that the ratio of initial populations $\frac{\rho_{\mathrm{d}}(0)}{\rho_{\mathrm{b}}(0)}$ is independent of the ground state energy since the population of the individual quantum dots are governed by Poissonian statistics [23], i.e., the excitons captured in the quantum dot ensemble are not in thermal equilibrium. The spin-flip rates presented here are thus all obtained under the assumption of $\frac{\rho_{\mathrm{d}}(0)}{\rho_{\mathrm{b}}(0)} = 0.8$, in accordance with the calculation shown in Fig. 5.3. The obtained spin-flip rates, shown in Fig. 5.6, display

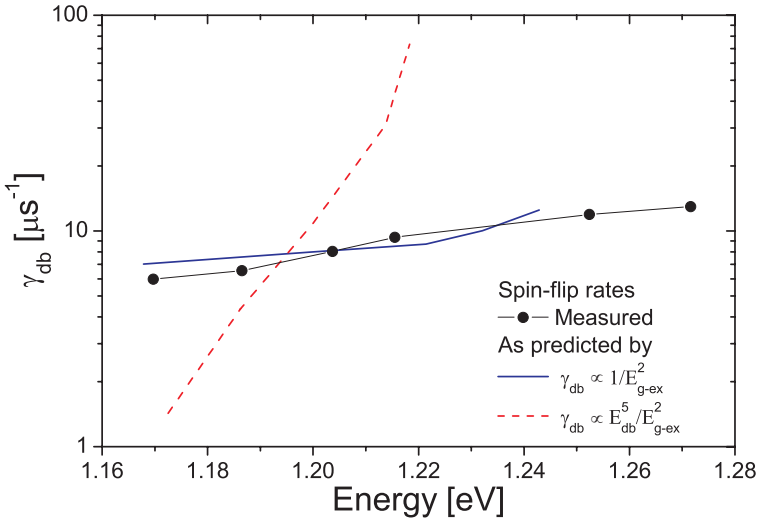

Fig. 5.6: The measured energy dependence of the spin-flip rate (solid black circles). Predicted energy dependence of the spin-flip rate in case of phonon mediated (blue solid line) [4] and deformation caused (red dashed line) [24] spin-flip process.

a clear increase with increasing emission energy. This dependence of the spin-flip rate on the ground state energy may help to identify the mechanisms causing the spin-flip. In the following we will discuss the energy dependence in the two cases where the spin-flip is: i) phonon mediate and due to spin-orbit interaction [4], and ii) due to the interplay between the short-range exchange interaction and deformation caused by phonons [24, 25].

Phonon-mediated spin-orbit interaction

In this case the hypothesis is that the excited states of the quantum dot have mixed spin character. Spin flips of the ground state exciton is thus possible by a transition to the first excited state by absorption of a virtual phonon [4]; as the spin axis of the excited state does not coincide with the spin axis of the ground state, there is a finite probability that a transition back and forth will result in a spin flip. Different observations lend support to the mixed spin character of the excited states: i) the absorption of light polarized both in-plane and out-of-plan from the excited states [26], indicating mixing of the light and heavy hole bands, and ii) calculations using $\boldsymbol{k} \cdot \boldsymbol{p}$ theory as reported in [4].

The spin-flip rate is expected to have an inverse dependence on the level spac-

ing between the ground and first excited state: $\gamma_{\mathrm{db}} \propto 1/E^2_{\mathrm{g-ex}}$, c.f. Ref. [4]. The level spacing is, in contrast to the intuitive predictions of an infinite-barrier model, measured to decrease with increasing ground state energy [27]. In full agreement with our measurements reported in Chapter 4, the measured decrease in level spacing is explained by a reduction of the overlap of the electron and hole wavefunctions with increasing ground state energy. This decrease in level spacing results in an increase in the spin-flip rate with increasing ground state energy, just as we observe in Fig. 5.6. The theoretical prediction (solid blue line in Fig. 5.6) is compared to the measured spin-flip rates with the use of the level spacings $E_{\mathrm{g-ex}}$ reported in Ref. [27]. In order to better compare theory and data, the energy axis of the theory curve has been scaled by 1.07 to coincide with energy axis of the measurements. A remarkably good agreement between data and the theory is observed. Our measurements can thus lend further support to a phonon-mediated spin-orbit interaction as a possible mechanism causing the spin-flip.

Short-range exchange interaction and phonon-caused deformation

Another possible spin-flip mechanism is the interplay of the short-ranged exchange interaction and the deformations caused by acoustic phonons as suggested in [24, 25]. The energy dependence of the spin-flip rate is in this case predicted to increase drastically with an increased electron-hole exchange energy: $\gamma_{\mathrm{db}} \propto E^5_{\mathrm{bd}}/E^2_{\mathrm{g-ex}}$. In situations where the symmetry is broken, e.g., under strong magnetic fields, the electron-hole exchange energy can be measured due to mixing of the bright and dark states. Exchange energies extrapolated to zero magnetic field are reported to attain values of 100 to 250 μeV and to display an increase with increasing ground state energy [28]. Using the exchange energies measured in Ref. [28] and the level spacing measured in Ref. [27] we compare the theory to the experiment. The theoretical prediction is shown by the dashed red line in Fig. 5.6. The energy scale of the data reported in Ref. [28] has been scaled by 0.92 in order to coincide with the energy range of the experiment. The drastic E^5_{bd} dependence predicted by theory is not in correspondence with our measurements.

In relation to the measured exchange energies [28], it should be noted that dependence of the exchange energy on ground state energy is explained by a direct proportionality between the exchange energy and the probability of the electron and hole being at the same position [29, 30], i.e., the overlap of the electron and hole wavefunctions. The results reported thus imply that the wavefunction overlap must increase with increasing ground state energy as also argued by the authors;

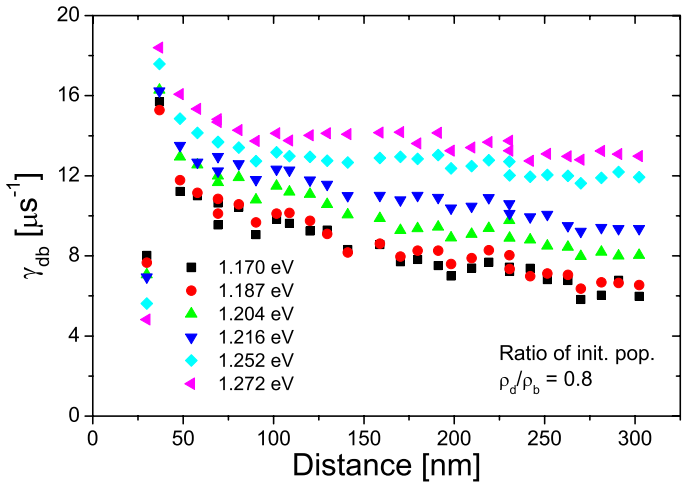

Fig. 5.7: The spin-flip rates versus distance for six different energies. For all distances the spin-flip rate is highest for high-energy quantum dots. A clear structural dependence is observed: quantum dots close to the interface exhibit larger spin-flip rates. The rates are obtained using $\frac{\rho_d(0)}{\rho_b(0)} = 0.8$.

however, from our measurements and calculations of the wavefunction overlap, c.f. Sec. 3.3, we can readily conclude that the opposite is the actual case. Furthermore, for the data reported in [31] a linear relation between the exchange energy and the wavefunction overlap implies that the wavefunction overlap should be reduced by more than than 60% going from high-energy to low-energy quantum dots which seems implausible.

5.5.1 Structural dependence of the spin-flip rate

An inspection of the spin-flip rates ($\frac{\rho_d(0)}{\rho_b(0)} = 0.8$) obtained for all the 30 distances, shown in Fig. 5.7, reveals a surprising structural dependence. The energy dependence of the spin-flip rate discussed above is verified for all distances. However, the absolute value of the spin-flip rate depends on the distance to the interface; that is, as the quantum dots are getting closer to the interface the spin-flip rate increases. Furthermore, the dependence on the distance is found to be more and more pronounced with decreasing emission energy.

The ratio of the initial populations is expected to be independent on the distance as the excitation is done by excitation in wetting layer states, i.e, the varying thickness of the top-most GaAs layer is of no concern. Again, we turn to the spin-flip rate for a possible explanation of the the distance dependence. We suggest that the dependence could be caused by either surface acoustic phonons or band bending due to electronic surface states at the interface. Surface acoustic phonons with an energy corresponding to the exchange splitting could mediate the spin-flip process. Another cause could be band bending of the conduction and valence band due to electronic surface states at the air-GaAs interface. Such a band bending would lead to a deformation of the wavefunctions and a possible change in both the electron-hole exchange splitting and the level spacing. However, if this was the case we would expect to observe modifications in the oscillator strength and thus the decay rate within the same distance to the interface. The measured decay rates shown in Sec. 3.3 do exhibit a pronounced deviation close to the interface, however, only for distances shorter than 70 nm, for the spin-flip rate the characteristic length scale is ~ 200 nm.

5.6 Detailed study of the decay dynamics over long time scales

A more detailed study of the slow components is facilitated by reducing the repetition rate of the excitation source. This directly results in the possibility to measure slower rates, but it also results in a larger dynamic range allowing for a better resolution of the different decay rates.

Experimental conditions

The excitation is performed using a laser diode delivering 62 ps long pulses at a repetition rate of 5 MHz. The excitation energy is 1.59 eV corresponding to excitation in the GaAs-barrier. The excitation spot has a diameter of $\sim 75\,\mu$m and the measurements are performed at excitation densities of 0.36, 1.1, 3.6, 11, and 36 excitons per quantum dot. The temperature is adjusted to 10 K, 16 K, 25 K, 36 K, and 50 K. The wafer used in the experiment is the one used for interface experiment presented in Chapter. 3 (NBI-167). The sample chosen for the measurements is the one with a distance to the interface of $z = 263$ nm. The measurements are performed at an emission energy of 1.187 eV.

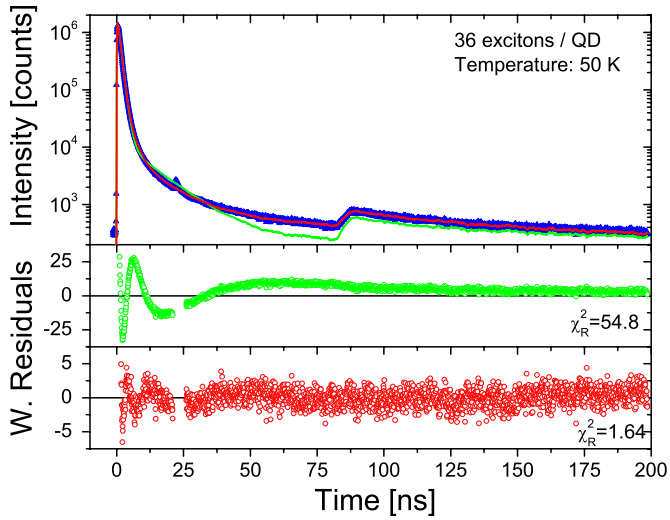

Fig. 5.8: Time-resolved emission acquired over 200 ns. The two artifacts observed in the decay curve are due to an unavoidable reflection in the APD's entrance window (22 ns) and after-pulsing events in the detector (80 ns). The after pulsing is accounted for by the instrument response, as readily seen by the fitted models which reproduce the pump at 80 ns. The time range including the reflection is removed prior to fitting of the model.

5.6.1 Time-resolved measurements acquired over short and long time spans

The time-resolved emission acquired at an excitation density of 36 excitons per quantum dot and at a temperature of 50 K is shown in Fig. 5.8(a). In contrast to the data acquired over a shorter time span of 13 ns, a bi-exponential decay (shown by the solid green line) is no longer able to model the data. This can be clearly seen from the weighted residual shown in Fig. 5.8(b). The improve dynamic range resolves that the decay dynamics exhibits a multi-exponential decay. We suggest that the multi-exponential behaviour is due to a distribution of slow decay rates within the ensemble; this could be a distribution of either the non-radiative decay rate or the spin-flip rate. A distribution of the non-radiative decay rate is plausible if the non-radiative decay rate is related to the surface states as suggested in Sec. 3.3 and thus is a property of the single quantum dot. Strong variations

in the spin-flip rates obtained on single quantum dots support the suggestion of a distribution of the spin-flip rate within the quantum dot ensemble [8].

We keep the distinction between the fast and slow decay rates due to their different causes, i.e., the decay of bright and dark excitons, respectively. Variations in either the non-radiative or the spin-flip rate will only result in minor variations in the fast decay rate as these variations are small compared to the radiative decay rate of the bright excitons. The fast decay rate is thus continuously modelled as a mono-exponential decay. The correct method for describing the multi-exponential decay of the slow component is to introduce a distribution of slow decay rates $\sigma_{\mathrm{s}}(\Gamma)$. The microscopic distribution is however unknown and as we are interested in obtaining the properties of the quantum dot ensemble, we instead extract the average decay time, $\bar{\tau}_{\mathrm{s}}$. This average decay time is well defined and can be calculated either directly from the decay curve or from a given model $N(t)$ of the decay. The average decay rate $\bar{\gamma}_{\mathrm{s}}$ is calculated as [4]:

$$\frac{1}{\bar{\gamma}_{\mathrm{s}}} = \bar{\tau}_{\mathrm{s}} = \frac{\int_0^\infty N(t)t\,dt}{\int_0^\infty N(t)\,dt}. \tag{5.6}$$

We model the slow component as a multi-exponential decay from which the average decay rate and the total number of counts in the slow component are easily obtained.

The ratios of the number of photon counts in the fast and slow components are shown for various excitation densities in Fig. 5.9(a). The ratios are compared to those obtained from measurements acquired under a shorter repetition period of 13 ns. The latter are presented in Sec. 5.3 in more details. The ratios are in good agreement, displaying the same dependence on excitation density and attaining similar values. This explicitly verifies that we are indeed able to gain information on the spin-flip rate from the data acquired over shorter time spans of only 13 ns. The slow decay rates obtained under the two different repetition periods are shown in Fig. 5.9(b) where they exhibit similar dependencies on the excitation density. The absolute values of average decay rates (200 ns) are however approximately a factor of 3 lower than the slow decay rates obtained from the 13 ns measurements. This is readily understood as only the fastest rates will be evident in the measurements acquired over short time scales. The observed difference by a factor of 3 suggests that the spin-flip rates obtained from the data acquired over the short time span of 13 ns are overestimated by a factor of ~ 3, c.f. Eq. (5.4). This

[4] In the case of a mono-exponential decay, $N(t) = A\exp(-\gamma_{\mathrm{A}}t)$, the average rate is identical to the decay rate: $\bar{\gamma} = \gamma_{\mathrm{A}}$.

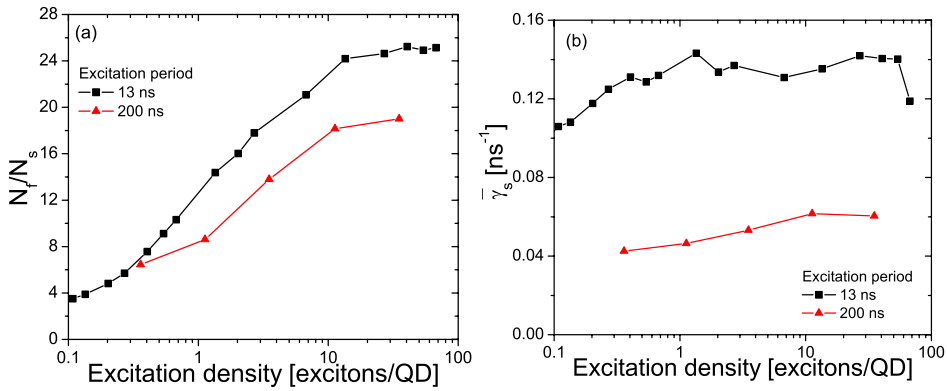

Fig. 5.9: Comparison of the ratio of total photon counts in the slow and the fast components **(a)** and the slow decay rate **(b)** for measurements acquired over time spans of 13 ns and 200 ns.

implies that the spin-flip rates obtained under low excitation in Sec. 5.3 should be corrected to $\sim 2\,\mu s^{-1}$ instead of $7\,\mu s^{-1}$ and in the limit of strong excitation the estimated spin-flip rate is corrected to $\sim 30\,\mu s^{-1}$ instead of $95\,\mu s^{-1}$.

5.6.2 Temperature dependence of the spin-flip rate

Time resolved measurements

The spin-flip rates obtained for the various temperatures and excitation densities are shown in Fig. 5.10. The rates exhibit an overall increase with increasing temperature for all excitation densities.

Independent of whether the spin-flip arises from a direct phonon-assisted thermalization [9] or from a combined effect of the phonon coupling to the hole spin states and the short range exchange interaction [24], acoustic phonons are needed to supply the energy difference between the dark and the bright exciton states. The density of acoustic phonons at an energy of E_{bd} is given by the Bose-Einstein number:

$$N_{\mathrm{B}} = \frac{1}{\exp(E_{\mathrm{bd}}/k_{\mathrm{B}}T) - 1}, \tag{5.7}$$

where T denotes the temperature. A linear temperature dependence of the spin-flip rate is therefore expected for $k_{\mathrm{B}}T > E_{\mathrm{bd}}$, i.e., $T > 2\,\mathrm{K}$ for a typical bright-dark

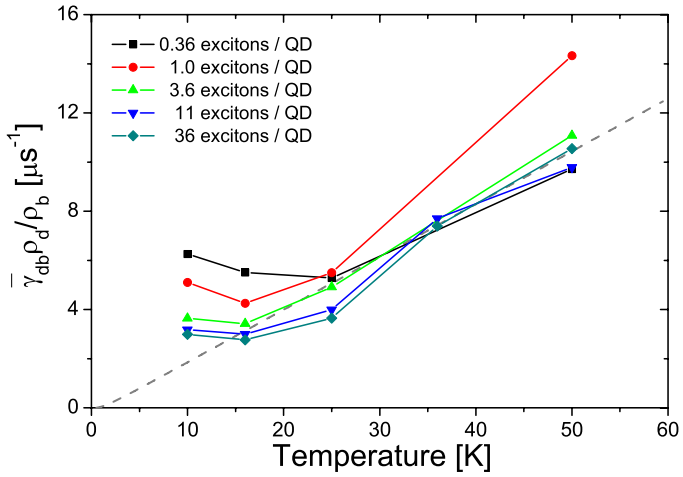

Fig. 5.10: Spin-flip rates obtained for the various temperatures and excitation densities.

splitting in InAs quantum dots of $E_{\mathrm{bd}} = 0.250\,\mathrm{meV}$ [31]. The phonon-assisted spin-flip rates can thus be described as

$$\gamma_{\mathrm{db}} = \gamma_0 N_{\mathrm{B}}, \qquad \gamma_{\mathrm{bd}} = \gamma_0 (N_{\mathrm{B}} + 1), \tag{5.8}$$

where the zero temperature relaxation rate from the bright to the dark states is given by γ_0.

For quantitative comparison we have plotted a theory curve calculated for $E_{\mathrm{bd}} = 0.250\,\mathrm{meV}$ and $\gamma_0 = 0.62\,\mu\mathrm{s}^{-1}$ in Fig. 5.10. The measurement and theory display an qualitative agreement. However, for low temperatures we observe a small increase in the measured spin-flip rates with decreasing temperature. For an understanding of this effect it would be beneficial to have knowledge of quantum efficiency's dependence on temperature. Moreover measurements on single quantum dots would also be of great value.

5.7 Conclusion

We have studied the decay dynamics and obtained the dark-to-bright spin-flip rate for the exciton ground state in quantum dot ensembles under various excitation conditions, different emission energies and for various distances to a dielectric in-

terface. Comparing data acquired over 13 ns and 200 ns we conclude that we are able to obtain spin-flip rates even over so short time spans as 13 ns; however, the rates must be corrected by a factor ~ 3 in order to compensate for the weighting of the fast components. Moreover, we find that the slow decay component exhibits a multi-exponential decay, suggesting that the slow decay rate is given by a distribution of decay rates within the quantum dot ensemble.

We find that the spin-flip rate is strongly affected by the excitation density increasing from $\sim 2\,\mu s^{-1}$ under weak excitation to $\sim 30\,\mu s^{-1}$ under strong excitation. Under variation of the excitation energy the slow decay rate and the spin-flip rate are found to vary strongly. The possible causes for these variations are discussed in details. We measure an increase in the spin-flip rates with increased quantum dot emission energy. This observation is discussed in the context of two different proposals for a spin-flip mechanism. Our measurements lend qualitative support to the work of Gündoğdu *et al.* [4] in which they suggest the spin-flip mechanism to be due to scattering by virtual phonons back and forth to the the excited. We report a structural dependence of the spin-flip rates exhibiting an increased rate as the quantum dot ensemble approaches an interface. Finally, the temperature dependence of the spin-flip rate is measured and we find an increase in the rate with increasing temperature, this is in general agreement with the spin-flip rate being proportional to the density of acoustic phonons.

References to Chapter 5

[1] S. Strauf, N. G. Stoltz, M. T. Rakher, L. A. Coldren, P. M. Petroff, and D. Bouwmeester, *High-frequency single-photon source with polarization control*, Nature Photonics 1, 704 (2007).

[2] D. Loss and D. P. DiVincenzo, *Quantum computation with quantum dots*, Phys. Rev. A 57, 120 (1998).

[3] K. Gündoğdu, K. C. Hall, T. F. Boggess, D. G. Deppe, and O. B. Shchekin, *Efficient electron spin detection with positively charged quantum dots*, App. Phys. Lett. 84, 2793 (2004).

[4] K. Gündoğdu, K. C. Hall, E. J. Koerperick, C. E. Pryor, M. E. Flatté, T. F. Boggess, O. B. Shchekin, and D. G. Deppe, *Electron and hole spin dynamics in semiconductor quantum dots*, App. Phys. Lett. 86, 113111 (2005).

[5] K. C. Hall, E. J. Koerperick, T. F. Boggess, O. B. Shchekin, and D. G. Deppe, *Hole spin relaxation in neutral InGaAs quantum dots: Decay to dark states*, App. Phys. Lett. 90, 053109 (2007).

[6] T. Amand, X. Marie, M. Sénèsa, O. Krebs, S. Laurent, S. Cortez, P. Voisin, and J. M. Gérard, *Spin dynamics of neutral and charged excitons in InAs/GaAs quantum dots: towards Q-bit implementation?*, Superlattices and Microstructures 32, 157 (2002).

[7] J. M. Smith, P. A. Dalgarno, R. J. Warburton, A. O. Govorov, K. Karrai, B. D. Gerardot, and P. M. Petroff, *Voltage Control of the Spin Dynamics of an Exciton in a Semiconductor Quantum Dot*, Phys. Rev. Lett. 94, 197402 (2005).

[8] I. Favero, G. Cassabois, C. Voisin, C. Delalande, P. Roussignol, R. Ferreira, C. Couteau, J. P. Poizat, and J. M. Gérard, *Fast exciton spin relaxation in single quantum dots*, Phys. Rev. B 71, 233304 (2005).

[9] O. Labeau, P. Tamarat, and B. Lounis, *Temperature Dependence of the Luminescence Lifetime of Single $CdSe/ZnS$ Quantum Dots*, Phys. Rev. Lett. 90, 257404 (2003).

[10] I. Žutić, J. Fabian, and S. Das Sarma, *Spintronics: Fundamentals and applications*, Rev. Mod. Phys. 76, 323 (2004).

[11] D. J. Hilton and C. L. Tang, *Optical Orientation and Femtosecond Relaxation of Spin-Polarized Holes in GaAs*, Phys. Rev. Lett. 89, 146601 (2002).

[12] A. V. Khaetskii and Y. V. Nazarov, *Spin relaxation in semiconductor quantum dots*, Phys. Rev. B 61, 12639 (2000).

[13] E. Tsitsishvili, R. v. Baltz, and H. Kalt, *Exciton-spin relaxation in quantum dots due to spin-orbit interaction*, Phys. Rev. B. 72, 155333 (2005).

[14] P.-F. Braun, X. Marie, L. Lombez, B. Urbaszek, T. Amand, P. Renucci, V. K. Kalevich, K. V. Kavokin, O. Krebs, P. Voisin, and Y. Masumoto, *Direct Observation of the Electron Spin Relaxation Induced by Nuclei in Quantum Dots*, Phys. Rev. Lett. 94, 116601 (2005).

[15] M. Paillard, X. Marie, P. Renucci, T. Amand, A. Jbeli, and J. M. Gérard, *Spin Relaxation Quenching in Semiconductor Quantum Dots*, Phys. Rev. Lett. 86, 1634 (2001).

[16] X. Marie, A. Jbeli, M. Paillard, T. Amand, and J. Gérard, *Exciton Spin Dynamics in Self-Organized InAs/GaAs Quantum Dots*, Phys. Stats. Sol.(a) 190, 523 (2002).

[17] H. Gotoh, H. Ando, H. Kamada, A. Chavez-Pirson, and J. Temmyo, *Spin relaxation of excitons in zero-dimensional InGaAs quantum disks*, App. Phys. Lett. 72, 1341 (1998).

[18] R. M. Thompson, R. M. Stevenson, A. J. Shields, I. Farrer, C. J. Lobo, D. A. Ritchie, M. L. Leadbeater, and M. Pepper, *Single-photon emission from exciton complexes in individual quantum dots*, Phys. Rev. B 64, 201302.

[19] C. Santori, G. S. Solomon, M. Pelton, and Y. Yamamoto, *Time-resolved spectroscopy of multiexcitonic decay in an InAs quantum dot*, Phys. Rev. B 65, 073310 (2002).

[20] M. Feucker, R. Seguin, S. Rodt, A. Hoffmann, and D. Bimberg, *Decay dynamics of neutral and charged excitonic complexes in single InAs/GaAs quantum dots*, App. Phys. Lett. 92, 063116 (2008).

[21] B. Baylac, X. Marie, M. Brousseau, J. Barrau, and Y. Shekun, *Hole spin relaxation in intrinsic quantum wells*, Surface Science 326, 161 (1995).

[22] J. L. Robb, Y. Chen, A. Timmons, K. C. Hall, O. B. Shchekin, and D. G. Deppe, *Time-resolved Faraday rotation measurements of spin relaxation in InGaAs/GaAs quantum dots: Role of excess energy*, App. Phys. Lett. 90, 153118 (2007).

[23] M. Grundmann and D. Bimberg, *Theory of random population for quantum dots*, Phys. Rev. B 55, 9740 (1997).

[24] K. Roszak, V. M. Axt, T. Kuhn, and P. Machnikowski, *Exciton spin decay in quantum dots to bright and dark states*, Phys. Rev. B 76, 195324 (2007).

[25] E. Tsitsishvili, R. v. Baltz, and H. Kalt, *Exciton spin relaxation in single semiconductor quantum dots*, Phys. Rev. B 67, 205330 (2003).

[26] S. Cortez, O. Krebs, P. Voisin, and J. M. Gérard, *Polarization of the interband optical dipole in InAs/GaAs self-organized quantum dots*, Phys. Rev. B 63, 233306 (2001).

[27] Y. D. Yang, H. Lee, D. Lee, J. S. Kim, J. Y. Leem, and S. K. Noh, *The energy level spacing from InAs/GaAs quantum dots: its relation to the emission wavelength, carrier lifetime, and zero dimensionality*, J. App. Phys. 99, 096101 (2006).

[28] M. bayer, A. Kuther, A. Forchel, T. L. Reinecke, and S. N. Walck, *Fine structure of excitons in self-assembled In0.60Ga0.40As quantum dots: Zeeman-interaction and exchange energy enhancement*, PHYSICA E 7, 475 (2000).

[29] T. Takagahara, *Effects of dielectric confinement and electron-hole exchange interaction on excitonic states in semiconductor quantum dots*, Phys. Rev. B 47, 4569 (1993).

[30] R. Romestain and G. Fishman, *Excitonic wave function, correlation energy, exchange energy, and oscillator strength in a cubic quantum dot*, Phys. Rev. B 49, 1774 (1994).

[31] M. Bayer, G. Ortner, O. Stern, A. Kuther, A. A. Gorbunov, A. Forchel, P. Hawrylak, S. Fafard, K. Hinzer, T. L. Reinecke, S. N. Walck, J. P. Reithmaier, F. Klopf, and F. Schäfer, *Fine structure of neutral and charged excitons in self-assembled In(Ga)As/(Al)GaAs quantum dots*, Phys. Rev. B 65, 195315 (2002).

6. INHIBITION AND ENHANCEMENT OF SPONTANEOUS EMISSION FROM QUANTUM DOTS IN PHOTONIC CRYSTAL MEMBRANES

We study the modified spontaneous emission rates of InAs quantum dot ensembles embedded in 2D photonic crystal membranes. We observe both strong inhibition as well as enhancement of the spontaneous emission rates by varying the lattice parameter of the photonic crystal. The position of the 2D photonic band gap is in excellent agreement with LDOS calculations. The multi-exponential decay dynamics is analysed by considering the mean decay rate which is modified up to a factor of 8 by tuning the lattice parameter. By taking into account the bright-dark exciton dynamics we are able to extract the ensemble averaged LDOS which shows very strong modifications of a factor of 18. The spontaneous emission from an ensemble of quantum dots is simulated using the LDOS calculated for various positions and orientations within the photonic crystal membrane. This simulation allows for the first quantitative comparison between time-resolved measurements and a full 3D calculation of the LDOS. A strikingly good agreement between the simulations and the measurements is found.

6.1 Introduction

Control over spontaneous emission of photons in semiconductors and the ability to funnel the emission into a few selected optical modes have a huge potential in a variety of applications. Potential applications could be: i) the suppression of re-emission of captured photons in solar cells, ii) the inhibition of emission at undesired wavelengths and directions in efficient light sources, iii) reduction of threshold power and noise in lasers, iv) increased directionality and repetition rate of single-photon sources [1], and v) strong coupling in solid state cavity QED by the creation of a high-Q cavity [2, 3]. The general desire is thus to restrict the spontaneous emission to occur only in those modes necessary for device operation.

For this purpose photonic crystals offer a new and very intricate tool, allowing us to modify and control the spontaneous emission in solid state devices.

Control of spontaneous emission by photonic crystals [4, 5] and in particular photonic crystal membranes (PCMs) [6–8] have indeed resulted in great progress within the fields of single-photon sources [9–11], strong coupling in solid state cavity QED [3, 12] and miniature lasers [13–16]. The major part of the work on photonic crystals has focused entirely on the enhanced spontaneous emission emitted from defect cavities within the photonic crystals [3, 6, 7, 10, 12–16]. Only recently has attention been drawn to the properties and possible device applications of unmodified PCM, i.e., PCMs *without* defect cavities [11]. The PCMs will cause redistribution of the spontaneous emission, also known from 3D photonic crystals [17–19], and can thus be used to increase the extraction efficiency of light emitted in high index materials [20]. Moreover, it is often overlooked that the photonic crystals also cause enhancement - and not only inhibition - of the spontaneous emission: as the density of states, integrated over energy, must be conserved the rate of spontaneous emission will be enhanced at certain energies outside the band gap [21].

While the main focus in the literature has been on enhanced emission from defect cavities, the only systematic study of spontaneous emission in PCMs has been performed on quantum wells [8] for which non-radiative recombination via surface states at the edges of the air holes are known to by a serious issue [8, 22]. Moreover, the non-local character of the quantum well exciton, i.e., the relative large Bohr radius and the possibility of diffusion in the quantum well plane, results in a non-trivial average over the spatially strongly varying LDOS.

In this chapter we present the first systematic study of time-resolved spontaneous emission from quantum dots embedded in PCMs. By systematically varying the lattice parameter of the PCM, we tune the 2D photonic band gap through the emission energy of the quantum dots. We observe both enhancement and strong inhibition directly in the average decay rate which varies by a factor of ~ 8. Using our knowledge of the bright-dark exciton decay dynamics, we are moreover able to extract the ensemble averaged LDOS. From numerical calculations of the LDOS, generously provided by A. F. Koenderink [23], we obtain a suitable theoretical basis for a comparison to the measured average decay rates and we find a strikingly good quantitative agreement.

6.2 Experimental details

We have measured time-resolved spontaneous emission from ensembles of InAs quantum dots embedded in PCMs. The lattice spacing of the PCM is systematically varied while the detection energy is kept constant to probe identical subensembles of the quantum dots. This allows us to directly observe the spontaneous emission from the quantum dots as the 2D photonic band gap is tuned into and through their emission energy and all other experimental parameters are kept fixed.

Sample preparation

The InAs/GaAs quantum dots embedded in the photonic crystal membranes are nominally identical to those in the previous chapters. The wafer (NBI-178) is grown on a GaAs (100) substrate where a 2 μm thick layer of $Al_{0.7}Ga_{0.3}As$ is deposited. A GaAs slab containing the embedded InAs quantum dots are created on top of the $Al_{0.7}Ga_{0.3}As$ by the deposition of a 75 nm GaAs layer, succeeded by 2.0 monolayers of InAs, and finally the deposition of a 75 nm thick GaAs cap. A triangular lattice of air holes, defined by electron beam lithography, is dry etched into the 160 nm thick GaAs slab creating the 2D photonic crystal, see Fig. 6.1. The underlying $Al_{0.7}Ga_{0.3}As$ layer is successively removed by wet chemical etching whereby the photonic crystal membrane, of the dimensions $40 \times 40\,\mu m^2$, is left suspended in air.

We have fabricated a series of PCMs with systematically varying lattice parameter a and hole radius r. The lattice parameter is well-defined by the design and is varied between 180 nm and 470 nm in steps of 10 nm. The actual hole radii depend not only on the design but also on the lattice parameter (e-beam proximity effects), the etch process, etc. For each lattice parameter 15 membranes with varying hole radii have been fabricated. After fabrication the hole radii are determined by scanning electron microscopy (SEM).

Experimental conditions

The membranes under study are chosen to have nearly identical r/a-values within the range of $r/a = 0.313 \pm 0.006$. This value is chosen as the triangular lattice is known to exhibit a wide 2D photonic band gap for the guided modes with in-plane polarization at $r/a = 0.3$ [24]; the PCMs are thus well suited for inhibiting spontaneous emission from the ground state exciton which is in-plane polarized,

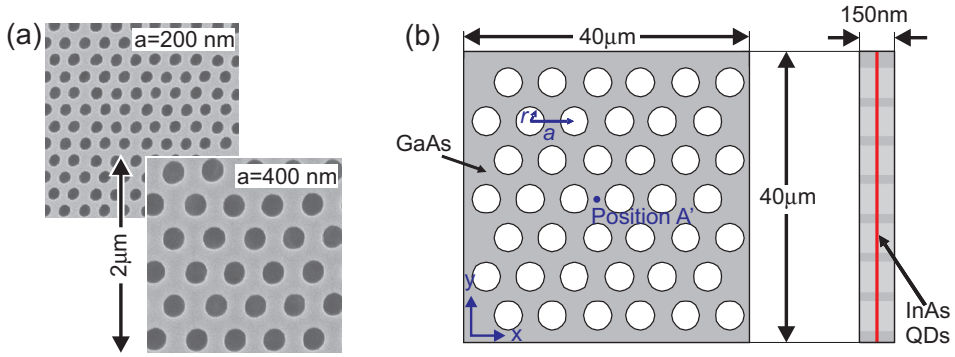

Fig. 6.1: **(a)** SEM images of two membranes showing the periodic arrangement of air holes in GaAs. Note that the shape and uniformity of the holes are superior for larger radii. **(b)** Sketch of membrane top view (left) and side view (right) indicating the dimensions. (Hole sizes are not to scale.) Position **A'** indicated by the blue dot denotes a possible position for an embedded quantum dot. LDOS calculations for this position are shown in Fig. 6.3(b).

c.f. Sec. 3.3 and [25]. To facilitate a detailed study of the slow component, we choose a repetition period of 100 ns. The excitation beam is focused to a spot having a vertical and horizontal FWHM of 47 µm and 69 µm, i.e., slightly larger than the PCMs. To ensure that only light emitted from the centre of the PCM ($d = 25$ µm) is detected, a fixed pinhole is used for spatial selection, c.f. Sec. 3.3.2. The excitation energy is 1.59 eV and the detection energy is chosen to 1.265 eV corresponding to the centre energy of the ground-state emission. At the detection energy of 1.265 eV (980 nm) the variation in lattice parameter a from 180 to 470 nm corresponds to a variation in the reduced frequency a/λ between 0.184 to 0.480. The spectral resolution is 2.6 meV. As the spatial and spectral selection reduces the number of quantum dots probed to $\sim 6 \times 10^3$, the excitation intensity is set to 6 W/cm^2 to obtain a satisfactorily signal. This correspond to the creation of ~ 15 excitons in the GaAs barrier per quantum dot.

6.3 Time-resolved measurements on quantum dots in photonic crystals

Time-resolved measurements for varying lattice parameter a are shown on a normalized scale in Fig. 6.2(a). In the limit of $a/\lambda \ll 1$ the effect of the photonic crystal will disappear as the periodicity of the structure will be small compared

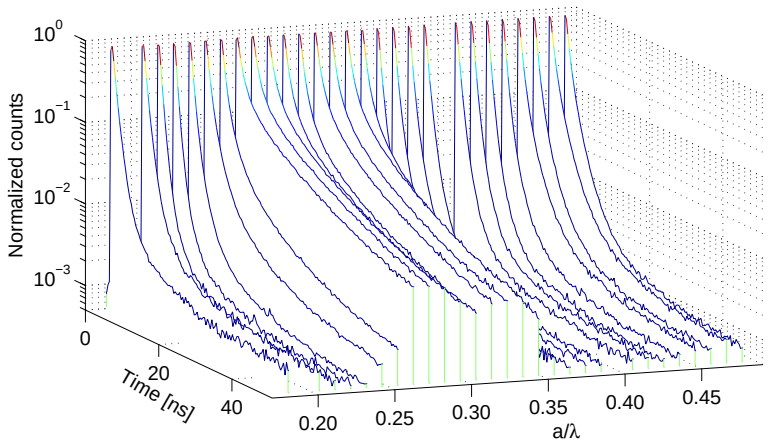

Fig. 6.2: **(a)** Normalized decay curves for the various lattice constants a. For clarity only the first 50 ns are shown. Inhibition of the spontaneous emission within the range $0.26 < a/\lambda < 0.35$ causes the decay dynamics to slow down.

to the emission wavelength. The PCM can thus be considered as a homogeneous medium which can be described by an effective refractive index. We therefore use the measurement performed on the PCM with $a = 180\,\text{nm}$ ($a/\lambda = 0.184$) as our reference. Comparing the decay curves (Fig. 6.2(a)) obtained for the different lattice parameters to the reference decay curve, a clear inhibition of the spontaneous emission is readily observed for samples in the range $0.26 < a/\lambda < 0.35$.

As in the previous measurements acquired over long time spans, the dynamics of the spontaneous emission exhibits a multi-exponential decay. From the measurements discussed in Sec. 5.6, where the LDOS for all the quantum dots in the ensemble are identical, we argue that the multi-exponential behaviour of the ensemble is due to a distribution of non-radiative or spin-flip rates and we furthermore succeed in modelling this by an average slow decay rate. The situation is, however, more complex when the quantum dot ensemble is placed in a PCM where the LDOS depends strongly on both position and orientation of the individual dipole emitter. First, we expect the decay dynamics of an ensemble to be characterized by a distribution of decay rates due to the spatial and orientational distribution of the quantum dots. Second, as the radiative decay rate is expected to be strongly inhibited, and thus comparable to or even smaller than the non-radiative decay rate, a clear separation between the radiative and non-radiative

decay rates cannot be made. As a consequence the analysis applied in Sec. 5.6 can not be used here. Instead, we choose to quantify the decay dynamics of the spontaneous emission by calculating the mean decay rate γ_{m}:

$$\frac{1}{\gamma_{\mathrm{m}}} = <\tau> = \frac{\int_0^\infty N(t)\, t\, dt}{\int_0^\infty N(t)\, dt}, \tag{6.1}$$

that is the average rate at which quantum dots in the ensemble make a transition from the excited state to the ground state. Note that the effect of variations in the LDOS is expected to be less noticeable in the mean decay rate than in the pure radiative decay rate, as the mean decay rate also includes the non-radiative decay rate which is unaffected by the LDOS. Our experimental determination of the variations in the spontaneous emission rates therefore provides a conservative estimate of the actual LDOS variation in the PCM.

6.3.1 Measuring the 2D photonic band gap

The mean decay rates are shown in Fig. 6.3(a) as a function of the reduced frequency. The decay rates are normalized to the decay rate obtained at $a/\lambda = 0.184$ which attains a value of $\gamma_{\mathrm{m}}^{\mathrm{ref}} = 0.612\,\mathrm{ns}^{-1}$. The PCM strongly affects the decay rates which show both enhancement and strong inhibition of the spontaneous emission. Within the range $0.26 < a/\lambda < 0.35$ the mean decay rates are inhibited by a factor 3.4 to 5.9 clearly showing the existence of a 2D photonic band gap. On both sides of the band gap the mean decay rates are enhanced up to 30%. There is a good qualitative agreement between the measured mean decay rates and the calculated LDOS, as exemplified in Fig. 6.3(b) showing the calculations for two dipole emitters positioned at **A'** and oriented along the x and y axes (c.f. Fig. 6.1). For the mean decay rate as well as the calculated LDOS we observe: i) enhancement on both sides of the band gap, ii) a slightly stronger enhancement on the red side than on the blue side, and iii) a decrease in the inhibition within the gap with increasing reduced frequency. While the band edges at the red side coincide perfectly, the band edges at the blue side are found to deviate by 6%.

The deviation between the measured and the calculated blue edge of the 2D photonic band gap is caused by a difference in membrane thickness d. While the mid-gap inhibition rate stays practically unaffected by reductions in the membrane thickness below $d = 400\,\mathrm{nm}$ [23], the band gap shifts towards higher frequencies and broadens slightly with decreasing thickness [26]. In the LDOS calculations a, r, and d are kept fixed while λ is varied, i.e., both r/a and d/a are thus kept

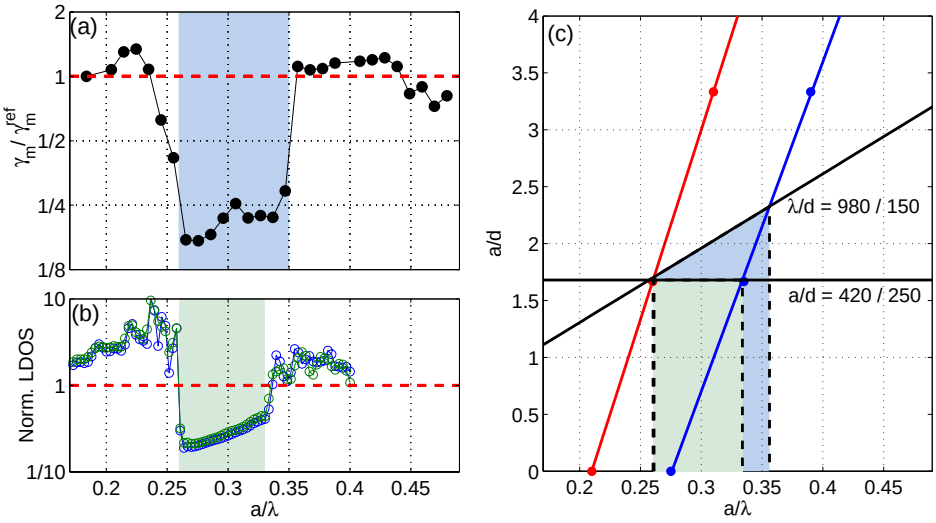

Fig. 6.3: **(a)** Mean decay rates versus reduced frequencies a/λ shown on a log-scale and normalized to the decay time of the reference. Strong inhibition of spontaneous emission is observed in the range $0.26 < a/\lambda < 0.35$, indicated by the light-blue shaded area. **(b)** Numerical calculations for a single dipole emitter at position **A'** aligned either along the x (blue) or the y axes (green), c.f. Fig.6.1(b). A 2D photonic band gap is found in the range $0.26 < a/\lambda < 0.33$ as indicated by the light-green shaded area. The numerical calculation is a courtesy of A. F. Koenderink [23]. **(c)** The edges of the band gap (solid red and blue lines) for various a/d interpolated from calculations by Andreani *et al.* [26] (solid red and blue dots). While the LDOS calculations follow the horizontal line $a/d = \frac{420\,\mathrm{nm}}{250\,\mathrm{nm}}$, the experimental measurements follow the solid line with slope $\lambda/d = \frac{980\,\mathrm{nm}}{150\,\mathrm{nm}}$. This readily explains the shift of the blue band edge.

constant. In the measurement we keep λ and d fixed, while varying a and r to keep r/a constant. This results in a reduction of the ratio d/a as the lattice parameter is increased, causing a shift of the band gap towards higher frequencies. To quantify this shift, the positions of the red and blue edges of the band gap, calculated by Andreani *et al.* [26] for $r/a = 0.3$, are shown in Fig. 6.3(c) for a/d-values of 0, 1.67, and 3.33. Since the edge positions exhibit a linear dependence on $1/d$, we perform linear interpolation to obtain the band edges for various a/d, as shown by the solid red and blue lines. The band gap is readily observed to shift towards higher frequencies and broadens as d is decreased. As the LDOS is calculated for $a/d = \frac{420\,\mathrm{nm}}{250\,\mathrm{nm}}$, shown by the horizontal line, the calculations by Andreani *et*

al. implies that the band gap in this case lies in the range $0.26 < a/\lambda < 0.33$ as indicated by the light-green shaded area. This is fully consistent with the calculations by Koenderink *et al.* In the measurements the lattice constant a is varied while keeping λ constant. This corresponds to moving along the solid line with slope $\lambda/d = \frac{980\,\mathrm{nm}}{150\,\mathrm{nm}}$. As indicated by the light-blue shaded area the band gap lies in this case in the range $0.26 < a/\lambda < 0.35$. This coincides perfectly with the position of the band gap observed in the measurements, c.f. Fig. 6.3(a). We can thus conclude that the measured 2D photonic band gap is indeed in full agreement with the numerical calculations.

As discussed in Sec. 5.6 the mean decay rate is very well defined and independent of the fitting model applied. It is thus a very strong signature of the PCM that we can observe such drastic variations without having to impose any assumptions regarding model or parameters. Moreover, the qualitative agreement between the variations in the mean decay rate of the *ensemble* and the variations in the LDOS calculated for a *single* position is surprisingly good. In Sec. 6.4 we will elaborate on how the experiment compares to quantitative theory.

6.3.2 Determining the ensemble averaged LDOS in PCMs

To make a more quantitative comparison of the level of inhibition / enhancement, we need to take into account both the interplay between the dark and bright quantum dot states as well as the ensemble nature of the experiment. The implications of this will be discuss in this section.

Internal bright-dark dynamics

In the 2D photonic band gap the LDOS is expected to attain values between 1/2 to 1/20 depending on the position and orientation of the in-plane dipole emitter, c.f. Ref [23]. The decay rate will additionally depend strongly on the properties of the emitter, i.e., the quantum efficiency and the interplay between the fine structure levels. Here we will consider three cases: i) an ideal two-level emitter with a quantum efficiency of 100%, ii) an ideal two-level emitter with a quantum efficiency of 95%, and iii) a quantum dot with both bright and dark states. In the latter case we employ the bi-exponential model described in Sec. 2.2.4. The approximation of $\gamma_{\mathrm{db}}, \gamma_{\mathrm{bd}} \ll \gamma_{\mathrm{b}} - \gamma_{\mathrm{d}}$ is however not implemented as the radiative decay rate can be strongly inhibited whereby the approximation is not valid. The parameters used in the bi-exponential model are obtained from the measurements presented in Sec. 5.6 and given in the figure caption of Fig. 6.4. To compare

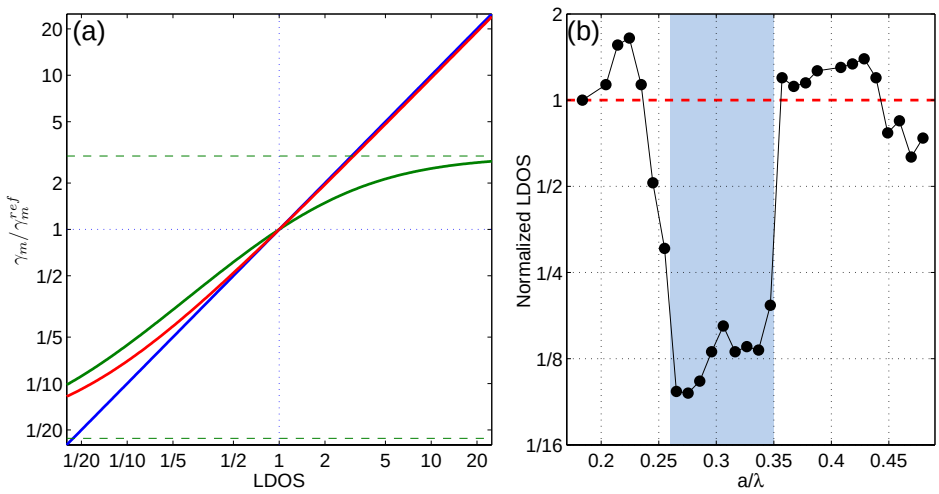

Fig. 6.4: **(a)** The normalized mean decay rate calculated for i) an ideal two-level emitter with $QE = 1$ (solid blue line), ii) an ideal two-level emitter with with $QE = 0.95$ (solid red line), and iii) taking into account the bright and dark excitons (solid green line). In accordance with the excitation degree of 15 excitons per quantum dot the following parameters are used: $\gamma_{\mathrm{rad}} = 1.3\,\mathrm{ns}^{-1}$, $\gamma_{\mathrm{bd}} = \gamma_{\mathrm{db}} = 35\,\mu\mathrm{s}^{-1}$, $\gamma^{\mathrm{b}}_{\mathrm{nrad}} = \gamma^{\mathrm{d}}_{\mathrm{nrad}} = 25\,\mu\mathrm{s}^{-1}$, $\rho_{\mathrm{b}}(0) = 0.95$, and $\rho_{\mathrm{d}}(0) = 0.05$. **(b)** The normalized LDOS can be obtained from the unambiguous relation between the normalized mean decay rate and the LDOS shown in (a).

the three cases the mean decay rates, calculated as a function of the LDOS, are normalized to the mean decay rate for a LDOS identical to unity. The comparison is shown in Fig. 6.4(a).

- In the trivial case of an ideal emitter with $QE = 100\%$ (blue line) there is a linear relation between the measured rate and the LDOS.
- If the QE is not unity (red line) the non-radiative decay rate sets a lower bound for the decay rate, i.e., when the spontaneous emission is completely inhibited the emitter can decay only by non-radiative decay. The normalized decay rate will thus approach $(1 - QE)$ as the LDOS is reduced below unity, while for increasing LDOS the radiative decay rate will dominate and a (nearly) linear relation can be found between the LDOS and the mean decay rate.
- In the third case, which includes the interplay between the bright and dark

excitons, the dependence of the mean decay rate on the LDOS is always sub-linear (green line). In the lower limit the normalized mean decay rate approaches $(1-QE)$. In the upper limit the mean decay rate saturates as the total number of photon counts in both the fast and in the slow components are proportional to the radiative decay rate γ_{rad}.

It is important to note that the interplay between the bright and dark states leads to a sub-linear dependence of the normalized mean decay rate on the LDOS. We can thus safely state that observed changes in the mean decay rate are caused by even larger variations in the LDOS. In relation to the measured variations in the normalized mean decay rate from 0.17 to 1.33(Fig. 6.3(a)), this means that the spontaneous emission inside the 2D photonic band gap is inhibited by more than a factor 5.9 and that the emission on the red edge is enhanced by more than 33%.

However, as both the normalized mean decay rate and LDOS are monotonic functions, their unambiguous relation allows for a more quantitative analysis, i.e., a determination of the ensemble averaged LDOS. Such an analysis demands knowledge of the rates governing the decay and the initial populations which we have obtained in Chapter 5. In accordance with the excitation degree of 15 excitons per quantum dot, the following parameters are used: the radiative decay rate $\gamma_{\mathrm{rad}} = 1.3\,\mathrm{ns}^{-1}$, the spin-flip rate $\gamma_{\mathrm{bd}} = 35\,\mu\mathrm{s}^{-1}$, the non-radiative decay rate $\gamma_{\mathrm{nrad}} = 25\,\mu\mathrm{s}^{-1}$, and the initial population for the bright and dark states $\rho_{\mathrm{b}}(0) = 0.95$ and $\rho_{\mathrm{d}}(0) = 0.05$ respectively. The ensemble averaged LDOS obtained with these parameters and normalized to the ensemble averaged LDOS obtained at $a/\lambda = 0.184$ is shown in Fig. 6.4(b) as a function of the reduced frequency. We find that inside the 2D band gap the LDOS is suppressed by at least a factor 5.2 and at most a factor of 10.6, while an enhancement by a factor of 1.7 occurs on the the red side of the 2D photonic band gap.

6.4 Quantitative comparison to LDOS calculations

The ensemble character of the derived LDOS (Fig. 6.4(b)) must be considered in order to make a quantitative comparison to numerical calculations; as we are measuring on ensembles, only ensemble averaged properties can be extracted from the measurements. The LDOS, to which the individual quantum dots couple, will depend strongly on their exact position and the orientation of their transition dipole moments and must thus be calculated for each possible position and orientation.

The spontaneous emission from the ensemble can then be simulated by summing the decay curves (Eq. (2.24)) from a large number of emitters placed at different locations $\mathbf{r}$ and with different orientations Θ:

$$N(t) = \sum_{\mathbf{r},\Theta} \eta(\mathbf{r},\Theta)\gamma_{\mathrm{rad}}(\mathbf{r},\Theta) M \rho_{\mathrm{b}}(\gamma_{\mathrm{rad}}(\mathbf{r},\Theta),t). \tag{6.2}$$

Here the position and orientation dependence of the collection efficiency η, the radiative decay rate γ_{rad}, and the bright exciton population ρ_{b} are explicitly denoted. A theoretical basis suitable for a direct comparison with the measured mean decay rates can successively be obtained by calculating the first moment (Eq. (6.1)) of Eq. (6.2). However, to simulate the overall decay dynamics it is necessary to consider: i) the orientational properties of the transition dipole, i.e., is Θ fixed at a given orientation or does it 'diffuse' and thus performs an effective average over the LDOS, and ii) the dependence of the collection efficiency on $\mathbf{r}$ and Θ. These two points of consideration will be discussed below.

Dipole orientation

The time-resolved measurements on quantum dot ensembles near a dielectric interface, c.f. Sec. 3.3, and the clear appearance of a 2D photonic band gap which coincides with the calculated in-plane 2D photonic band gap, allow us to conclude that the ground-state emission is polarized in the plane of the membrane. The question which remains is whether the transition dipoles can be considered to stay at fixed in-plane orientations within the exciton lifetime or if they 'diffuse' around in the plane. The latter could be caused by a high bright-bright spin flip rate as light emitted from the two bright states will be polarized along the two orthogonal principal axes of the quantum dot [27]. In the limit of a fast bright-bright spin flip, the quantum dot will effectively couple to the average value of the LDOS projected onto the two principal axes. This will smear out the extrema of the LDOS, in particular in the 2D photonic band gap where the LDOS projected on two orthogonal axes in general is found to be anti-correlated, c.f. Fig 1.5 in Ref. [23].

From measurements performed on InAs/GaAs quantum dots to determine the bright-bright spin-flip rates there are reports of both very slow spin-flip rates ($< 50\,\mu\mathrm{s}^{-1}$) [28] as well as very fast ($\geq 10\,\mathrm{ns}^{-1}$) spin-flip rates for some quantum dots [29]. Based on the LDOS calculations a fast bright-bright spin-flip will reduce the maximum inhibition inside the band gap to a factor of ~ 6. However, from measurements on single dots on the same wafer we have obtained decay rates as

low as $0.05\,\mathrm{ns}^{-1}$, i.e., an inhibition by a factor of ~ 20. Such low decay rates demonstrate that the fast bright-bright spin-flip is not occurring here. In the following calculations we will thus assume that the orientation of the transition dipole moment remains fixed within the exciton lifetime.

Collection efficiency and radiation pattern of single quantum dots

The radiation pattern of the individual quantum dots depends on the angular symmetry of the LDOS projections, i.e., strong inhibition of spontaneous emission in some directions causes not only reduction in the emission rate but also spatial redistribution of the spontaneous emission. In fact PCMs have been proposed as a mean to enhance the poor extraction efficiency of light emitted in semiconductor structures [20]. To understand in details how the extraction efficiency of the individual quantum dots will depend on its position and orientation the far-field emission patterns must be calculated for each possible position and orientation. This can be achieved by finite difference time domain calculations and a successive near-to-far-field transformation following the approach of, e.g., Taflove *et al.* [30]. This is, however, far from a trivial task and we will not pursue it here.

In a more feasible approach, the collection efficiency can be approximated as follows. The radiative modes, into which the spontaneous emission is emitted, are divided in two groups: the modes which are confined and propagate in the slab and the modes which leak out of the slab. Correspondingly, the radiative decay rate can be expressed as the sum of the decay rates into the two groups of modes: $\gamma_{\mathrm{rad}} = \gamma_{\mathrm{slab}} + \gamma_{\mathrm{leak}}$. While the 2D photonic crystal strongly affects the decay rate into the slab $\gamma_{\mathrm{slab}}(\mathbf{r}, \Theta)$, it is assumed that the rate into the leaky modes γ_{leak} is completely unaffected by the photonic crystal [8, 31]. The collection efficiency is in this case given by the ratio of the leaky rate to the radiative rate:

$$\eta(\mathbf{r}, \Theta) \simeq \xi \frac{\gamma_{\mathrm{leak}}}{\gamma_{\mathrm{leak}} + \gamma_{\mathrm{slab}}(\mathbf{r}, \Theta)} = \xi \frac{\gamma_{\mathrm{leak}}}{\gamma_{\mathrm{rad}}(\mathbf{r}, \Theta)}, \tag{6.3}$$

where ξ denotes the fraction of the leaky modes which are emitted into the numerical aperture of the collection optics. In this approach the collection efficiency is thus found to be inversely proportional to the decay rate, i.e., if the spontaneous emission is strongly inhibited in the plane by the 2D photonic crystal the emission is redistributed and emitted into the leaky modes. The time-integrated luminescence from an excited quantum dot is correspondingly given by

$$N(\mathbf{r}, \Theta) \propto \xi \frac{\gamma_{\mathrm{leak}}}{\gamma_{\mathrm{rad}}(\mathbf{r}, \Theta)} QE \propto \frac{QE}{\gamma_{\mathrm{rad}}(\mathbf{r}, \Theta)}. \tag{6.4}$$

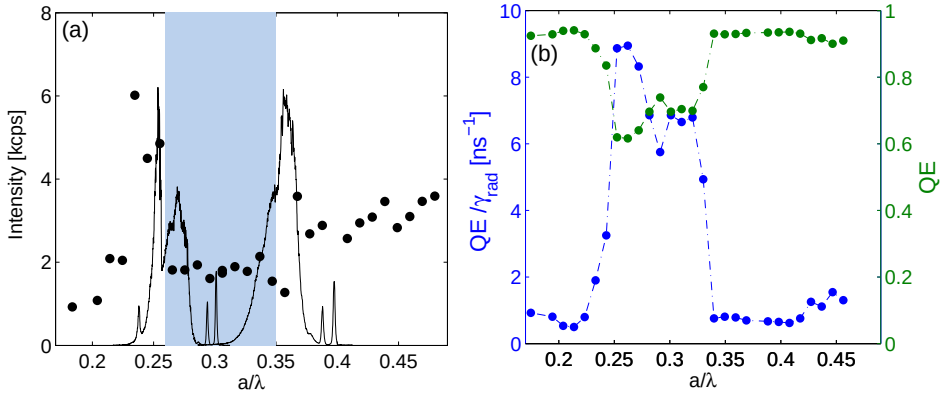

Fig. 6.5: **(a)** Intensity versus reduced frequency (solid dots). No signs of redistributed spontaneous emission are observed; on the contrary a reduction of the intensity is observed inside the band gap. The two spectra at the band edges (solid curves) also display suppression for the emission energies within the band gap. **(b)** Expected intensity versus reduced frequency in the case of redistribution (blue dots, left axis) and no redistribution (green dots, right axis).

Measurements on single quantum dots [11, 31] and on a quantum well [8] placed in 2D photonic crystals have shown an increase in time-integrated luminescence for the emission energies within the band gap. However, we do not observe such an effect in our measurements. In Fig 6.5(a) the measured intensities, which are shown as a function of the reduced frequency, display a reduction of the intensity within the 2D band gap. We note that comparing absolute intensity measurements among different PCM can be difficult as the sample must be repositioned for each membrane and moreover the pump beam suffers different Bragg reflection on the different PCMs due to the variation in lattice parameter [32]. The observed reduction in the time-integrated intensity is confirmed by the acquired spectra, shown in Fig. 6.5(b). The two spectra, acquired at the edges of the band gap, exhibit a clear suppression of the luminescence for energies inside the band gap. This suggest that the reduced time-integrated luminescence within the 2D photonic band gap is not only due to different effective pumping caused by mis-alignments or variation in the reflection of the pump beam. The expected variations in time-integrated ensemble luminescence, given by Eq. (6.4), can by calculated from the ensemble averaged LDOS shown in Fig. 6.4. These variations are shown together with the calculated quantum efficiency in Fig. 6.5(a). While there are no simi-

larities between the time-integrated measurements and the expected emission in the presence of pronounced redistribution ($\propto \frac{QE}{\gamma_{rad}}$) there seems to be a qualitative agreement between the measurements and the variation in the QE. If no or moderate redistribution of the emission takes place we expect the time-integrated luminescence to be proportional to the QE. A possible explanation for the discrepancy between our measurements and those reported in Refs. [11, 31] could be the different size of the numerical apertures in the experimental setups: if redistribution of the emission mainly occurs into modes which leave the membrane at high angles, a small aperture will not collect those modes, while a high numerical aperture will. In Refs. [11, 31] a high numerical aperture of 0.8 is used.

Calculations of the ensemble averaged decay rates

Based on the LDOS calculations and the bi-exponential model (c.f. Sec. 2.2.4) we simulate the spontaneous emission arising from an ensemble of quantum dots placed inside the PCM. The summation over different positions and orientations includes two orthogonal in-plane dipole orientations and 7 spatial positions[1]. The parameters used to model the bi-exponential decay are those already given in Sec. 6.3.2.

As we do not observe indications of a redistribution of the spontaneous emission, the calculations are performed both for the case of no redistribution, for which the ensemble luminescence is given as

$$N(t) \propto \sum_{\mathbf{r},\Theta} \gamma_{\mathrm{rad}}(\mathbf{r},\Theta)\rho_{\mathrm{b}}(\mathbf{r},\Theta,t), \tag{6.5}$$

and in the case of redistribution, for which the ensemble luminescence is given as

$$N(t) \propto \sum_{\mathbf{r},\Theta} \rho_{\mathrm{b}}(\mathbf{r},\Theta,t). \tag{6.6}$$

The simulated spontaneous emission calculated for the ensemble in both cases is shown in Fig. 6.6 for 3 different reduced frequencies: below ($a/\lambda = 0.204$), inside ($a/\lambda = 0.296$), and above the 2D photonic band gap ($a/\lambda = 0.388$). The simulated emission has been scaled and added a background, corresponding to the measured values, to facilitate a direct comparison to the measurement shown along the

[1] The LDOS is calculated for the three orthogonal dipole orientations and at 16 different positions along the trajectory of the irreducible unit cell [23]. However, as we only need to consider in-plane polarization and as our quantum dots are located outside the air holes the summation is reduced to include only 14 of the 48 different terms.

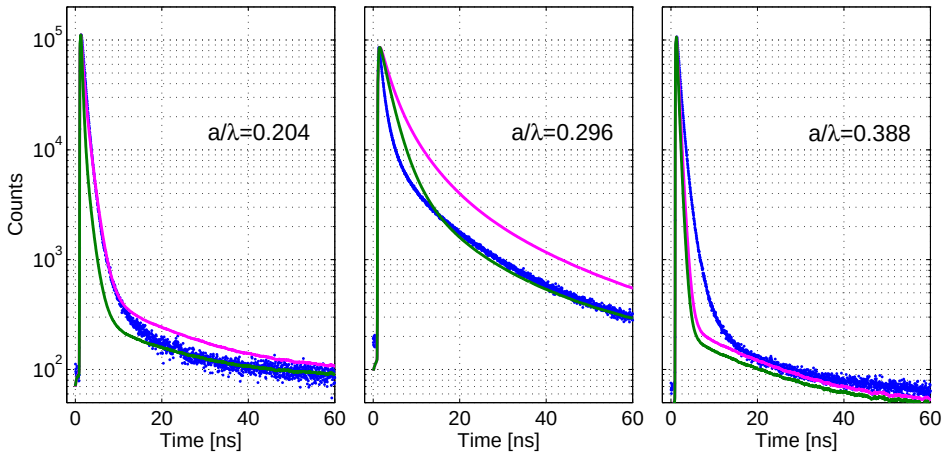

Fig. 6.6: The simulated ensemble emission in case of redistribution (magenta) and no redistribution (green) for 3 different reduced frequencies: below ($a/\lambda = 0.204$), inside ($a/\lambda = 0.296$), and above ($a/\lambda = 0.388$) the 2D photonic band gap. The simulations have been scaled and added a background corresponding to the respective measurements shown by the blue dots.

simulated data. The overall trends observed in the measured data are qualitatively well represented by the simulations. Inside the band gap the slow decay rates and in particular the amplitude of the slow components are dominating, while the slow components are several orders of magnitude weaker than the fast component outside the band gap. However, just as in Sec. 5.6 the simulated data are not capable of modelling the smooth transition from the fast to the slow component observed in the time-resolved measurements precisely. This is most evident outside the band gap where the fast radiative decay rate can be clearly separated from the slow non-radiative decay rate. Again, we suggest that this discrepancy is due to a distribution of the non-radiative or the spin-flip rates. In case of no redistribution of spontaneous emission, the fast decaying components will be weighted stronger than the slowly decaying components. This appears as a suppression of the slow components in simulated emission (green lines) when compared to the simulations describing the case of redistributed spontaneous emission. Neither of the two cases can be argued to obtain a better overall agreement with the time-resolved measurements than the other. We do therefore not find support for rejecting either of the two cases.

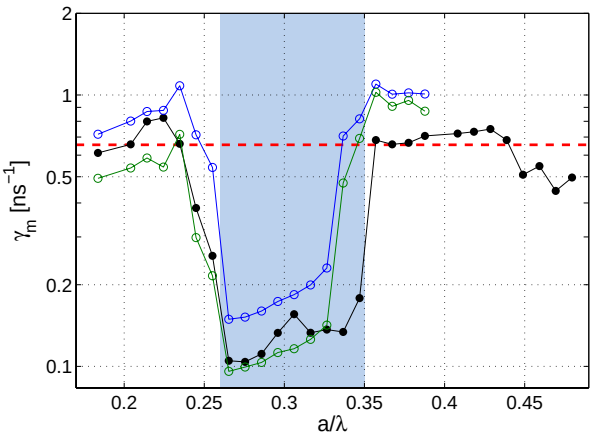

Fig. 6.7: The mean decay rate as a function of the reduced frequency: measurement (black solid dots), simulation without redistribution (open blue circles), and simulation with redistribution (open green circles).

Despite the fact that the simulated decay curves do not perfectly model the time-resolved measurements, we do achieve a remarkable agreement between the mean decay rates obtained from the simulations and those measured. All data are shown in Fig. 6.7. As we simulate the mean decay rate, a direct comparison is possible without normalising the data. The dashed red line indicates the averaged decay rate obtained away from the PCM, that is from quantum dots placed in a GaAs slab. The measured rates vary between $0.10\,\mathrm{ns}^{-1}$ and $0.82\,\mathrm{ns}^{-1}$ corresponding to a variation by a factor of 7.9. This is very well matched by the simulations of the redistributed spontaneous emission resulting in variations between $0.10\,\mathrm{ns}^{-1}$ and $1.02\,\mathrm{ns}^{-1}$ (a factor of 10.7), while the non-redistributed spontaneous emission leads to a slightly weaker variation by a factor of 7.4, i.e., between $0.15\,\mathrm{ns}^{-1}$ to $1.10\,\mathrm{ns}^{-1}$. This successful comparison of the ensemble decay dynamics to numerical calculations of the strongly position and orientation dependent LDOS is, to the best of our knowledge, the first successful quantitative comparison between experiment and full 3D LDOS calculations.

6.5 Conclusion

We have studied the time-resolved emission from quantum dots embedded in PCMs while systematically varying the lattice parameter. The mean decay rate is found to vary strongly by a factor of ~ 8. Strong inhibition of the spontaneous emission is observed within the 2D photonic band gap which is found in the range $0.26 < a/\lambda < 0.35$ in full agreement with numerical calculations by Koenderink *et al.* [23]. Using the knowledge gained earlier regarding the interplay between the bright and dark exciton states, we are able to conclude that the variations in the ensemble averaged LDOS are even stronger than the variations in the mean decay rate. We extract this ensemble averaged LDOS, which is found to vary by more than a factor of 18. Simulating the spontaneous emission from an ensemble of quantum dots placed in the PCM, we obtain a simulated mean decay rate, which is found to agree remarkably well with the measured mean decay rates. We have thus succeeded to make a full quantitative comparison between the numerically calculated LDOS and the measured ensemble decay dynamics.

References to Chapter 6

[1] J. Kim, O. Benson, H. Kan, and Y. Yamamoto, *A single-photon turnstile device*, Nature 397, 500 (1999).

[2] J. P. Reithmaier, G. Sęk, A. Löffler, C. Hofmann, S. Kuhn, S. Reitzenstein, L. V. Keldysh, V. D. Kulakovskii, T. L. Reinecke, and A. Forchel, *Strong coupling in a single quantum dot-semiconductor microcavity system*, Nature 432, 197 (2004).

[3] T. Yoshie, A. Scherer, J. Hendrickson, G. Khitrova, H. M. Gibbs, G. Rupper, C. Ell, O. B. Shchekin, and D. G. Deppe, *Vacuum Rabi splitting with a single quantum dot in a photonic crystal nanocavity*, Nature 432, 200 (2004).

[4] P. Lodahl, A. F. van Driel, I. S. Nikolaev, A. Irman, K. Overgaag, D. Vanmaekelbergh, and W. L. Vos, *Controlling the dynamics of spontaneous emission from quantum dots by photonic crystals*, Nature 430, 654 (2004).

[5] I. S. Nikolaev, P. Lodahl, A. F. van Driel, A. F. Koenderink, and W. L. Vos, *Strongly nonexponential time-resolved fluorescence of quantum-dot ensembles in three-dimensional photonic crystals*, Phys. Rev. B 75, 115302 (2007).

[6] A. Kress, F. Hofbauer, N. Reinelt, M. Kaniber, H. J. Krenner, R. Meyer, G. Böhm, and J. J. Finley, *Manipulation of the spontaneous emission dynamics of quantum dots in two-dimensional photonic crystals*, Phys. Rev. B 71, 241304 (2005).

[7] D. Englund, D. Fattal, E. Waks, G. Solomon, B. Zhang, T. Nakaoka, Y. Arakawa, Y. Yamamoto, and J. Vučković, *Controlling the Spontaneous Emission Rate of Single Quantum Dots in a Two-Dimensional Photonic Crystal*, Phys. Rev. Lett. 95, 013904 (2005).

[8] M. Fujita, S. Takahashi, Y. Tanaka, T. Asano, and S. Noda, *Simultaneous Inhibition and Redistribution of Spontaneous Light Emission in Photonic Crystals*, Science 308, 1296 (2005).

[9] J. Vučković and Y. Yamamoto, *Photonic crystal microcavities for cavity quantum electrodynamics with a single quantum dot*, App. Phys. Lett. 82, 2374 (2003).

[10] W.-H. Chang, W.-Y. Chen, H.-S. Chang, T.-P. Hsieh, J.-I. Chyi, and T.-M. Hsu, *Efficient Single-Photon Sources Based on Low-Density Quantum Dots in Photonic-Crystal Nanocavities*, Phys. Rev. Lett. 96, 117401 (2006).

[11] M. Kaniber, A. Laucht, T. Hürlimann, M. Bichler, R. Meyer, M.-C. Amann, and J. J. Finley, *Highly efficient single-photon emission from single quantum dots within a two-dimensional photonic band-gap*, Phys. Rev. B 77, 073312 (2008).

[12] K. Hennessy, A. Badolato, D. Gerace, M. Atatüre, S. Gulde, S. Fält, E. L. Hu, and A. Imamoğlu, *Quantum nature of a strongly coupled single quantum dot-cavity system*, Nature 445, 896 (2007).

[13] O. Painter, R. K. Lee, A. Scherer, A. Yariv, J. D. O'Brien, P. D. Dapkus, and I. Kim, *Two-Dimensional Photonic Band-Gap Defect Mode Laser*, Science 284, 1819 (1999).

[14] H. Y. Ryu, M. Notomi, E. Kuramoti, and T. Segawa, *Large spontaneous emission factor (> 0.1) in the photonic crystal monopole-mode laser*, App. Phys. Lett. 84, 1067 (2004).

[15] H. G. Park, S. H. Kim, S. H. Kwon, Y. G. Ju, J. K. Yang, J. H. Baek, S. B. Kim, and Y. H. Lee, *Electrically Driven Single-Cell Photonic Crystal Laser*, Science 305, 1444 (2004).

[16] S. Strauf, K. Hennessy, M. T. Rakher, Y.-S. Choi, A. Badolato, L. C. Andreani, E. L. Hu, P. M. Petroff, and D. Bouwmeester, *Self-Tuned Quantum Dot Gain in Photonic Crystal Lasers*, Phys. Rev. Lett. 96, 127404 (2006).

[17] A. F. Koenderink, L. Bechger, H. P. Schriemer, A. Lagendijk, and W. L. Vos, *Broadband Fivefold Reduction of Vacuum Fluctuations Probed by Dyes in Photonic Crystals*, Phys. Rev. Lett. 88, 143903 (2002).

[18] I. S. Nikolaev, P. Lodahl, and W. L. Vos, *Quantitative analysis of directional spontaneous emission spectra from light sources in photonic crystals*, Phys. Rev. A 71, 053813 (2005).

[19] L. Bechger, P. Lodahl, and W. Vos, *Directional Fluorescence Spectra of Laser Dye in Opal and Inverse Opal Photonic Crystals*, J. Phys. Chem. B 109, 9980 (2005).

[20] S. Fan, P. R. Villeneuve, J. D. Joannopoulos, and E. F. Schubert, *High Extraction Efficiency of Spontaneous Emission from Slabs of Photonic Crystals*, Phys. Rev. Lett. 78, 3294 (1997).

[21] S. M. Barnett and R. Loudon, *Sum Rule for Modified Spontaneous Emission Rates*, Phys. Rev. Lett. 77, 2444 (1996).

[22] H. Altug, D. Englund, and J. Vučković, *Ultrafast photonic crystal nanocavity laser*, Nature Physics 2, 484 (2006).

[23] A. F. Koenderink, M. Kafesaki, C. M. Soukoulis, and V. Sandoghdar, *Spontaneous emission rates of dipoles in photonic crystal membranes*, J. Opt. Soc. Am. B 23, 1196 (2006).

[24] J. D. Joannopoulos, R. D. Meade, and J. N. Winn, *Photonic Crystals - Molding the Flow of Light*, Princeton University Press, Princeton NJ (1995).

[25] S. Cortez, O. Krebs, P. Voisin, and J. M. Gérard, *Polarization of the interband optical dipole in InAs/GaAs self-organized quantum dots*, Phys. Rev. B 63, 233306 (2001).

[26] L. C. Andreani and M. Agio, *Photonic Bands and Gap Maps in a Photonic Crystal Slab*, J. Quantum Elec. 38, 891 (2002).

[27] M. Bayer, G. Ortner, O. Stern, A. Kuther, A. A. Gorbunov, A. Forchel, P. Hawrylak, S. Fafard, K. Hinzer, T. L. Reinecke, S. N. Walck, J. P. Reithmaier, F. Klopf, and F. Schäfer, *Fine structure of neutral and charged excitons in self-assembled In(Ga)As/(Al)GaAs quantum dots*, Phys. Rev. B 65, 195315 (2002).

[28] M. Paillard, X. Marie, P. Renucci, T. Amand, A. Jbeli, and J. M. Gérard, *Spin Relaxation Quenching in Semiconductor Quantum Dots*, Phys. Rev. Lett. 86, 1634 (2001).

[29] I. Favero, G. Cassabois, C. Voisin, C. Delalande, P. Roussignol, R. Ferreira, C. Couteau, J. P. Poizat, and J. M. Gérard, *Fast exciton spin relaxation in single quantum dots*, Phys. Rev. B 71, 233304 (2005).

[30] A. Taflove and S. C. Hagness, *Computational Electrodynamics: The Finite-Difference Time-Domain Method*, Artech House Publishers, Boston, 3rd edition (2005).

[31] M. Kaniber, A. Kress, A. Laucht, M. Bichler, R. Meyer, M.-C. Amann, and J. J. Finley, *Efficient spatial redistribution of quantum dot spontaneous emission from two-dimensional photonic crystals*, App. Phys. Lett. 91, 061106 (2007).

[32] V. N. Astratov, J. S. Culshaw, R. M. Stevenson, D. M. Whittaker, M. S. Skolnick, T. F. Krauss, and R. M. de la Rue, *Resonant coupling of near-infrared radiation to photonic band structure waveguides*, J. Lightwave Tech. 17, 2050 (1999).

7. SUMMARY AND OUTLOOK

7.1 Summary

In this thesis we present and discuss the decay dynamics of spontaneous emission from quantum dots embedded in nanophotonic structures. The outcome of the research is presented in the Chapters 3 to 6 and the main results and conclusions are emphasized here.

Energy dependence of the oscillator strength and quantum efficiency of InAs quantum dots measured by a modified local density of optical states

We present time-resolved measurement acquired from InAs quantum dot ensembles placed in the close vicinity of a dielectric interface. The decay rate of the spontaneous emission as a function of distance to the interface is excellently modelled by theory. This allows for an accurate determination of the radiative and non-radiative decay rates and thus an accurate determination of the oscillator strength and quantum efficiency. The energy dependence of the oscillator strength and quantum efficiency is determined by acquiring the time-resolved measurements for 6 different energies. Both properties are found to decrease with increasing emission energy (decreasing quantum dot size). From these measurements we conclude that the optical properties of large quantum dots, emitting at low energies, are superior and that large quantum dots thus are most suited as nanophotonic light sources. The measurements are also acquired under stronger excitation intensity, for which we observe a reduction in the quantum efficiency.

We report a series of measurements on colloidal CdSe/ZnS quantum dots near as silver-coated interface. The differences between the self-assembled and the colloidal quantum dots are summarized, and the interpretation of the intrinsically multi-exponential decay curves from colloidal quantum dots is discussed. Despite the complexity of the decay dynamics, the measured decay rates are well modelled by taking into account the two-dimensional character of the dipole.

Measuring the overlap of the electron and hole wavefunctions

We evaluate the transition matrix element for self-assembled InAs quantum dots, whereby a relation between the oscillator strength and the overlap of the electron and hole wavefunctions is established. Using this relation we obtain the wavefunction overlap from the measurements presented in Chapter 3. The overlap is found to decrease with increasing emission energy (decreasing quantum dot size). The experimental findings are supported by calculations of the wavefunction overlap implemented in the effective-mass approximation. The calculation shows a reduction in the wavefunction overlap as the quantum dot size is reduced. This reduction stems from the different masses of the electron and hole which results in a different sensitivity of the electron and hole wavefunctions on the quantum dot size.

The energy dependence of the wavefunction overlap in colloidal CdSe/ZnS quantum dots is also calculated and compared to the case of InAs quantum dots. For colloidal quantum dots the overlap shows no dependence on quantum dot size, thereby pinpointing a striking difference between colloidal and self-assembled quantum dots. The difference readily explains the different energy dependence of the radiative decay rate which is reported for colloidal quantum dots in Ref. [1].

Decay dynamics of bright and dark excitons

The decay dynamics of quantum dot ensembles is studied under different excitation conditions, different emission energies, and for various distances to a dielectric interface. The time-resolved emission is analysed in a model which takes into account the bright and dark excitons and their internal dynamics, allowing for a determination of the spin-flip rate. We compare data acquired over 13 ns and 200 ns and conclude that we are able to obtain the spin-flip rates from data acquired over short time spans. However, the rates acquired over 13 ns must be corrected to compensate for the strongly weighted fast rates. The data acquired over 200 ns reveal that the spontaneous emission exhibit a multi-exponential decay. We suggest that this is caused by a distribution of non-radiative and/or spin-flip rates within the quantum dot ensemble.

From the measurements obtained under various excitation intensities, the spin-flip rate is found to increase with increasing intensity. The spin-flip rate is also strongly dependent on the excitation energy and the possible causes are discussed in details. Analyzing the measurements presented in Chapter 3 in the more involved model, the spin-flip rate's dependence on quantum dot energy is obtained.

The observed dependence is discussed in the context of two different mechanisms proposed to be the cause of the spin-flip. Our measurements lend qualitative support to a spin flip caused by virtual phonon scattering [2]. A surprising structural dependence of the spin-flip rates is found from the same measurements.

The temperature dependence of the spin-flip rate is also measured and found to increase with increasing temperature. This is in overall agreement with the spin-flip rate being phonon-mediated and thus proportional to the density of acoustic phonons.

Inhibition and enhancement of spontaneous emission from quantum dots in photonic crystals

We have performed a study of the spontaneous emission from quantum dots embedded in photonic crystal membranes while systematically varying the lattice parameter. Strong inhibition of the mean decay rate is observed for emission frequencies within the 2D photonic band gap, while enhancement is observed on both sides of the band gap. The measured width and position of the band gap is in excellent agreement with theory. Due to the bright-dark interplay, the directly measured variation in the mean decay rates is a conservative measure of the variations in the local density of optical states. We discuss how to perform a quantitative comparison between local density of states calculations and measurements. Using the knowledge of the quantum dot decay dynamics obtained in Chapters 3 and 5, we model the mean decay rate for an ensemble of quantum dots embedded in a photonic crystal membrane. The modelled mean decay rates are found to agree remarkably well with the measured mean decay rates. This is, to the best of our knowledge, the first successful comparison between experiment and a full 3D calculation of the local density of optical states.

7.2 Outlook

To further improve the understanding of the light-emitter coupling in photonic crystals, the work presented here could be continued on several fronts:

Numerical calculations of the emission patterns

A theoretical study of the redistribution of spontaneous emission from quantum dots within the photonic crystal membrane would allow for the correct weighting of the individual components in the modelled ensemble emission. The calculations

should be performed for several positions and orientations of the dipole emitter. Such a study would benefit from similar experimental studies, i.e., measurements of spontaneous emission from single quantum dots, from which the decay rate could be related to the intensity, hopefully in agreement with the numerical calculations.

Time-resolved measurements of spontaneous emission from single quantum dots

An experimental study of time-resolved measurements on single quantum dots within the photonic crystal membrane. From a sufficiently large number of data points, a distribution of decay rates could be obtained and directly compared to the calculations of the local density of optical states. In contrast to 3D structures, photonic crystal membranes are well suited for such experiments as the individual quantum dots can be addressed from above the membrane.

Suppression of dark exciton creation in doped structures

By incorporation of a highly n-doped semiconductor layer near the quantum dot layer, the quantum dots can be charged with a single electron. This will suppress the formation of dark excitons, as the introduction of an exciton in the quantum dot will result in the formation of a trion (a charged exciton). The trion has no fine structure [3] and the spontaneous emission decays thus single exponentially [4,5].

Embedding such a layer of pre-charged quantum dots in the photonic crystal membrane should facilitate a more simple analysis of the measured spontaneous emission as the individual quantum dots are expected to decay single-exponentially. The trion may suffer from a large non-radiative decay, and it is thus necessary to determine the quantum efficiency of the quantum dot trions before a comparison between experiment and theory can be performed.

References to Chapter 7

[1] A. F. van Driel, G. Allan, C. Delerue, P. Lodahl, W. L. Vos, and D. Vanmaekelbergh, *Frequency-Dependent Spontaneous Emission Rate from CdSe and CdTe Nanocrystals: Influence of Dark States*, Phys. Rev. Lett. 95, 236804 (2005).

[2] K. Gündoğdu, K. C. Hall, E. J. Koerperick, C. E. Pryor, M. E. Flatté, T. F. Boggess, O. B. Shchekin, and D. G. Deppe, *Electron and hole spin dynamics in semiconductor quantum dots*, App. Phys. Lett. 86, 113111 (2005).

[3] A. Högele, S. Seidl, M. Kroner, K. Karrai, R. J. Warburton, B. D. Gerardot, and P. M. Petroff, *Voltage-Controlled Optics of a Quantum Dot*, Phys. Rev. Lett. 93, 217401 (2004).

[4] J. M. Smith, P. A. Dalgarno, R. J. Warburton, A. O. Govorov, K. Karrai, B. D. Gerardot, and P. M. Petroff, *Voltage Control of the Spin Dynamics of an Exciton in a Semiconductor Quantum Dot*, Phys. Rev. Lett. 94, 197402 (2005).

[5] S. Strauf, N. G. Stoltz, M. T. Rakher, L. A. Coldren, P. M. Petroff, and D. Bouwmeester, *High-frequency single-photon source with polarization control*, Nature Photonics 1, 704 (2007).

APPENDIX

A. ESTIMATE OF EXCITATION DENSITY

The excitation density is estimated by taking the following parameters into account: the intensity, reflection at the surface, the energy of the excitation pulse, the repetition rate of the excitation source, the thickness of the absorbing material and the absorption coefficient of the material.

The number of photons incident on the sample surface per pulse per quantum dot is calculated as

$$n_{\mathrm{ph}} = \frac{I\lambda_{\mathrm{ex}}}{hc_0\sigma_{\mathrm{QD}}f_{\mathrm{rep}}}, \tag{A.1}$$

where I is the intensity, λ_{ex} is the wavelength of the excitation source, f_{rep} is the repetition frequency of the excitation source, h is Planck's constant, c_0 is the speed of light and σ_{QD} is the (surface) density of the quantum dots.

However, part of the incident light is reflected in the dielectric interface. The transmitted part can be calculated using Fresnel's equations as

$$T = 1 - \left|\frac{n_2\cos\theta_1 - n_1\cos\theta_2}{n_2\cos\theta_1 - n_1\cos\theta_2}\right|^2 \quad , \quad \theta_2 = \arcsin\left(\frac{n_1}{n_2}\sin(\theta_1)\right), \tag{A.2}$$

where n_2 is the refractive index of GaAs, n_1 is the refractive index of air, θ_1 is the pump angle (pump normal to sample: $\theta_1 = 0$) and θ_2 is the angle of the refracted light given be Snell's Law, as stated above. We have chosen to use a TM-polarized pump beam as this allows us to pump at the Brewster angle and thus minimize reflection in the surface. Hence, only the Fresnel equation for TM polarized light is stated above.

As the GaAs barriers in all our samples are bounded by materials with a higher electronic band gap, only photons absorbed in the GaAs will have a possibility of being captured in the quantum dots. For a GaAs barrier of thickness d the absorption in given by

$$I_{\mathrm{abs}} = I_0\big(1 - \exp(-\alpha d)\big), \tag{A.3}$$

where I_0 is the incident intensity and α is the wavelength dependent absorption coefficient, which for GaAs is $\alpha = 1.216 \cdot 10^4\,\mathrm{cm}^{-1}$ at 1.6 eV (826 nm) [1].

Is is important to stress that we estimate the number of excitons absorbed in the GaAs per quantum dot. This is not identical to the number of excitons captured in the quantum dots, but an upper estimate. This is evident from the spectra acquired which show strong emission at the energy corresponding to the carbon defect even for low excitation densities. Judging from the spectra approximately half of the excitons are captured in carbon defects even at low powers. As the excitation density is increased a larger fraction of the created excitons will decay directly from the GaAs barrier or from the carbon defects and thus not be captured by the dots.

References to Appendix A

[1] S. L. Chuang, *Physics of Optoelectronic Devices*, Wiley-Interscience, New York (1995).

B. NUMERICAL SOLUTIONS OF THE FIVE-LEVEL SYSTEM

To calculate the initial population probabilities of the bright and dark states in the quantum dots (QDs), we set up a five-level model which include the following levels: the ground state $|g\rangle$, the bright exciton $|b\rangle$, the dark exciton $|d\rangle$, the bi-exciton $|xx\rangle$, and a reservoir level $|R\rangle$. The levels are coupled as depicted in Fig. B.1. The rates used here are the total rates, i.e., the sum of the non-radiative

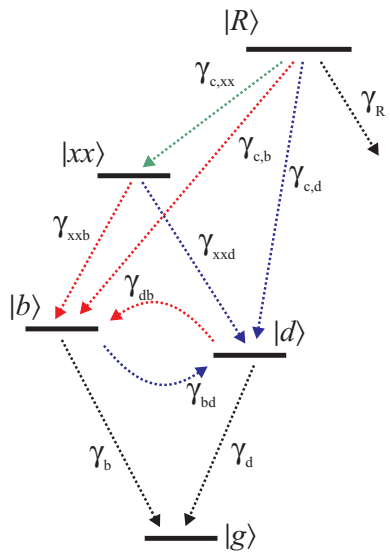

Fig. B.1: The five-level system consisting of the ground state $|g\rangle$, the bright exciton $|b\rangle$, the dark exciton $|d\rangle$, the bi-exciton $|xx\rangle$, and a reservoir level $|R\rangle$. The channels coupling the different levels are denoted by the respective rates.

and radiative decay rates. The system is excited by injecting a population of N excitons per quantum dot at the reservoir level $|R\rangle$, from where it relaxes down and populate the lower lying states. The population probabilities for the ground state, bright-exciton state, dark-exciton state, bi-exciton state and the reservoir are denoted by ρ_{g}, ρ_{b}, ρ_{d}, ρ_{xx}, and ρ_{R} , respectively, and attain values between 0

and 1. Moreover $\rho_{\mathrm{g}} + \rho_{\mathrm{b}} + \rho_{\mathrm{d}} + \rho_{\mathrm{xx}} = 1$.

To set up the rate equations governing the system we start by considering the processes leading to the population of the bright state. These processes are indicated by the red arrows in Fig. B.1. A bright exciton can be created in three ways: (i) an exciton is captured by a QD in the ground state, (ii) a bi-exciton decays leaving a bright exciton behind, or (iii) a dark exciton undergoes a spin flip and becomes a bright exciton.

- The rate of process (i) is proportional to
  - the number of excitons in the reservoir $N\rho_{\mathrm{R}}$
  - the probability of having a QD in the ground state ρ_{g}
  - the capture rate from the reservoir to the QD $\gamma_{\mathrm{c,b}}$

$$\gamma_{\mathrm{c,b}}\rho_{\mathrm{g}}N\rho_{\mathrm{R}} \tag{B.1}$$

- The rate of process (ii) is proportional to
  - the probability of having a QD in the bi-exciton state ρ_{xx}
  - the decay rate of the bi-exciton γ_{xxb}

$$\gamma_{\mathrm{xxb}}\rho_{\mathrm{xx}} \tag{B.2}$$

- The rate of process (iii) is proportional to
  - the probability of having a QD in the bright exciton state ρ_{b}
  - the spin-flip rate of dark excitons γ_{db}

$$\gamma_{\mathrm{db}}\rho_{\mathrm{d}} \tag{B.3}$$

The dark state can be populated by similar processes, resulting in similar terms, the subscripts b and d should just be exchanged.

A bi-exciton can only be created if a QD is in either the bright or the dark state and another exciton is captured. This process is indicated by the green arrow in Fig. B.1.

- The probability of the creation of a bi-exciton is proportional to
  - the sum of the probabilities of having a QD in either the bright or the dark exciton state $\rho_{\mathrm{b}} + \rho_{\mathrm{d}}$
  - the number of excitons in the reservoir $N\rho_{\mathrm{R}}$
  - the capture rate from the reservoir to the QD $\gamma_{\mathrm{c,xx}}$

$$\gamma_{\mathrm{c,xx}}N\rho_{\mathrm{R}}(\rho_{\mathrm{b}} + \rho_{\mathrm{d}}) \tag{B.4}$$

The only processes which have not been addressed so far are: the decay of either the bright (γ_{b}) or the dark (γ_{d}) populations resulting in a transition to the ground state, and the escape of population out of the reservoir (γ_{R}).

Combining the process mentioned above, we can set up the master equations describing the temporal evolution of the population probabilities as

$$\frac{d\rho_{\mathrm{g}}}{dt} = \gamma_{\mathrm{d}}\rho_{\mathrm{d}} + \gamma_{\mathrm{b}}\rho_{\mathrm{b}} - (\gamma_{\mathrm{c,d}} + \gamma_{\mathrm{c,b}})\rho_{\mathrm{g}} N \rho_{\mathrm{R}} \tag{B.5}$$

$$\frac{d\rho_{\mathrm{b}}}{dt} = \gamma_{\mathrm{xxb}}\rho_{\mathrm{xx}} + \gamma_{\mathrm{db}}\rho_{\mathrm{d}} - \gamma_{\mathrm{bd}}\rho_{\mathrm{b}} - \gamma_{\mathrm{b}}\rho_{\mathrm{b}} + \gamma_{\mathrm{c,b}}\rho_{\mathrm{g}} N \rho_{\mathrm{R}} - \gamma_{\mathrm{c,xx}}\rho_{\mathrm{b}} N \rho_{\mathrm{R}} \tag{B.6}$$

$$\frac{d\rho_{\mathrm{d}}}{dt} = \gamma_{\mathrm{xxd}}\rho_{\mathrm{xx}} + \gamma_{\mathrm{bd}}\rho_{\mathrm{b}} - \gamma_{\mathrm{db}}\rho_{\mathrm{d}} - \gamma_{\mathrm{d}}\rho_{\mathrm{d}} + \gamma_{\mathrm{c,d}}\rho_{\mathrm{g}} N \rho_{\mathrm{R}} - \gamma_{\mathrm{c,xx}}\rho_{\mathrm{d}} N \rho_{\mathrm{R}} \tag{B.7}$$

$$\frac{d\rho_{\mathrm{xx}}}{dt} = \gamma_{\mathrm{c,xx}} N \rho_{\mathrm{R}}(\rho_{\mathrm{b}} + \rho_{\mathrm{d}}) - (\gamma_{\mathrm{xxb}} + \gamma_{\mathrm{xxd}})\rho_{\mathrm{xx}} \tag{B.8}$$

$$\frac{d\rho_{\mathrm{R}}}{dt} = -\gamma_{\mathrm{R}}\rho_{\mathrm{R}} - (\gamma_{\mathrm{c,d}} + \gamma_{\mathrm{c,b}})\rho_{\mathrm{g}} N \rho_{\mathrm{R}} - \gamma_{\mathrm{c,xx}} N \rho_{\mathrm{R}}(\rho_{\mathrm{b}} + \rho_{\mathrm{d}}). \tag{B.9}$$

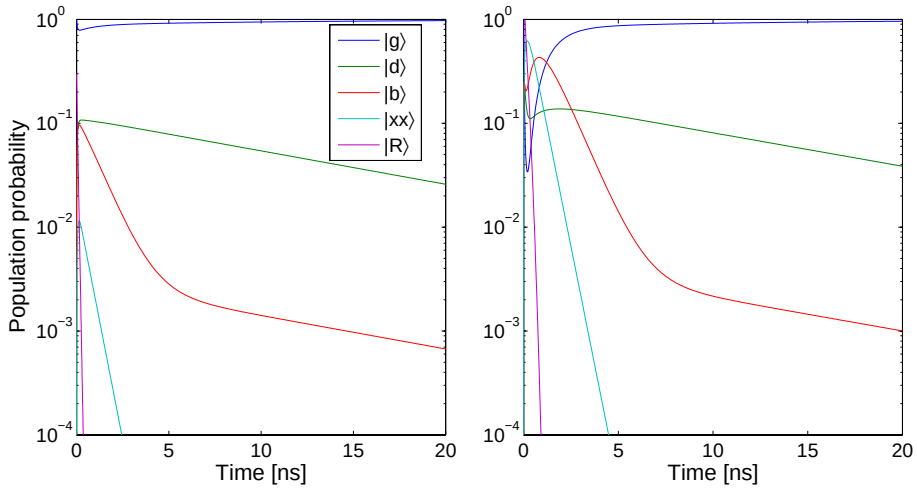

Fig. B.2: The decay of the population probabilities of the ground state (blue), dark state (green), bright state (red), bi-exciton state (cyan) and the reservoir (blue). The following rates are used in the calculation (in units of ns^{-1}) : $\gamma_{\mathrm{b}} = 1$, $\gamma_{\mathrm{d}} = 0.05$, $\gamma_{\mathrm{xxd}} = 0.1$, $\gamma_{\mathrm{xxb}} = 2$, $\gamma_{\mathrm{c,b}} = \gamma_{\mathrm{c,d}} = \gamma_{\mathrm{c,xx}} = 100$, $\gamma_{\mathrm{R}} = 4$, $\gamma_{\mathrm{db}} = \gamma_{\mathrm{bd}} = 0.025$.

The rate equations are solved using MatLab's ordinary-differential equation solver (ODE45). In Fig. B.2 are shown the temporal evolution of the population probabilities for the five levels. The calculations are obtained for an initial pop-

ulation of the reservoir level of 0.3 and 3.0, shown in the left and right figure, respectively.

The decay of the bright exciton (red) exhibits the characteristic bi-exponential decay while the dark excitons (green) and the bi-excitons (cyan) decay single-exponentially. For low excitation (left figure) the initial populations of the bright and dark states are similar, while the initial population of bi-excitons is approximately an order of magnitude lower. Increasing the excitation density by a factor of 10 (right plot) the initial population of the bright exciton is higher than both the bright and the dark initial populations. This directly causes a redistribution of the initial populations among the bright and dark states, favouring the bright states as the bi-exciton most likely undergoes a radiative decay. The rates used in the calculation are given in the figure caption. To obtain the ratio of the initial dark and bright populations, however, only the decay rates of the bi-exciton are of importance.

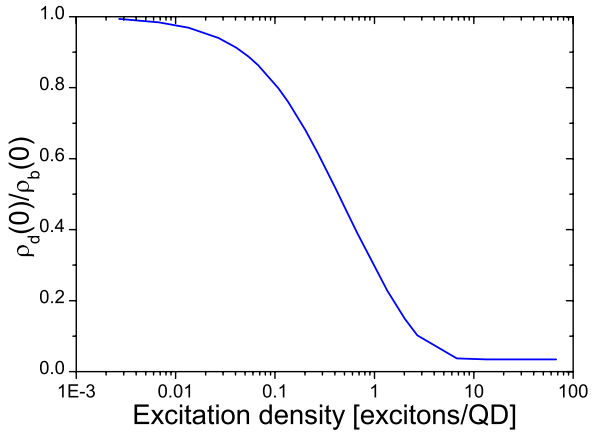

Fig. B.3: The ratio of the initial populations of the dark and bright states. In the low excitation limit the bi-exciton creation is very unlikely resulting in a ratio of unity. In the limit of strong excitation only bi-excitons are created and the ratio settles at value given by the quantum efficiency of the bi-exciton.

We have obtained the initial populations for various excitation levels and calculated the ratio of the dark and bright initial populations, as shown in Fig. B.3. In the limit of low excitation the probability of creating bi-excitons is negligible,

hence the ratio of the initial populations of the dark and bright states are unity. As the excitation density is increased, the probability of creating bi-excitons increases and results in a larger fraction of bright excitons. In the limit of strong excitation only bi-excitons are created, and the ratio therefore settles at a value given by the quantum efficiency of the bi-exciton.